ABSTRACT

Title of Document: INFLUENCE OF POLYMER STRUCTURE ON PLASMA-POLYMER INTERACTIONS IN RESIST MATERIALS

Robert Lawson Bruce, Doctor of Philosophy, 2010

Directed By: Professor Gottlieb S. Oehrlein, Department of Materials Science and Engineering and Institute for Research in Electronics and Applied Physics

The controlled patterning of polymer resists by plasma plays an essential role in the fabrication of integrated circuits and nanostructures. As the dimensions of patterned structures continue to decrease, we require an atomistic understanding underlying the morphological changes that occur during plasma-polymer interactions. In this work, we investigated how plasma surface modifications and the initial polymer structure influenced plasma etch behavior and morphological changes in polymer resists. Using a prototypical argon discharge, we observed polymer modification by ions and vacuum ultraviolet (VUV) radiation from the plasma. A thin, highly dense modified layer was formed at the polymer surface due to ion

bombardment. The thickness and physical properties of this ion-damaged layer was independent of polymer structure for the systems examined here. A relationship was observed that strongly suggests that buckling caused by ion-damaged layer formation on a polymer is the origin of roughness that develops during plasma etching. Our results indicate that with knowledge of the mechanical properties of the ion-damaged layer and the polymer being processed, plasma-induced surface roughness can be predicted and the surface morphology calculated. Examining a wide variety of polymer structures, the polymer poly(4-vinylpyridine) (P4VP) was observed to produce extremely smooth surfaces during high-ion energy plasma etching. Our data suggest that VUV crosslinking of P4VP below the ion-damaged layer may prevent wrinkling. We also studied another form of resists, silicon-containing polymers that form a SiO_2 etch barrier layer during O_2 plasma processing. In this study, we examined whether assisting SiO_2 layer formation by adding Si-O bonds to the polymer structure would improve O_2 etch behavior and reduce polymer surface roughness. Our results showed that while adding Si-O bonds decreased etch rates and silicon volatilization during O_2 plasma exposure, the surface roughness became worse. Enhanced roughening was linked to the decrease in glass transition temperature and elastic modulus as Si-O bonds were added to the polymer structure. For polymers used as resists it is required that the mechanical properties of the ion-damaged layer and the polymer be taken into account to understand their roughening behavior.

INFLUENCE OF POLYMER STRUCTURE ON PLASMA-POLYMER INTERACTIONS IN RESIST MATERIALS

By

Robert Lawson Bruce

Dissertation submitted to the Faculty of the Graduate School of the
University of Maryland, College Park, in partial fulfillment
of the requirements for the degree of
Doctor of Philosophy
2010

Advisory Committee:
Prof. Gottlieb S. Oehrlein, Dept. of Materials Science & Engineering, Chair
Prof. Robert M. Briber, Dept. of Materials Science & Engineering
Prof. Peter Kofinas, Dept. of Materials Science & Engineering
Prof. John Melngailis, Dept. of Electrical & Computer Engineering
Prof. Raymond J. Phaneuf, Dept. of Materials Science & Engineering

© Copyright by
Robert Lawson Bruce
2010

Dedication

This dissertation is dedicated in memory of my Grandfather and Grandmother:

Robert Donald Bruce

and

Anne Tafra Bruce

Acknowledgements

First and foremost, I would like to thank my advisor, Professor Oehrlein for being my guide through this whole amazing adventure. Your thoughts and ideas were so valuable to me. You gave me the opportunities, the encouragement, and the independence to do top scientific research and discover new things. Lastly, you taught me to strive for excellence in everything that I do. Thank you.

I would like to thank the National Science Foundation (NSF) (under Award NIRT No. CTS-0506988) for their financial support for these many years.

I would also like to thank my dissertation committee for showing so much interest and enthusiasm in my work and I hope you enjoy reading my dissertation. Thank you, Professor Briber, Professor Kofinas, Professor Melngailis, and Professor Phaneuf.

To my collaborators, without the insights and ideas, the competition, the hard work and help that came from all of you, I would not have gotten so far and progressed so much. Thank you, Dr. Brian Long, William Bell, Prof. Grant Willson (University of Texas, Austin), T. C. Lin, Dr. Taesoon Kwon, Dr. Hung-Chih Kan, Prof. Ray Phaneuf (LPS at the University of Maryland, College Park), Dr. Joe Végh, Dr. Dustin Nest, Prof. David Graves (University of California, Berkeley), and Dr. Azar Alizadeh (GE Global Research) for all your contributions. I am especially grateful to T. C. Lin and Dr. Taesoon Kwon for spending so much of their valuable time on the AFM, scanning hundreds of my samples.

To my colleagues throughout these 4.5 years who are also my dear friends, Dr. Xuefeng Hua, Dr. Li Ling, Dr. Sebastian Engelmann, Ming-Shu Kuo, Florian Weilnboeck, Nick Fox-Lyon, Masahiro Sumiya, Dr. Arup Pal, Dr. Deuk-Yeon Lee and Yilin Liu, I will never forget the times we had together. Thanks for the friendship and support.

I'm also very grateful to all of my students that helped me do outstanding research, including Chase Dutton, Scott Perusse, Michael Sweatt, Kevin Dwyer, Tshikuna Muanankese, and Sivan Shachar.

Thank you to Professor Ralph W. Bruce, my uncle and mentor, who taught me how to do research and love it. Thank you to Professor Luz Martinez-Miranda for the invaluable guidance you provided me during my first year as a PhD student.

Thanks to the many people who helped me and my research, including Jay Pyle, Bryan Quinn, Joe Kselman, Tim Corrigan, Susan Buckhout-White, Laurent Henn-Lecordier and Josh Balsam.

To my Mom and Dad, Robert Joseph and Yu Yumei Bruce, there are no words to express my gratitude for all that you've done to make me the man I am today. To my big sis, Sandy Bruce, thank you for being my good friend for all these years! To Nate Pantumsinchai and Miha Vindis, I made it! We're one step closer…

Finally, to my fiancée, Taesoon Kwon, your love kept me going. Thank you with all my heart and see you in March!

Table of Contents

Dedication ii
Acknowledgements iii
Table of Contents v
List of Tables viii
List of Figures ix

Chapter 1: Introduction 1

1.1 Progress in Semiconductor Device Fabrication 1
1.2 Advances in Resist Technology 4
1.3 Polymer Modification by Plasma 6
1.4 Modification of Si-containing Polymers in Oxygen Plasma 9
1.5 Surface Roughness and Line Edge Roughness 9
1.6 Experimental Approach 11
1.6.1 Collaborative Research 11
1.6.2 Laboratory for Plasma Processing of Materials 12
1.6.3 Plasma Processing 13
1.6.4 Surface Characterization 16
1.7 Outline of Thesis 17

Chapter 2: Study of Ion and Vacuum Ultraviolet-induced Effects on Styrene- and Ester-based Polymers Exposed to Argon Plasma 19

2.1 Introduction 22
2.2 Experimental Setup and Procedures 25
2.2.1 Description of Materials 25
2.2.2 Plasma Processing 27
2.2.3 Surface Characterization 31
2.3 Results and Discussion 33

2.3.1 Empirical Study of the Contribution of Ions, VUV Radiation and Temperature to Polymer Modification by Ar Plasma 33
2.3.2 Dependence of Etch Rate on Temperature and Polymer Degradation 42
2.3.3 Ellipsometric Analysis of Ar Plasma Etched Polymers at Fixed Low Temperature 45
2.3.4 Characterization of Polymer Surface Modification by High Energy Ions 52
2.3.5 Ellipsometric and Roughening Behavior of Ar Plasma Etched Polymers at High RF Bias 56
2.3.6 Discussion: Mechanism of Etching in P4MS, PαMS, and Ester-based Polymers 65
2.4 Summary and Conclusions 68

Chapter 3: Relationship between Nanoscale Roughness and Ion-Damaged Layer in Argon Plasma Exposed Polystyrene Films 71

3.1 Introduction 73
3.2 Experimental Details 75
3.3 Results and Discussion 77
3.4 Conclusions 85

Chapter 4: On the Absence of Post-Plasma Etch Surface and Line Edge Roughness in Vinylpyridine Resists 87

4.1 Introduction 89
4.2 Experimental Setup 90
4.3 Results and Discussion 93
4.3.1 Comparison of Surface and Line Edge Roughness in PS, PαMS, and P4VP 93
4.3.2 Modification of Ion-Damaged Layer by N_2 Addition 99

4.3.3 Modification of Polymer Underlayer by
Plasma VUV Radiation 114
4.3.4 Discussion 117
4.4 Conclusions 119

Chapter 5: Molecular Structure Effects on Dry Etching Behavior
of Si-containing Resists in Oxygen Plasma 120

5.1 Introduction 122
5.2 Experimental Setup 123
5.2.1 Description of Materials 123
5.2.2 Plasma Processing 125
5.2.3 Surface Characterization 125
5.3 Results and Discussion 126
5.3.1 Etching Kinetics 126
5.3.2 XPS Analysis and SiO_2 Layer Characterization 129
5.3.3 Roughness Analysis 136
5.3.4 Influence of Substrate Bias 139
5.3.5 Mechanism of O_2 Plasma Etching 144
5.4 Conclusion 147

Chapter 6: General Conclusions and Future Directions 148

References 152

List of Tables

Chapter 1:

Table 1.1: Organization chart of researchers and competencies.

Chapter 2:

Table 2.1: Estimated steady state damage layer thicknesses and densities for PS, P4MS and PαMS under 100 eV Ar^+ ion bombardment calculated by MD simulations. Data is averaged over the last ~2500 impacts.

Chapter 3:

Table 3.1: Shown are modified layer properties for the different maximum ion energy conditions. h and n-ik were determined by molecular dynamics simulation and ellipsometry, respectively. Density, E_f and σ were obtained from amorphous carbon property relationships in Ref. 3.39, 3.40, and 3.41, respectively. σ_c was calculated from Equation 3.2.

Chapter 5:

Table 5.1: Important parameters of polymers P(Si), P(Si-O), and P(Si-O2).

List of Figures

Chapter 1:

Figure 1.1: Example of an integrated circuit structure manufactured by the photolithographic process.[1.2]

Figure 1.2: Steps in a simple pattern transfer process to make high aspect ratio structures in an underlying material.

Figure 1.3: Schematic of a multi-layer resist.

Figure 1.4: Schematic Overview of LPPM.

Figure 1.5: Schematic of the inductively coupled plasma reactor used in our experiments.

Figure 1.6: Photograph of the inductively coupled plasma reactor showing essential design elements.

Chapter 2:

Figure 2.1: Schematics of the polymer structures are shown with their names in abbreviated form below the structures. The styrene-based polymers are (a) poly(styrene), (b) poly(4-methylstyrene) and (c) poly(α-methylstyrene). The ester-based polymers are (d) poly(methyl methacrylate), (e) poly(hydroxyadamantyl acrylate) and (f) poly(hydroxyadamantyl methacrylate).

Figure 2.2: Schematic of experimental setup for fully-exposed and VUV-only conditions. Fully-covered condition replaces the UV window with a Si roof, which blocks both ions and VUV radiation. The 50 mm sample is either affixed to the bottom electrode by thermal grease, resulting in cooled conditions, or left without grease, resulting in thermally floating conditions and a fast rise in temperature from 10°C to 120°C in 2 minutes.

Figure 2.3: Thickness removed along P4MS and PαMS samples that were partially exposed to Ar plasma and partially covered by a MgF_2 UV window or Si roof at low temperature conditions (a) and high temperature conditions (b). Samples at fixed low temperatures were bonded to the chilled bottom electrode (10°C) with thermal grease. Samples without thermal grease heated with time from 10°C at plasma start to 120°C

after 2 minutes of plasma exposure. Ar discharges were generated using 300W source power, 10 mTorr pressure, 40 sccm gas flow, no RF bias, and 2 minutes plasma exposure time.

Figure 2.4: Thickness removed along 248nm-Type (P4MS and PαMS) and 193nm-Type (HAdA, HAMA, and PMMA) polymer samples that were partially exposed to Ar plasma and partially covered by a MgF_2 UV window high temperature conditions is shown in (a). In (b), the thickness removed in the plasma exposed region and the UV window covered region are compared at low temperature and at high temperature. Samples at fixed low temperatures were bonded to the chilled bottom electrode (10°C) with thermal grease. Samples without thermal grease heated with time from 10°C at plasma start to 120°C after 2 minutes of plasma exposure. Ar discharges were generated using 300W source power, 10 mTorr pressure, 40 sccm gas flow, no RF bias, and 2 minutes plasma exposure time.

Figure 2.5: Etch-induced RMS roughness of polymers after plasma exposure for full exposed and VUV-only conditions. Samples without thermal grease heated with time from 10°C at plasma start to 120°C after 2 minutes of plasma exposure. Ar discharges were generated using 300W source power, 10 mTorr pressure, 40 sccm gas flow, no RF bias, and 2 minutes plasma exposure time.

Figure 2.6: Etch rate of P4MS (a) PαMS (b) and PMMA (c) samples as a function of plasma exposure time. While the plasma is on, the thermally floating samples rise in temperature. After 60 seconds, the plasma is turned off and the samples are cooled down for 5 minutes. The samples are exposed to the plasma three more times with 5 minute cooling in between each run. Ar discharges were generated using 300W source power, 10 mTorr pressure, 40 sccm gas flow, no RF bias, and 2 minutes plasma exposure time.

Figure 2.7: Ψ-Δ plots of P4MS and PαMS (a) and HAdA and HAMA (b) exposed to Ar discharges are shown. The Ψ-Δ simulated trajectories of unexposed P4MS (i), PαMS (ii), HAdA (iv) and HAMA (v) with varying thickness and constant refractive index are shown for comparison. Also, the Ψ-Δ simulated trajectory for a constant 30nm UV modified layer on top of a varying thickness of unexposed PαMS (iii) is shown in (a). Ar discharges were generated using 300W source power, 10 mTorr pressure, 40 sccm gas flow, and no RF bias.

Figure 2.8: Etch rate versus plasma exposure time for P4MS, PαMS, HAdA, HAMA, and PMMA under Ar plasma discharge. Ar discharges were generated using 300W source power, 10 mTorr pressure, 40 sccm gas flow, no RF bias, and 1 minute plasma exposure time.

Figure 2.9: (a) Side view MD simulation image of PS after ~7800 impacts of 100 eV Ar^+ ions. The estimated thickness of the densified layer at the surface is 1.61nm. (b) Ψ-Δ plot of PS etched by Ar plasma with -100V bias and then etched again with no bias. Also shown are simulated trajectories of unmodified PS (i) and PS with a constant 1.61nm thickness damage layer and complex refractive index 2.39-0.4i (ii). Ar discharges were generated using 300W source power, 10 mTorr pressure, 40 sccm gas flow, -100V RF bias, and 1 minute plasma exposure time.

Figure 2.10: (a) The upper plot shows a comparison of valence bands for unexposed and plasma exposed with -100V RF bias PS measured by XPS. The lower plot is the difference between the unexposed and plasma exposed with -100V RF bias PS. (b) At a high RF bias of -150V, a graphitic peak can be seen in the Raman spectra.

Figure 2.11: Ψ-Δ plot (a) and optical model (b) for P4MS under -100V self-bias conditions. Simulated trajectories for unmodified P4MS (i) and constant ion-damaged layer on top of P4MS (i) are also shown. Ar discharges were generated using 300W source power, 10 mTorr pressure, 40 sccm gas flow, -100V RF bias, and 5 minute plasma exposure time.

Figure 2.12: Ψ-Δ plot (a) and optical model (b) for PαMS under -100V self-bias conditions. Simulated trajectories for unmodified PαMS (i), constant ion-damaged layer on top of PαMS (ii) and constant ion-damaged layer and UV-damaged layer on top of PαMS (iii) are shown. Ar discharges were generated using 300W source power, 10 mTorr pressure, 40 sccm gas flow, -100V RF bias, and 5 minute plasma exposure time.

Figure 2.13: Etch rate versus plasma exposure time for P4MS, PαMS, HAdA, and HAdA under Ar -100V self-bias conditions. Inset is a close-up of the reduced etch rate steady-state regime. Ar discharges were generated using 300W source power, 10 mTorr pressure, 40 sccm gas flow, -100V RF bias, and 1 minute plasma exposure time.

Figure 2.14: RMS roughness of polymers versus plasma exposure time is shown for P4MS, PαMS, HAdA, and HAMA under Ar -100V self-bias conditions. Ar discharges were generated using 400W source power, 10 mTorr pressure, 50 sccm gas flow, -100V RF bias, and 1 minute plasma exposure time. Gradient structures were made to be able to measure RMS roughness versus plasma exposure time.

Figure 2.15: Schematic of polymer chains exposed to ionizing radiation for conditions above and below the ceiling temperature.

Chapter 3:

Figure 3.1: A schematic of the highly stressed, modified layer formation and roughening that occurs simultaneously at the surface of a polystyrene film under Ar plasma exposure. Important materials and morphological properties are also shown.

Figure 3.2: Dependence of ion-damaged layer thickness, h, on the maximum ion energy determined by XPS analysis and MD simulation.

Figure 3.3: (a) 2 × 2 μm AFM images showing surface roughness in PS after ion bombardment at varying maximum ion energies. Also shown are calculated and experimental values of λ (b) and A (c) versus maximum ion energy of the nanoscale roughness processed at 40°C.

Figure 3.4: (a) 50 × 50 μm AFM images showing surface roughness in PS after the samples processed under the same conditions are heating to 170°C. Also shown are calculated and experimental values of λ (b) and A (c) versus maximum ion energy of plasma processed samples after heating to 170°C.

Chapter 4:

Figure 4.1: (a) AFM images with corresponding polymer structures as inset and (b) comparison of RMS roughness for PS, PαMS and P4VP after 100% Ar and 90% Ar/C_4F_8 plasma exposure. Samples were etched for 60 seconds.

Figure 4.2: RMS roughness of selected polymers (P4VP, PS, P4MS, PαMS, HAdA, HAHA, 248 nm PR and 193 nm PR) after Ar and 90% Ar/C_4F_8 plasma exposures. Samples were etched for 60 seconds.

Figure 4.3: SEM images of hot embossed patterned samples of PS, PαMS and P4VP are shown after (a) 100% Ar and (b) 90% Ar/C_4F_8 plasma exposure.

Figure 4.4: (a) Removed thickness and (b) etch rate for PS, PαMS and P4VP after Ar plasma exposure.

Figure 4.5: Dependence of ion-damaged layer thickness, h_f, on maximum ion energy for PS exposed to 0%, 2.5% and 5% N_2 added to an Ar discharge and P4VP exposed to an Ar discharge.

Figure 4.6: Ψ-Δ plot for PS exposed to 0%, 2.5% and 5%N_2 added to an Ar discharge.

Figure 4.7: Dependence of (a) density, ρ, and (b) elastic modulus, E_f, of the ion-damaged layer on maximum ion energy for PS exposed to 0%, 2.5% and 5% N_2 added to an Ar discharge.

Figure 4.8: Dependence of (a) amplitude, A, and (b) wavelength, λ, on maximum ion energy 0% and 2.5% N_2 added to an Ar discharge.

Figure 4.9: AFM images of PS exposed to 0% and 2.5% N_2 added to an Ar discharge with maximum Ar^+ ion energy at 135 eV.

Figure 4.10: Etch rate versus %N_2 addition in an Ar discharge is shown for PS from 75 eV to 135 eV.

Figure 4.11: (a) AFM section scan and (b) AFM images of PS exposed to 0% N_2 in an Ar discharge at 135 eV maximum ion energy and 5% N_2 in an Ar discharge at 50 eV maximum ion energy, both heated afterwards to 110 °C.

Figure 4.12: Dependence of (a) amplitude, A, and (b) wavelength, λ, on maximum ion energy for PS exposed to 0%, 2.5% and 5% N_2 added to an Ar discharge and then heated to 110 °C.

Figure 4.13: Comparison of the dependence of amplitude, A, in PS and P4VP on maximum ion energy after exposure to an Ar discharge.

Figure 4.14: Comparison of the dependence of wavelength, λ, on maximum ion energy in PS after exposure to Ar and Ar/N_2 discharges and P4VP after exposure to an Ar discharge and then both heated above their respective T_g (PS, 110 °C, and P4VP, 155 °C).

Figure 4.15: Comparison of ion-damaged layer elastic modulus, E_f, of Ar/N_2 exposed PS and Ar exposed P4VP versus maximum ion energy.

Figure 4.16: Dependence of the change in refractive index on VUV exposure time for PS, PαMS, and P4VP.

Figure 4.17: XPS N 1*s* spectra of unexposed P4VP and VUV-exposed P4VP.

Figure 4.18: Schematic of the mechanisms of surface morphology development in PS and P4VP after plasma exposure and after plasma exposure and subsequent heating above glass transition temperature.

Chapter 5:

Figure 5.1: Molecular structures of (a) P(Si), (b) P(Si-O) and (c) P(Si-O2).

Figure 5.2: (a) Thickness removed and (b) etch rate dependence on plasma exposure time for P(Si), P(Si-O) and P(Si-O2). Polymers were etched using O_2 plasma without substrate bias.

Figure 5.3: The changes in the XPS C1*s*, Si 2*p*, and O 1*s* spectra with plasma exposure time are shown for P(Si), P(Si-O), and P(Si-O2). Polymers were etched using O_2 plasma without substrate bias.

Figure 5.4: SiO_2 layer thickness measured by XPS for P(Si), P(Si-O), and P(Si-O2). Polymers were etched under O_2 plasma without substrate bias.

Figure 5.5: Thickness removed versus SiO_2 layer thickness formed is shown for P(Si), P(Si-O), and P(Si-O2) under O_2 plasma with no substrate bias conditions. Dashed lines are linear fits of the experimental data. The solid line is the theoretical linear relationship of thickness removed and SiO_2 layer thickness if no Si is lost during the formation of the SiO_2 layer calculated using equation 5.2.

Figure 5.6: Etch rate versus SiO_2 layer thickness is shown for P(Si), P(Si-O), and P(Si-O2) under O_2 plasma with no substrate bias conditions. Dashed lines are exponential decay fits of the experimental data.

Figure 5.7: Plot (a) of rms roughness dependence on plasma exposure time in P(Si), P(Si-O) and P(Si-O2). Also shown are AFM images (b) of P(Si), P(Si-O) and P(Si-O2) after 120 seconds of plasma exposure. Polymers were etched under O_2 plasma without substrate bias.

Figure 5.8: Etch rate dependence versus thickness removed is shown for P(Si), P(Si-O) and P(Si-O2) under (a) O_2 without substrate bias, (b) O_2 / -100V substrate bias, and (c) (90% N_2 / O_2) / -100V substrate bias processing conditions.

Figure 5.9: Thickness removed (a), SiO_2 layer thickness (b) and rms roughness (c) for P(Si), P(Si-O) and P(Si-O2) in O_2 without substrate bias, O_2 / -100V substrate bias, and (90% N_2 / O_2) / -100V substrate bias processing conditions.

Figure 5.10: Thickness removed (a) and etch rate (b) versus SiO_2 layer thickness formed is shown for P(Si), P(Si-O), and P(Si-O2) under O_2 without

substrate bias, O_2 /-100V substrate bias, and (90% N_2 /O_2) /-100V substrate bias conditions.

Figure 5.11: Schematic of etch behavior for (a) P(Si) and (b) P(Si-O) and P(Si-O2) under O_2 plasma without substrate bias.

Chapter 1: Introduction

1.1 Progress in Semiconductor Device Fabrication

Moore's law states that the number of transistors on an integrated circuit has doubled every two years since the start of the semiconductor industry.[1.1] The roughly exponential increase of device density heralded the information age and is the driving force that continues to increase the performance, speed, capacity and affordability of computing devices to this day. Advances in lithographic technologies for semiconductor device fabrication and nanotechnology have enabled the continuing miniaturization of the critical dimensions (CD) of transistors and other semiconductor devices.

Lithography is a top-down, layer-by-layer approach to making intricate patterns of complex devices and structures on substrates at high throughput and fidelity.[1.2] In particular, the photolithography process used in the semiconductor industry is a simple yet powerful concept that enables the creation of integrated circuits composed of billions of devices and minimum feature sizes down to tens of nanometers. An example of the complexity of a typical integrated circuit is shown in Fig. 1.1.[1.3]

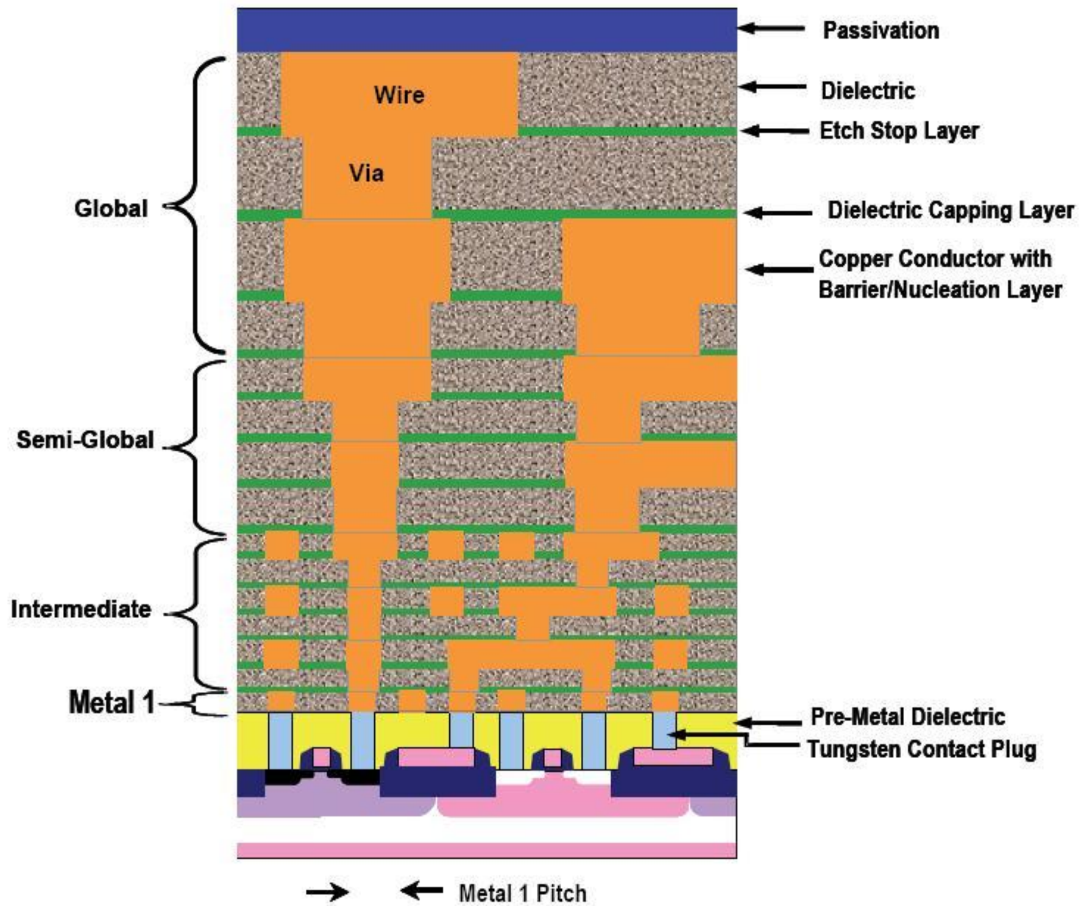

Figure 1.1: Example of an integrated circuit structure manufactured by the photolithographic process.[1.2]

A simple pattern transfer process by photolithography is shown schematically in Fig. 1.2. In this process, a desired pattern is created on a photosensitive polymer resist (photoresist) by UV exposure through a patterned mask. The exposed areas become soluble and are removed, revealing the underlying material below, while the unexposed areas in the resist remain. The pattern in the resist is transferred into the underlying material by etching of the exposed regions by plasma while the regions covered by resist are protected.

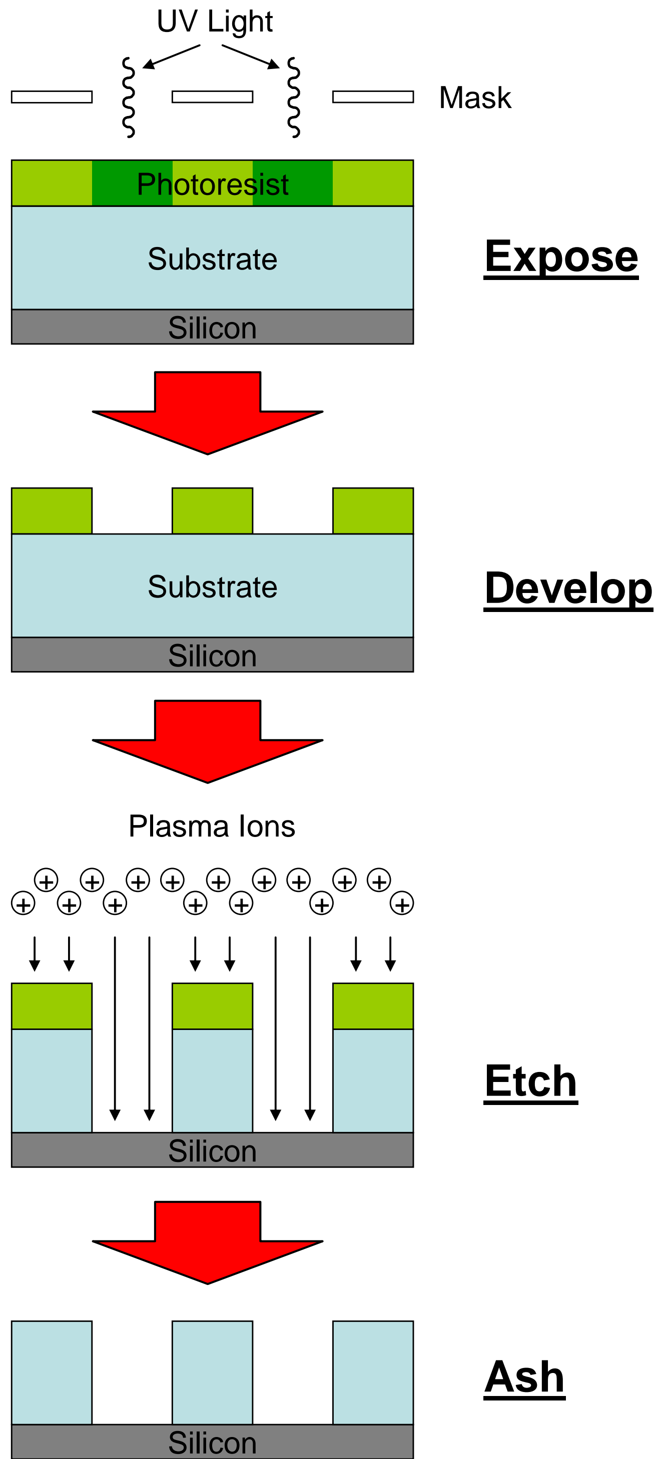

Figure 1.2: Steps in a simple pattern transfer process to make high aspect ratio structures in an underlying material.

1.2 Advances in Resist Technology

High performance resists must be easily patterned, provide protection during pattern transfer into the underlying material, and be removed without much difficulty. In most cases, polymers are used as resist materials. Resists can be patterned in a number of ways depending on the lithographic approach. Photoresists are exposed to UV radiation through a patterned mask and the exposed areas are dissolved away.[1.4] In nanoimprint lithography, a mold is pressed into the resist to make a pattern.[1.5] Block copolymer lithography uses a polymer that self-organizes into a well-defined pattern.[1.6]

After the pattern is made in the resist, it must be transferred into the underlying material. The common method of pattern transfer in most lithographic technologies is by plasma etching.[1.7] The requirements for plasma etching are that there is high selectivity of etching the underlying material over the resist material and that etching is highly anisotropic, i.e. etching is mostly in the vertical direction. The type of plasma chemistry used is highly dependent on the composition of the underlying material. SiO_2 is a common material that has been used as the gate dielectric in transistors and in passivation layers. For SiO_2, a fluorocarbon-based plasma discharge is used as it is highly selective in removing SiO_2 over hydrocarbon-based polymer resists.[1.7]

A dramatic recent change in photoresist polymer type took place as the UV exposure wavelength decreased from 248 nm to 193 nm to further reduce the CD size in integrated circuits.[1.8] The 248 nm photoresist (PR) was too absorbing for 193 nm

due to the presence of aromatic rings in the polymer structure, so an entirely different polymer structure was devised for use with 193 nm exposure wavelengths. These 193 nm PR replaced aromatic rings with large aliphatic cages to reduce UV absorption but maintain the plasma etch resistance. However, 193 nm PR proved to have very low etch resistance and showed much greater plasma-induced roughening compared to 248 nm PR.

Multi-layer resists have been introduced recently to compensate for the poor etch performance of 193 nm PR.[1.9] The most common multi-layer resists are trilayer resist structures with a 193 nm PR on top, a thin Si-containing resist in the middle, and a thick, oxide etch resistant hydrocarbon resist below called the carbon hard mask. A schematic is shown in Fig. 1.3. The 193 nm PR is thin to improve pattern definition during the exposure and development step. An fluorocarbon-based plasma etch step is used to break through the thin Si-containing resist. The multi-layer stack is then exposed to an oxygen plasma, which has high etch selectivity of carbon hard mask over Si-containing resist. Once the pattern is transferred to the thick carbon hard mask, a fluorocarbon-based plasma can be used to etch the underlying oxide layer with a highly etch resistant resist above so that small feature sizes at very high aspect ratios become possible.

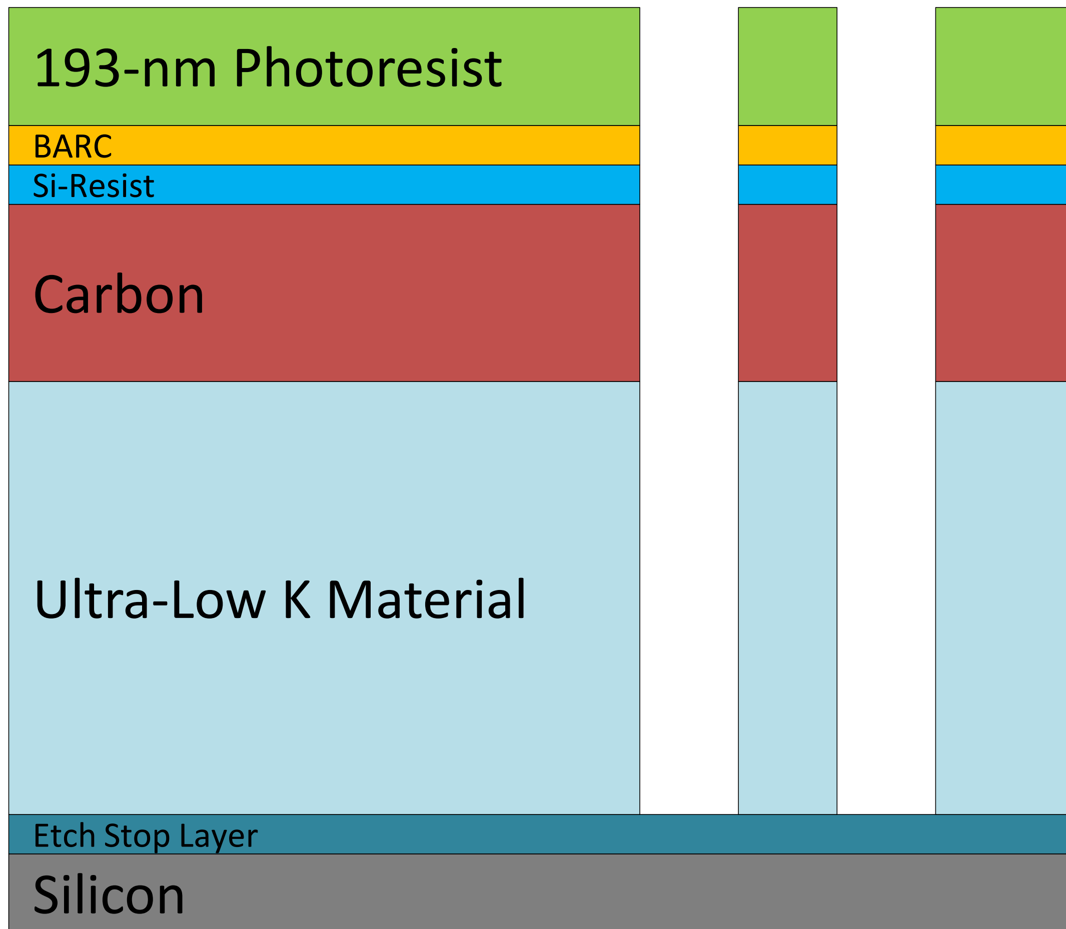

Figure 1.3: Schematic of a multi-layer resist.

1.3 Polymer Modification by Plasma

A plasma is a complex environment and there are many species that can affect a polymer including ions, excited neutrals, electrons and UV/VUV photons.[1.10,1.11] To understand plasma-polymer interactions, the gas discharge chemistry and the plasma conditions must be well-characterized and the effect of all the plasma species on a particular polymer structure must be considered.

Ion bombardment can cause drastic changes to a polymer exposed to a plasma.[12] Ions accelerated toward the polymer induce physical sputtering of material from the surface and collision cascades within the material. Increasing the ion energies enhance the ion effect. There is an ion energy dependent depth in which the ions penetrate within a material. In polymers, for ion energies of several hundred eV, the penetration depth is normally under 10 nm. Depending on the type of chemical bonds the plasma-exposed material contains there can be a preferential bond breaking and selective removal of one species over another. This can cause depletion and changing of the chemical composition within the penetration depth of the ions. Polymers interacting with plasma are especially affected by depletion reactions. In general, Ar^+ ions bombarding a polymer preferentially remove hydrogen and oxygen atoms over carbon atoms, creating a carbon rich surface within the penetration depth of the ions. The modified, carbon rich surface restructures, and densifies.[1.13,1.14]

Modification by plasma VUV radiation must also be considered. Polymers are sensitive to VUV radiation, and the consequences depend on polymer structure and photon energy. The VUV absorption depth in polymers is dependent on the wavelength of the light and polymer type. The absorption depth is usually much larger than the penetration depth of ions, ranging from tens to hundreds of nanometers.[1.15]

Electrons and neutrals may also contribute to surface modification during plasma exposure. The energy of electrons bombarding the polymer film is on the order of a few eV,[1.16] and this will only occur for very short periods during the rf cycle. The energy that can be deposited is likely below that required for bond

breakage. Ions are accelerated to much higher energy and the deposited energy is much greater, making their impact dominant.

The effect of neutrals is dependent on their reactivity with the polymer. Oxygen radicals in an oxygen discharge react with hydrocarbon-based polymers to make many volatile products that are subsequently removed from the surface.[1.17] Thermal neutrals in pure Ar discharges are inert and their temperatures are slightly above room temperature,[1.18] so there will be little chemical etching effect of the polymers. Fast neutrals can be formed in Ar discharges, and their effects will be similar to that of ions. The excited neutrals in an Ar discharge, metastable Ar* atoms, have an internal energy around 12 eV,[1.19] and may contribute to material removal by potential sputtering.

Polymers have been observed to undergo various types of radiation-driven degradation mechanisms under a plasma environment. Degradation mechanisms include chain cross-linking, main-chain scission, and side chain removal. The degradation mechanism is highly dependent on the polymer structure. In one study it was found that polymers that had a hydrogen bonded opposite the side group on the carbon backbone ("α-H") were prone to cross-linking reactions while a methyl group bonded instead ("α-methyl") were prone to main-chain scission reactions.[1.20] A classic example is the difference in response between polystyrene (PS) and poly(α-methylstyrene).[1.21] However, there have been conflicting data comparing PS and PαMS and comparing other polymers with the two types of structure, with sometimes a large difference occurring and sometimes similar behavior is observed.[1.22,1.23,1.24]

1.4 Modification of Si-containing Polymers in Oxygen Plasma

Oxygen plasma has been traditionally used to remove polymer resists after plasma pattern transfer, i.e. the ashing step.[1.17] Oxygen radicals react with hydrocarbon species in the resist and rapidly convert the polymer into volatile species such as H_2O, CO_2, and CO. Etching proceeds quickly in the resist, while underlying materials such as SiO_2 and Si are largely unaffected.

Adding Si to the resist polymer structure causes significant changes in oxygen plasma etch behavior. The oxygen reacts and forms SiO_2 at the resist surface,[1.17,1.25,1.26] which acts as a barrier to further etching. Therefore, Si-containing polymers can be used as resists if in conjunction with a hydrocarbon-based polymer as the underlying material. Si-containing resists are used in many lithographic technologies such as photolithography,[1.9,1.27,1.28] top surface imaging,[1.29,1.30,1.31] block copolymer lithography[1.32] and nanoimprint lithography.[1.33,1.34,1.35]

1.5 Surface Roughness and Line Edge Roughness

Polymers are prone to undesirable surface roughening during plasma processing as a result of exposure to energetic ions, reactive species, and VUV radiation that interact and modify the surface.[1.36,1.37,1.38] As the feature sizes of devices in integrated circuits continue to decrease, polymer resist roughening becomes a greater problem for successful pattern transfer.[1.39,1.40] The correlation between etch behavior and roughening behavior is still largely unknown.

Reducing formation of line edge roughness (LER), the roughness measured along the horizontal edge of etched trenches, is becoming increasingly important as feature sizes shrink. There are many contributions to LER in a patterned resist.[1.41,1.42] For photoresists, a large part originates from the exposure and development step that produces stippled sidewalls.[1.43,1.44,1.45]

Another major contributor to LER is the plasma pattern transfer step.[1.46,1.47] Here, surface roughness formed at the resist surface is transferred along the sidewalls into the underlying material. Therefore, high resist surface roughness leads to enhanced LER. Polymer structure can have a major impact on LER, as was found during the transition from 248 nm to 193 nm PR.[1.48] Changing to 193 nm PR led to a major increase in surface roughness and LER. Choice of polymer structure for photoresists has been restricted due to requirements of transparency to the UV exposure wavelength and ability to undergo acid-catalyzed reactions to increase solubility after photoexposure.[1.8] The advent of alternative lithographic techniques[1.49] (e.g. nanoimprint lithography, extreme ultraviolet lithography and block copolymer lithography) provides the opportunity to optimize polymer structure and composition so that surface roughness and LER are minimized during the plasma pattern transfer steps.

1.6 Experimental Approach

1.6.1 Collaborative Research

This research is a product of a world-class interdisciplinary collaboration bringing together leading experts from academia and industry. An organization chart of researchers and their respective competencies are shown in Table 1.1. The design, development, and synthesis of advanced and novel resist polymer material for this research are accomplished by Prof. Grant Willson's research group at UT – Austin. Dr. Alizadeh's group at GE provides essential development and fabrication of patterned resists using advanced lithographic techniques including nanoimprint lithography by hot embossing and block copolymer lithography. The fundamental aspects of plasma/ion beam/VUV interactions with polymer surfaces are studied by Prof. David Graves' group at UC – Berkeley and compared with realistic plasma conditions in our lab. This is achieved in two ways: molecular dynamics (MD) simulations of ion beam interaction with polymer surfaces and well-characterized ion beam and VUV processing of polymers. The advanced polymer systems provided by Prof. Willson's group, nanostructures fabricated by Dr. Alizadeh and the fundamental insights gained from Prof. Graves' group are applied to our plasma-polymer research and characterization at UMD. Prof. Phaneuf's group at UMD uses their expertise in materials and nanostructure characterization to fully investigate plasma-induced modifications in polymer systems.

<table>
<tr><th>Principal Invesigator</th><th colspan="2">Location</th><th>Graduate Students</th><th>Research Capabilities</th></tr>
<tr><td>Prof. Grant Willson</td><td colspan="2">UT – Austin</td><td>Brian Long</td><td>Advanced Resist Expertise, Model Polymers & Synthesis Capabilities</td></tr>
<tr><td>Dr. Azar Alizadeh</td><td colspan="2">GE Global Research</td><td></td><td>Polymer Expertise and Use of Nanostructures</td></tr>
<tr><td>Prof. David Graves</td><td colspan="2">UC – Berkeley</td><td>Joe Vegh
Dustin Nest</td><td>Ion and VUV Studies & MD Simulations</td></tr>
<tr><td>Prof. Gottlieb Oehrlein</td><td rowspan="2">UMD</td><td>MSE, IREAP</td><td>Robert L. Bruce</td><td>Materials and Nanostructure Plasma Processing & Diagnostics</td></tr>
<tr><td>Prof. Raymond Phaneuf</td><td>MSE, LPS</td><td>T. C. Lin</td><td>Materials & Nanostructure Characterization</td></tr>
</table>

Table 1.1: Organization chart of researchers and competencies.

1.6.2 Laboratory for Plasma Processing of Materials

We used inductively coupled plasma reactors for our plasma processing experiments, which are located in the Laboratory for Plasma Processing of Materials at the University of Maryland in College Park. The major scientific theme of this laboratory is the characterization and understanding of plasma-material interface processes that control the properties of materials/structures that are fabricated by plasma processing. This research requires a variety of equipment, including plasma reactors, plasma characterization tools, and surface analysis equipment. The inductively coupled plasma reactors we used are connected to a cluster system, shown in Fig. 1.4, which enables transfer of samples between chambers under ultra high vacuum conditions. Therefore, a sample can be transferred from the inductively coupled plasma reactor after plasma processing to the Vacuum Generator ESCA Mk

II surface analysis chamber for x-ray photoelectron spectroscopy analysis without exposure to air.

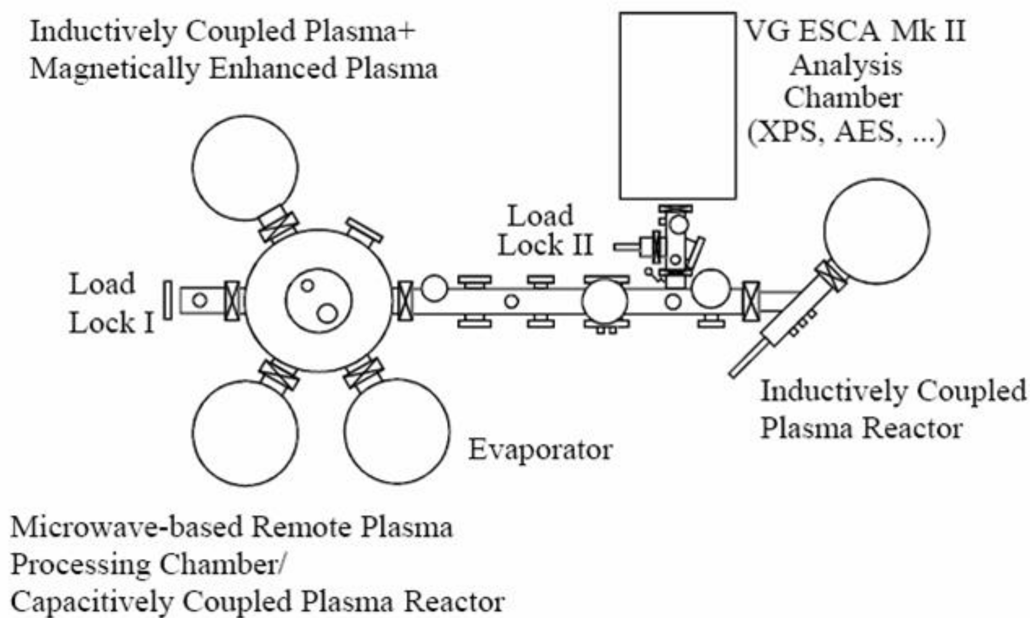

Figure 1.4: Schematic Overview of LPPM.

1.6.3 Plasma Processing

The primary inductively coupled plasma (ICP) reactor used for our studies is one of the best-characterized[1.50,1.51,1.52] and modeled[1.53] reactors available for research. The ICP reactor is shown schematically in Fig. 1. 5 and a photograph of the actual reactor is shown in Fig. 1.6. The plasma is generated inductively using a planar coil placed on top of a quartz window and powered through an L-type matching network at 13.56 MHz with a power supply (0-2000W). Ion bombardment on a 125 mm diameter substrate can be independently controlled using another bias power supply

with a frequency of 3.7 MHz (0-250W). The distance between the quartz window and substrate is 14.5 cm. The bottom electrode where the substrate is fixed is cooled at 10 °C by a chiller. The base pressure achievable was below 1×10^{-6} Torr. Standard processing conditions were 10 mTorr operating pressure and 40 sccm flow rate.

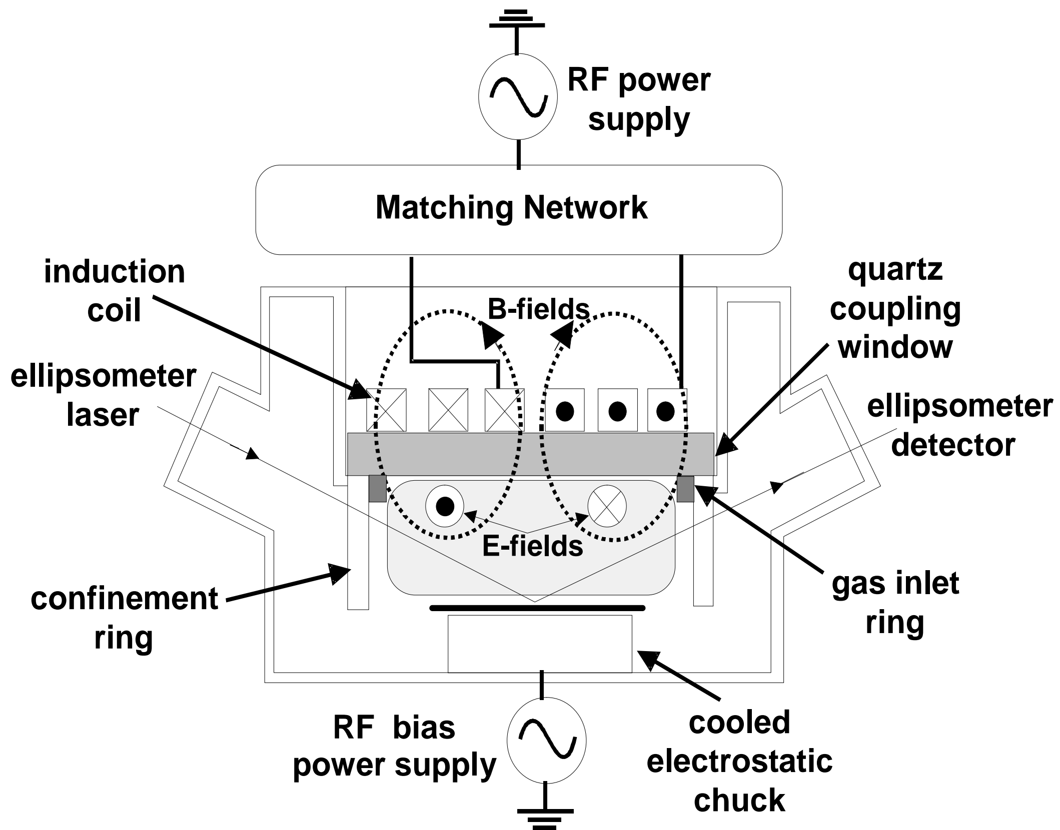

Figure 1.5: Schematic of the inductively coupled plasma reactor used in our experiments.

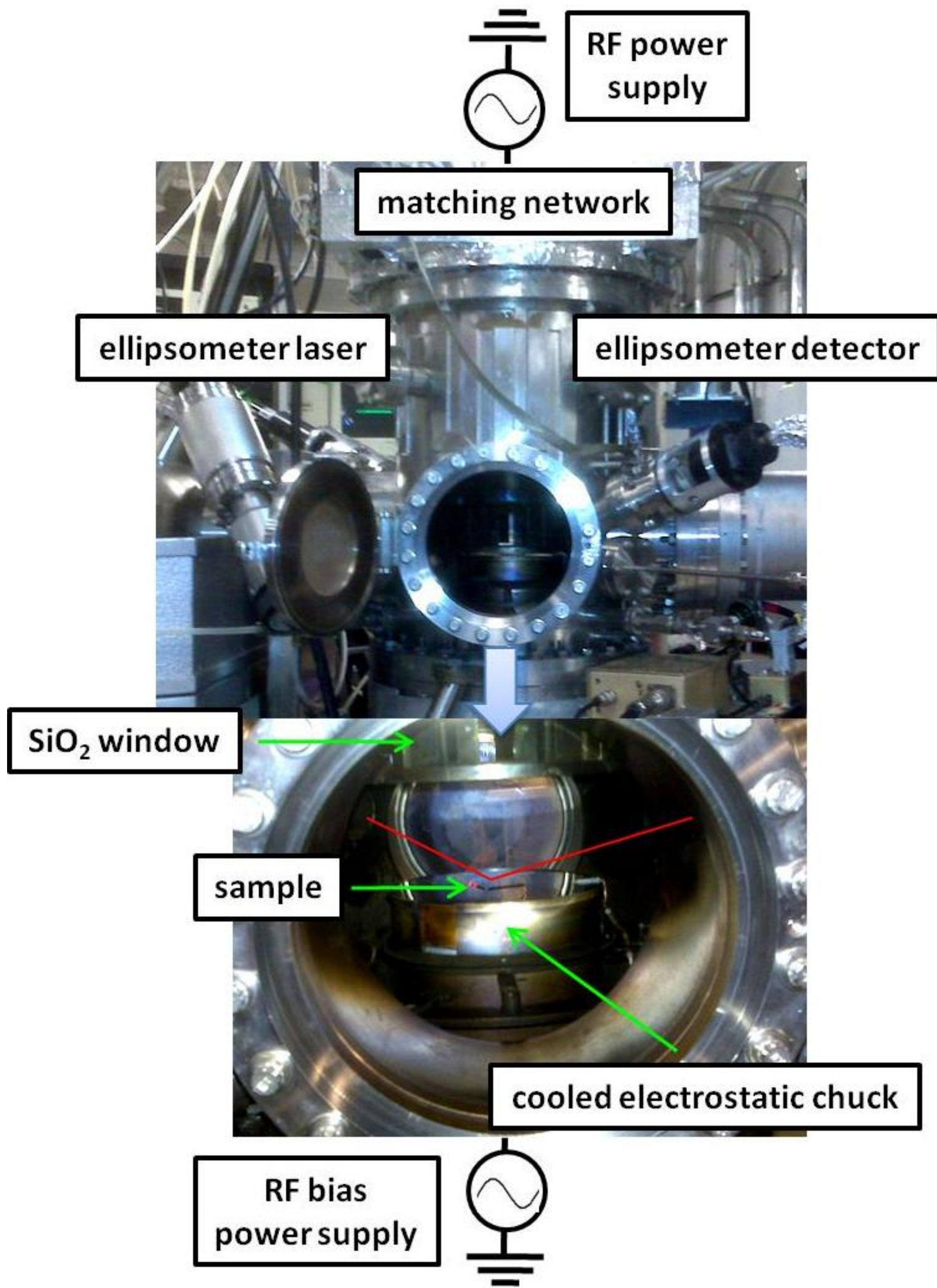

Figure 1.6: Photograph of the inductively coupled plasma reactor showing essential design elements.

1.6.4 Surface Characterization

Thickness and optical properties (refractive index and extinction coefficient) of films were measured *in situ* and in real-time by a single wavelength (HeNe laser) ellipsometer. The ellipsometer is an automated rotating compensator ellipsometer working in the polarizer-compensator-sample-analyzer (PCSA) configuration and with an angle of 71.3°. The ellipsometer measures two angles that describe the relative change in amplitude (Ψ) and change in phase (Δ) of an electric field vector upon reflection.[1.54] The values of Ψ and Δ are measured and related to fundamental physical properties of the film by using an optical model and solving the Fresnel reflection coefficients for the physical property values.[1.55]

For chemical information from the surface, X-ray photoelectron spectroscopy (XPS) analysis was performed in a Vacuum Generators ESCA Mk II surface analysis chamber using a nonmonochromatized Mg Kα source (1253.6 eV) or Al Kα source (1486.5 eV). 25×25 mm^2 samples were transferred in vacuum through the cluster system or in air immediately after plasma processing. Spectra were obtained in constant analyzer energy mode at 20 eV pass energy. The analyzer resolution was approximately 0.2 eV and the resolution of the spectra was limited by the linewidth of the x-ray source, approximately 1 eV.

To characterize the surface morphology, atomic force microscopy (AFM) measurements were performed on unexposed and processed samples. Processed samples were transferred to the AFM in air. The scan size for measurements was normally fixed at 2×2 μm^2, though it could be changed depending on the lateral length scale of the surface features. The surface roughness values reported were

calculated from the RMS of the surface profile after the measurement. The lateral length scale ("wavelength") of the roughness was determined by measuring the peak value in the Fast-Fourier Transform (FFT) spectrum of the AFM images.

1.7 Outline of Thesis

The main goal of this PhD thesis is to establish an atomistic understanding of the interactions of polymer structures with prototypical plasmas during pattern transfer to enable the rational identification of both the molecular design parameters and internal plasma processing parameters required for controlled patterning at nanoscale dimensions.

Towards this goal, this thesis addresses 1) the influence of polymer structure on ion and VUV-induced surface modification behavior, 2) the relationship between nanoscale surface roughness and plasma surface modification, 3) the experimental observation of smooth surfaces after plasma etch in the vinylpyridine polymer, and 4) molecular structure effects on plasma surface modification in Si-containing resists.

In chapter 2, the influence of polymer structure on ion and VUV-induced surface modification behavior is presented. We show that ion bombardment creates a thin, dense, amorphous carbon-like layer on polymer surfaces and that ion effects are the same for polymers with vastly different chemical structures. In contrast, we show that VUV modification is highly polymer structure dependent.

In chapter 3, we establish a relationship between the ion-induced modified layer formed in polymers during plasma etching and the surface roughness that develops at the same time. We show evidence that the large difference in the

mechanical properties of the modified surface layer and the undamaged polymer underlayer induces a buckling instability that forms nanoscale wrinkles on the surface.

In chapter 4, we present the novel result of ultra-smooth surfaces in a vinylpyridine polymer after plasma etching. We compare the surface and sidewall surface morphology of typical polymers with the vinylpyridine polymer to demonstrate how the absence of post-plasma etch surface roughening can benefit plasma processed nanostructures. We then establish the mechanism underlying the retention of smooth surfaces in P4VP.

In chapter 5, we turn to investigating the influence of polymer structure in Si-containing polymers on O_2 plasma surface modification. We show that adding Si-O bonding to the polymer structure increases the etch resistance and reduces Si loss. However, surface roughening becomes worse due to a significant decrease in glass transition temperature with Si-O bonds added.

Finally, we will summarize the main conclusions of the thesis in chapter 6.

Chapter 2: Study of Ion and Vacuum Ultraviolet-induced Effects on Styrene- and Ester-based Polymers Exposed to Argon Plasma

J. Vac. Sci. Technol. B, 27, 1142 (2009)

R. L. Bruce, S. Engelmann, T. Lin, T. Kwon, R. J. Phaneuf, G. S. Oehrlein, B. K. Long, C. G. Willson, J. J. Végh, D. Nest, D. B. Graves and A. Alizadeh

ABSTRACT

Plasma-polymer interactions are important for the purpose of etching, deposition, and surface modification in a wide range of different fields. An Ar discharge from an inductively coupled plasma reactor was used to determine the factors in a simple plasma that control etch and surface roughness behavior for three styrene-based and three ester-based model polymers. We compared the etch behavior of polymers in Ar plasma discharges with low and high energy ions by changing the substrate bias, compared cooled and elevated substrate temperature conditions, and compared fully plasma exposed conditions and vacuum ultraviolet (VUV)-only conditions by employing a magnesium fluoride window to prevent ion bombardment in the VUV-only case. It was found that ions, VUV radiation, and temperature all had significant impact on the etch behavior of polymers. The dependence of polymer structure on etch and surface roughness was also compared. Polymers with styrene and ester side groups were compared and polymers with α-hydrogen and with α-methyl were compared. It was found that for styrene-based polymers, there was a

large difference in material removal between α-hydrogen (poly(4-methylstyrene)(P4MS)) and α-methyl (poly(α-methylstyrene) (PαMS)) structures. This difference was highly temperature dependent, and the ceiling temperature of the polymers was found to be the most important property to consider. Below the ceiling temperature, the amount of material removed in P4MS and PαMS was the same, but above it there was a dramatic material loss in PαMS not seen in P4MS. For the ester-based polymers it was established that oxygen depletion occurred before any other mechanism and the most important factor to consider was oxygen content in the polymer. By using *in situ* ellipsometry, it was also found that at temperatures below the ceiling temperature modification by VUV radiation of PαMS created a slightly denser layer at the surface with higher index of refraction. This effect was not seen in P4MS. It was observed that in general, low energy ions contributed to material removal by physical sputtering at the polymer surface and the amount of material removal increased with oxygen content in the polymer. VUV radiation caused bulk depolymerization and oxygen depletion reactions that were highly polymer structure specific and temperature dependent. High energy ion bombardment was found to create an amorphous carbon-like damage layer with a thickness that was determined by the ion penetration depth. This damage layer could be characterized by ellipsometry. While for P4MS it was sufficient to model by ellipsometry the etch process using an ion-damaged layer on top of a bulk layer of unmodified polymer, the VUV effect needed to be added to the optical model in order to accurately characterize PαMS. Finally, surface roughening of polymers only occurred under ion bombardment. High energy ion bombardment produced the greatest roughness and

corresponded to densification of the ion-damaged layer at the surface. Polymers that exhibited greater material loss to create the damaged layer showed the highest roughness.

2.1 Introduction

The exposure of polymers to plasmas is an important method for the purpose of etching, deposition, and surface modification in a wide range of different fields.[2.1,2.2] Plasmas can affect a polymer in many ways depending on the composition of the gas discharge.

The simplest plasma to consider for this purpose is an inert gaseous discharge such as an Ar plasma. Some of the Ar atoms in a discharge are ionized into singly charged Ar^+ ions, with the majority of Ar atoms remaining in the neutral state. Light emission in the vacuum ultraviolet (VUV) range is also present with Ar I resonance lines (~104.8 nm and 106.7 nm) being the most intense.[2.3]

There are many interactions that can occur when a polymer is exposed to a simple Ar plasma. The various plasma constituents that can affect the polymer include positive ions, excited neutrals, electrons and UV/VUV photons.

Ion bombardment can cause drastic changes to a polymer exposed to a plasma.[2.4] Ions accelerated toward the polymer induce physical sputtering of material from the surface and collision cascades within the material. Increasing the ion energies enhance the ion effect. There is an ion energy dependent depth in which the ions penetrate within a material. In polymers, for ion energies of several hundred eV, the penetration depth is normally under ten nanometers. Depending on the type of chemical bonds the plasma-exposed material contains there can be a preferential bond breaking and selective removal of one species over another. This can cause depletion and changing of chemical composition within the penetration depth of the ions. Polymers interacting with plasma are especially affected by depletion reactions. In

general, Ar^+ ions bombarding a polymer preferentially remove hydrogen and oxygen atoms over carbon atoms, creating a carbon rich surface within the penetration depth of the ions. The modified, carbon rich surface restructures and densifies. [2.5,2.6]

VUV light is also emitted from an Ar plasma. Polymers are sensitive to VUV radiation, and the consequences depend on polymer structure and photon energy. The VUV absorption depth in polymers is dependent on the wavelength of the light and polymer type. The absorption depth is usually much larger than the penetration depth of ions, ranging from tens to hundreds of nanometers. [2.7]

Polymers have been observed to undergo various types of radiation-driven degradation mechanisms under a plasma environment. Degradation mechanisms include chain cross-linking, main-chain scission, and side chain removal. The degradation mechanism is highly dependent on the polymer structure. In one study it was found that polymers that had a hydrogen bonded opposite the side group on the carbon backbone ('α-H') was prone to cross-linking reactions while a methyl group bonded instead ('α-methyl') was prone to main-chain scission reactions.[2.8] A classic example is the difference in response between polystyrene (PS) and poly(α-methylstyrene).[2.9] However, there have been conflicting data comparing PS and PαMS and comparing other polymers with the two types of structure, with sometimes a large difference occurring and sometimes similar behavior is observed.[2.10,2.11,2.12]

Recently there has been much work done on designing polymer-based photoresist materials so that etch resistance is enhanced during the plasma pattern transfer step. Another issue is that as feature sizes become smaller, roughening in the polymer resist becomes a greater problem for successful pattern transfer. The

correlation between etch behavior and roughening behavior is still largely unknown. A dramatic recent change in photoresist polymer type took place as the UV exposure wavelength decreased from 248 nm to 193 nm.[2.13,2.14] Whereas 248 nm photoresist (PR) polymers include side groups with aromatic rings and also have the α-H structure, the 193 nm PR polymers contain adamantyl cyclic groups instead - since the aromatic rings absorb too strongly at the smaller wavelength - and also have the α-methyl structure. The 193 nm polymers typically have much lower etch resistance than 248 nm polymer and also exhibit more surface roughness as a result of plasma processing. It is not clear which factors are responsible for these differences, e.g. cross-linking versus chain scission or other structural and compositional differences.

In this article, we investigate the effect of ions and VUV radiation in a plasma on polymer films. While VUV radiation is well known to affect polymers in general, the VUV radiation from low temperature plasmas is less well characterized. This study focuses on the specific radiation effects of plasmas. Also, by comparing simple styrene- and ester-based polymers with α-H or α-methyl structures, we study the influence of polymer structure on etch and surface roughness behavior. We first describe the experimental setup in Section 2.2. In the first part of Section 2.3 (Secs. 2.3.1 – 2.3.3), we explain our experimental results for plasma exposure of polymers in low ion energy and VUV-radiation only conditions. In the second part – (Secs. 2.3.4 and 2.3.5) – we present experimental results for the case of plasma exposure with high ion energy and the characterization of the ion-damaged layer created at the polymer surface. In the final part – Section 2.3.6 – we discuss the mechanisms of plasma-polymer surface interactions based on our results.

2.2 Experimental Setup and Procedures

2.2.1 Description of Materials

In this study, various simple structure polymers were investigated to gain insight into plasma-polymer surface interactions and etch behavior. Polystyrene and its derivatives, poly(4-methylstyrene) (P4MS) and poly(α-methylstyrene) (PαMS) are linear polymers with highly etch-resistant benzene ring side-groups (see Fig. 2.1). Both P4MS and PαMS contain an additional methyl group attached. In P4MS, the methyl group is attached to the *para* side of the benzene ring side group. In PαMS, the methyl group is attached to the carbon backbone (α-carbon) on the opposite side of the benzene ring side group.

In addition, two polymers with the same backbone structure but different side groups were studied. Poly(hydroxyadamantyl acrylate) (HAdA) and poly(hydroxyadamantyl methacrylate) (HAMA) have backbone structures similar to P4MS and PαMS, respectively (see Fig. 2.1). However, instead of a benzene ring side group, both have a hydroxyadamantyl-ester side group. Poly(methyl methacrylate) (PMMA) was also synthesized to investigate ester-type polymers without the bulky adamantyl side group.

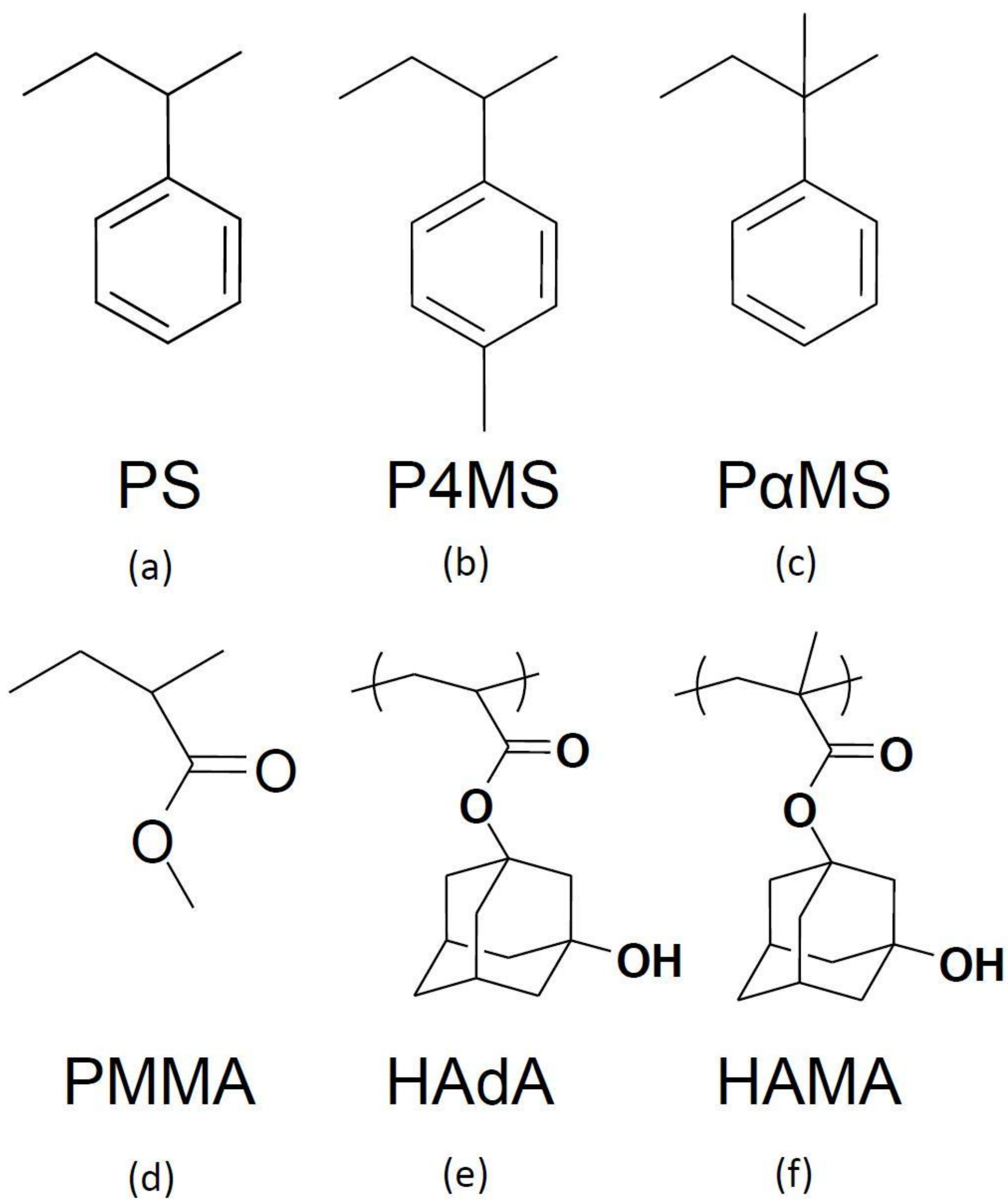

Figure 2.1: Schematics of the polymer structures are shown with their names in abbreviated form below the structures. The styrene-based polymers are (a) poly(styrene), (b) poly(4-methylstyrene) and (c) poly(α-methylstyrene). The ester-based polymers are (d) poly(methyl methacrylate), (e) poly(hydroxyadamantyl acrylate) and (f) poly(hydroxyadamantyl methacrylate).

All polymers were synthesized with similar degree of polymerization (~200) to eliminate the influence of chain length. Polymers were spin-coated onto Si wafers and baked at 90°C for 1 minute. The average thickness of the polymer films was 400 nm.

2.2.2 Plasma Processing

The inductively coupled plasma (ICP) reactor used in this study has been described in previous publications.[2.15,2.16] A planar coil is placed on top of a quartz window and powered through an L-type matching network at 13.56 MHz with a power supply (0-2000W). Ion bombardment on a 125 mm diameter substrate can be independently controlled using another bias power supply with frequency 3.7 MHz (0-250W). The distance between quartz window and substrate was 14.5 cm. The bottom electrode where the substrate is fixed is cooled at 10°C by a chiller. The base pressure achieved in the chamber before processing of each sample was 2×10^{-6} Torr. The processing conditions used were 10 mTorr operating pressure fixed by throttle valve, 40 sccm flow rate of Ar, and inductive power set to 300W. Unless otherwise indicated, 25 mm × 25 mm samples were plasma-exposed to an Ar discharge for 60 seconds. For the case of low ion energies, the bias power supply was not used. Therefore, the ion energy was determined by the plasma potential (about -20 V).[2.15] For high ion energies, the bias power was maintained at a setting that provided a self-bias voltage of -100V.

Electrons and neutrals may also contribute to surface modification during plasma exposure. The energy of electrons bombarding the polymer film is on the

order of a few eV[2.17], and this will only occur for very short periods during the RF cycle. The energy that can be deposited is likely below that required for bond breakage. The ions are accelerated to much higher energy and the deposited energy is much greater, making their impact dominant.

Thermal neutrals in pure Ar discharges are inert and their temperatures are slightly above room temperature[2.18], so there will be little chemical etching effect on the polymers. Fast neutrals can be formed in Ar discharges, and their effects will be similar to that of ions and cannot be distinguished in this work. However, the rate of formation of fast Ar neutrals is considered to be small since our operating pressure is low, creating a collision-less sheath. The excited neutrals in an Ar discharge, metastable Ar* atoms, have an internal energy around 12 eV[2.19] and may contribute to material removal by potential sputtering.

In this article we focus on the contribution of ions and VUV radiation, but this is a simplification of the actual situation since we are not explicitly addressing the contribution of electrons and energetic neutrals. Our investigation shows little material modification that can be attributed to these plasma species but that they could contribute in part to surface sputtering in the low ion energy conditions. The strong agreement of our observations and the molecular dynamics simulations that also neglect the effect of electrons and energetic neutrals indicates that their contribution must be small.

For the study in Section 2.3.1, polymer films on 25 mm × 50 mm Si substrates were placed underneath a Si structure, shown in Fig. 2.2, so that half of the polymer film was exposed to the plasma discharge and the other half was covered by either an

MgF_2 window or a Si roof. The MgF_2 window or Si roof was separated 0.7 mm from the polymer film. The polymer film thickness was measured along the 50 mm length before and after plasma exposure and the removed thickness plotted versus position. From 0 to 25 mm the polymer was fully exposed to the plasma discharge and from 25 to 50 mm the polymer was covered.

In this manner, three plasma-polymer interaction conditions could be compared: fully exposed, VUV-only, and fully covered. In the fully exposed condition, polymer films were exposed to Ar^+ ions and VUV radiation. In the VUV-only condition, the MgF_2 window shielded the polymer film from Ar^+ ion bombardment but permitted VUV light down to the cutoff wavelength (112 nm). The fully covered condition shielded the polymer film from both Ar^+ ions and VUV radiation.

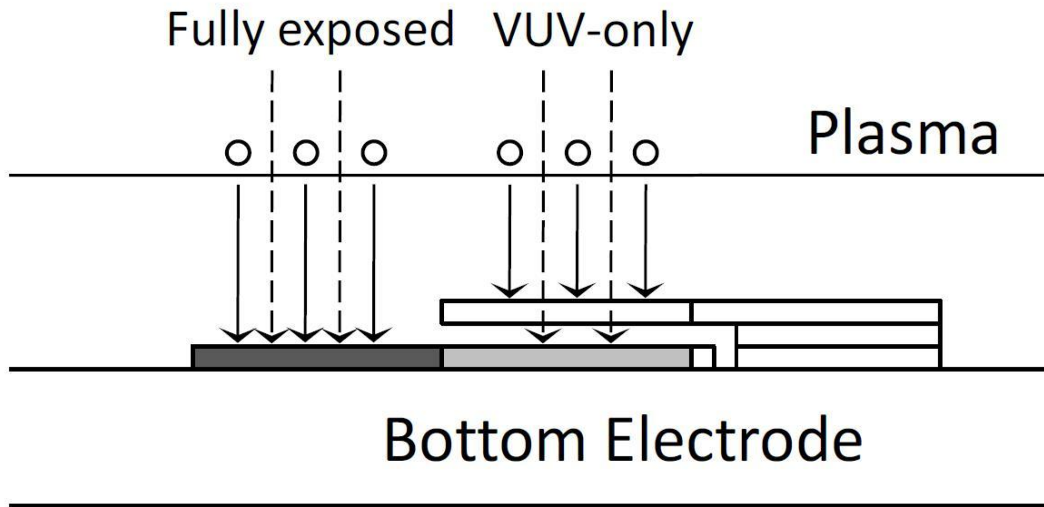

Figure 2.2: Schematic of experimental setup for fully-exposed and VUV-only conditions. Fully-covered condition replaces the UV window with a Si roof, which blocks both ions and VUV radiation. The 50 mm sample is either affixed to the bottom electrode by thermal grease, resulting in cooled conditions, or left without grease, resulting in thermally floating conditions and a fast rise in temperature from 10°C to 120°C in 2 minutes.

The effect of VUV radiation was measured by material removal and refractive index change since the VUV spectra of the Ar plasma generated by the ICP chamber was not characterized. The MgF_2 window cutoff wavelength (112 nm) is above the Ar I resonance lines, however light emission greater than 112 nm will affect the polymers.

In addition, two temperature conditions were compared: cooled and thermally floating. Cooled substrates were bonded to the bottom electrode with thermal grease. Since the bottom electrode is chilled to 10°C, the Si substrate and polymer film on top are constantly cooled during the experiment. Thermally floating substrates did not have thermal grease between the substrate and bottom electrode. The imperfect contact leaves the substrate thermally isolated and the energy deposition due to Ar^+ ion bombardment and VUV radiation will heat the substrate and polymer film on top. The temperature of the thermally floating substrate increases linearly with time. It was calculated that the substrate temperature increased ~1°/sec under these discharge conditions and substrate geometry.

For the measurement of root mean square (RMS) roughness by atomic force microscopy versus plasma exposure time, gradient samples were processed. They were processed in another ICP chamber supplied with a 0-2000W 13.56 MHz power supply. The samples being etched were placed atop a 300 mm diameter Si electrode which can be independently biased using a 0-1000W 13.56 MHz power supply. The electrode temperature is fixed at 10°C using a chiller. The chamber walls are fixed at 50°C using heating straps. The base pressure achieved before processing of each

sample was 5×10^{-5} Torr. The processing conditions used were 10 mTorr operating pressure fixed by throttle valve, 50 sccm flow rate, and inductive power set at 400W. The conditions for the 300 mm ICP chamber were chosen to produce similar plasma etch results as the 125 mm ICP chamber. A shutter approach is used to create a sample that has been exposed from 0 to 60 seconds over the length of the sample. The shutter approach method is explained in a previous publication.[2.13]

2.2.3 Surface Characterization

The thickness and optical properties (refractive index and extinction coefficient) of the polymer films were measured *in situ* during plasma processing using a SOFIE STE70 He-Ne ellipsometer. The ellipsometer is an automated rotating compensator ellipsometer working in the polarizer-compensator-sample-analyzer (PCSA) configuration. The angle of incidence was 71.3° and for the simulation of ellipsometric data the Si substrate refractive index was fixed at 3.866-0.028i. The ellipsometer measures two angles that describe the relative change in amplitude (Ψ) and change in phase (Δ) of an electric field vector upon reflection.[2.20] Ψ and Δ were measured and can be related to fundamental physical properties of the polymer film such as thickness, refractive index, and extinction coefficient by using an optical model and solving the Fresnel reflection coefficients for the physical property values.[2.20]

X-ray photoelectron spectroscopy (XPS) analysis was performed in a Vacuum Generators ESCA Mk II surface analysis chamber using a nonmonochromatized Al Kα X-ray source (1486.5 eV). 25 mm × 25 mm samples were transferred in air

immediately after processing. Spectra were obtained under 90° emission angle relative to the surface and in constant analyzer energy (CAE) mode at 20 eV pass energy. The analyzer resolution was approximately 0.2 eV and the resolution of the spectra was limited by the linewidth of the X-ray source, approximately 1 eV.

Raman spectroscopy analysis was performed on unexposed and processed samples in a Horiba Jobin-Yvon LabRAM HR-VIS microRaman system using a 633 nm laser wavelength.

Atomic force microscopy (AFM) measurements were performed on unexposed and processed samples. Processed samples were transferred to the AFM in air. The scan size for all measurements was fixed at $2 \times 2\ \mu m^2$. The surface roughness values reported were calculated from the root mean square (RMS) of the surface profile after the measurement.

Molecular dynamics (MD) simulations of 100 eV Ar^+ ions bombarding a model polystyrene surface were performed and are explained in depth in a previous publication.[2.4] The simulation cell contained 9 polystyrene chains, each consisting of 20 monomers, for a total of 2880 atoms. The initial spacing of the polymer chains was chosen so that the density was the same as bulk polystyrene (1.06-1.12 g/cm^3). The model polystyrene system was allowed to equilibrate at 300K for several tens of picoseconds to yield a relaxed surface. Further details of the simulations are presented elsewhere.[2.4]

2.3 Results and Discussion

2.3.1 Empirical Study of the Contribution of Ions, VUV Radiation and Temperature to Polymer Modification by Ar Plasma

The combined effect of ions and VUV radiation and the effect of VUV radiation only in a pure Ar discharge on the removed thickness of polymer films were examined. In Fig. 2.3(a), the film thickness removed in P4MS and PαMS on cooled substrates was compared under fully exposed, VUV-only, and fully covered conditions. Fully exposed, P4MS and PαMS showed similar, low removed thickness. In the fully covered and VUV-only conditions, there is negligible removed thickness in both polymers.

In Fig. 2.3(b), the film thickness removed in P4MS and PαMS on thermally floating substrates was compared under fully exposed, VUV-only, and fully covered conditions. Polymer films on thermally floating substrates heated from 10°C at 0 seconds to 120°C in 120 seconds. P4MS showed values of removed thickness similar to cooled conditions. Unlike P4MS, the thickness removed in PαMS increased significantly in all three heated conditions. Furthermore, in the fully exposed and VUV-only conditions, PαMS showed a similar amount of thickness removed.

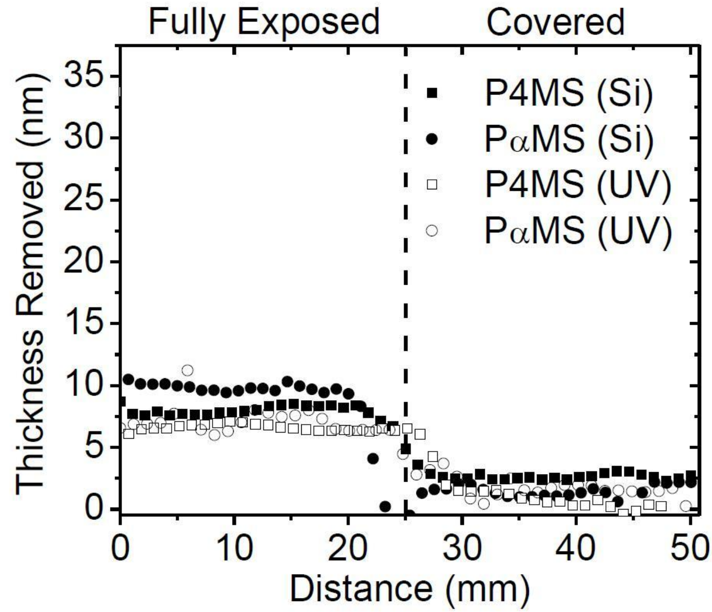

(a)

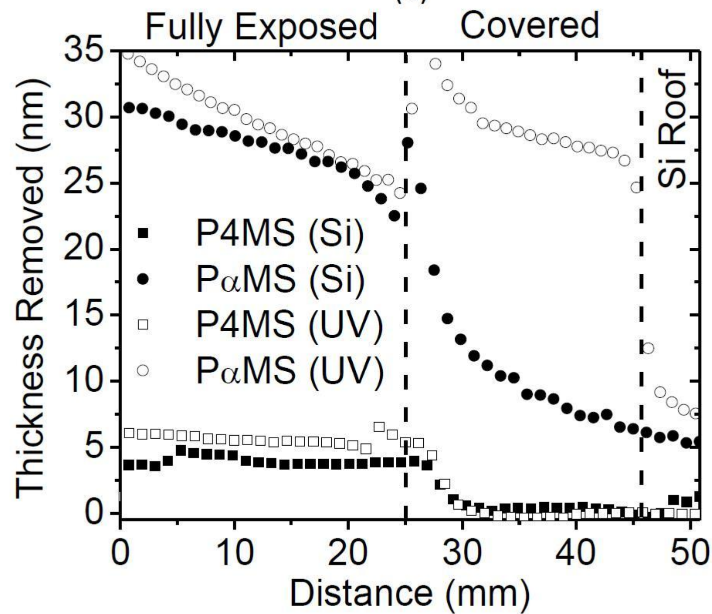

(b)

Figure 2.3: Thickness removed along P4MS and PαMS samples that were partially exposed to Ar plasma and partially covered by a MgF_2 UV window or Si roof at low temperature conditions (a) and high temperature conditions (b). Samples at fixed low temperatures were bonded to the chilled bottom electrode (10°C) with thermal grease. Samples without thermal grease heated with time from 10°C at plasma start to 120°C after 2 minutes of plasma exposure. Ar discharges were generated using 300W source power, 10 mTorr pressure, 40 sccm gas flow, no RF bias, and 2 minutes plasma exposure time.

From the overall etch behavior of P4MS and PαMS, a number of observations can be made. P4MS and PαMS on cooled substrates show pure physical sputtering behavior. That is, Ar^+ ion bombardment is the main factor in material removal. VUV-only and fully covered conditions show negligible film thickness removed indicating that VUV radiation does not contribute to material removal. Both polymers exhibit little removed thickness in fully exposed conditions due to the high etch resistance of the pendant aromatic ring that both contain. They show similar removed thickness because of their identical chemical composition.

On thermally floating substrates, with rapid heating of the polymer films, there is a difference in etch behavior between P4MS and PαMS. P4MS continued to show pure physical sputtering behavior. Similar removed thickness in the fully exposed condition and negligible removed thickness in the VUV-only and fully covered conditions are found between cooled and thermally floating substrates.

PαMS, however, showed a significant increase in removed thickness at the thermally floating condition compared to the cooled condition. In the fully exposed condition, the removed thickness increased from 8.44±0.56 nm on the cooled substrate to 28.72±2.5 nm on the thermally floating substrate. The drastic increase in removed thickness may be explained by considering the VUV-only condition. Even with the MgF_2 window protecting the polymer film from ion bombardment, a comparable removed thickness is found between fully exposed and VUV-only conditions. Therefore, the enhanced removed thickness in PαMS is due to the combination of VUV radiation and elevated temperature. Even in the fully covered condition, PαMS shows 8.22±2.29nm removed thickness. This may be due to the

high reactivity of PαMS at elevated temperatures and also stray VUV light that may penetrate under the Si roof from the side.

Therefore, PαMS undergoes VUV photodegradation at elevated temperature while P4MS remains stable. It has been reported that, generally, polymers with a methyl group on the backbone α-carbon will be prone to chain scission reactions, while polymers with a hydrogen at this position will be prone to crosslinking reactions when exposed to ionizing radiation.[2.9] Since PαMS contains the former structure and P4MS contains the latter structure, the difference in removed thickness at elevated temperature might be caused by this general structural difference and response. We tested this by comparing the removed thickness of HAdA and HAMA under fully exposed and VUV-only conditions on thermally floating substrates. HAdA and P4MS have the same α-H structure and, likewise, HAMA and PαMS have the same α-methyl structure. Unlike P4MS and PαMS, HAdA and HAMA contain an adamantyl ester sidechain instead of an aromatic ring.

Figure 2.4(a) shows the removed thickness in P4MS, PαMS, HAdA, HAMA, and PMMA on thermally floating substrates under fully exposed and VUV-only conditions. HAdA and HAMA show, unlike P4MS and PαMS, similar removed thickness in the fully exposed and VUV-only conditions. Also, both polymers show a finite removed thickness (2.87±0.49 nm for HAdA, 4.02±0.31 nm for HAMA) under VUV-only conditions.

It is possible that the similar etch behavior between HAdA and HAMA is due to the heavy adamantyl ester chain that may keep any chain scission products from volatilizing in HAMA. To determine if this is the case, PMMA was also exposed and

the removed thickness is shown in Fig. 2.4(a). PMMA shows a much greater removed thickness than HAdA and HAMA. In the fully exposed condition, PMMA shows the greatest removed thickness (72.18±1.30nm) compared to the other polymers. In the VUV-only condition, PMMA shows half the amount of removed thickness (35.05±1.83nm) as the fully exposed condition.

Comparing PαMS to HAMA and PMMA, all polymers with a methyl group on the α-carbon, shows that only PαMS has equivalent amount of removed thickness in the fully exposed and VUV-only conditions. Therefore, in conditions of elevated temperature, most of the removed thickness of PαMS can be attributed to VUV radiation while for HAMA and PMMA there is a significant amount of thickness removed by physical sputtering by ions and ion-induced gasification processes.

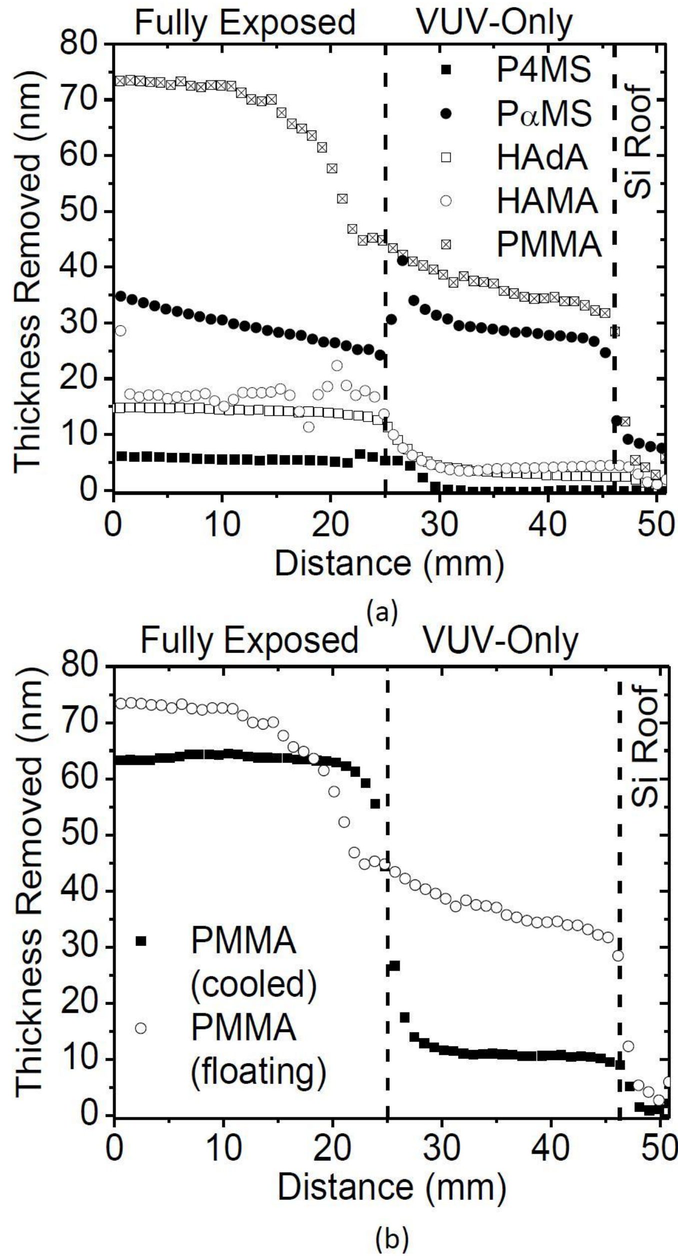

Figure 2.4: Thickness removed along 248nm-Type (P4MS and PαMS) and 193nm-Type (HAdA, HAMA, and PMMA) polymer samples that were partially exposed to Ar plasma and partially covered by a MgF_2 UV window high temperature conditions is shown in (a). In (b), the thickness removed in the plasma exposed region and the UV window covered region are compared at low temperature and at high temperature. Samples at fixed low temperatures were bonded to the chilled bottom electrode (10°C) with thermal grease. Samples without thermal grease heated with time from 10°C at plasma start to 120°C after 2 minutes of plasma exposure. Ar discharges were generated using 300W source power, 10 mTorr pressure, 40 sccm gas flow, no RF bias, and 2 minutes plasma exposure time.

The removed thickness of PMMA was compared under fully exposed and VUV-only conditions on cooled and thermally floating substrates in Fig. 2.4(b). The removed thickness was lower in both the fully exposed and VUV-only conditions when the substrate is cooled. However, there was still a significant amount of thickness removed under cooled, VUV-only conditions (10.79±0.34nm). This is in sharp contrast to the etch behavior of PαMS, where only at elevated temperatures did VUV-only conditions show any impact on removed thickness.

From Figs. 2.3 and 2.4 a number of insights can be gained about the contributions of ion sputtering, VUV radiation, and temperature on material removal in polymers under plasma exposure. Over the temperature range of 10°C to 120°C, temperature does not affect the amount of material removed by ion sputtering. Also, more material is sputtered by ions when the polymer contains more oxygen. Therefore, if only ion sputtering is considered, the thickness removed of polymers would follow the trend: P4MS, PαMS (0% O) < HAdA (8.8% O), HAMA (8.1% O) < PMMA (13.3% O).

The effect of VUV radiation is highly polymer specific and temperature dependent. For PαMS, elevated temperature is required to induce material removal by VUV radiation. However, PMMA shows significant VUV-only material removal even at near room temperature. VUV-only material removal in PMMA is enhanced at elevated temperature. Therefore, there is a possible difference in material removal mechanism between PαMS and PMMA. PαMS also shows material removal caused mostly by VUV radiation while PMMA shows only a portion of material removal caused by VUV radiation at elevated temperatures with the remaining removal rate

explained by ion sputtering. This would further support a difference in material removal mechanisms between the two polymers.

HAdA and HAMA also show only a portion of material removal caused by VUV radiation and both show similar removed thickness under fully exposed and VUV-only conditions at elevated temperatures. Therefore, the difference in methyl group or hydrogen on α-carbon on the polymer backbone does not bring about a difference in removed thickness in HAdA and HAMA like in P4MS and PαMS.

The effect of VUV radiation on ester-based polymers such as HAdA, HAMA, and PMMA is possibly dependent on amount of oxygen in the polymer just like ion sputtering. The greatest amount of VUV-only removed thickness is in PMMA (13.3% O), while for HAdA (8.8% O) and HAMA (8.1% O) the removed thickness is much less but still present.

Overall, it does not seem that the minimal difference between the removed thickness of HAdA and HAMA can be explained by the presence of heavy adamantyl-ester groups that inhibit volatilization. The etch behavior of both polymers and PMMA appear to be dependent on amount of oxygen in the polymer. This mechanism of material degradation may occur first, changing the polymer structure so that the chain scission versus crosslinking reaction based on backbone structure can no longer occur.

Figure 2.5 shows the RMS roughness of the polymers after plasma exposure for fully exposed and VUV-only conditions at elevated temperature. All polymers under VUV-only conditions exhibited very little roughness, similar to RMS roughness values of the virgin polymer films. Only under fully exposed conditions

and the introduction of ion bombardment did roughening occur. PαMS showed very high RMS roughness in the fully exposed case, and HAdA and PMMA showed a slight increase in the RMS roughness. P4MS and HAMA showed no change in RMS roughness compared to VUV-only condition. It is unclear how roughening evolves in each polymer structure, but the contribution of ion bombardment seems necessary for any roughening to occur. These results are in agreement with ion beam processing work reported by Nest, et al.[2.21] They showed that surface roughening in polymer films required the combined effects of VUV exposure, ion bombardment and heating.

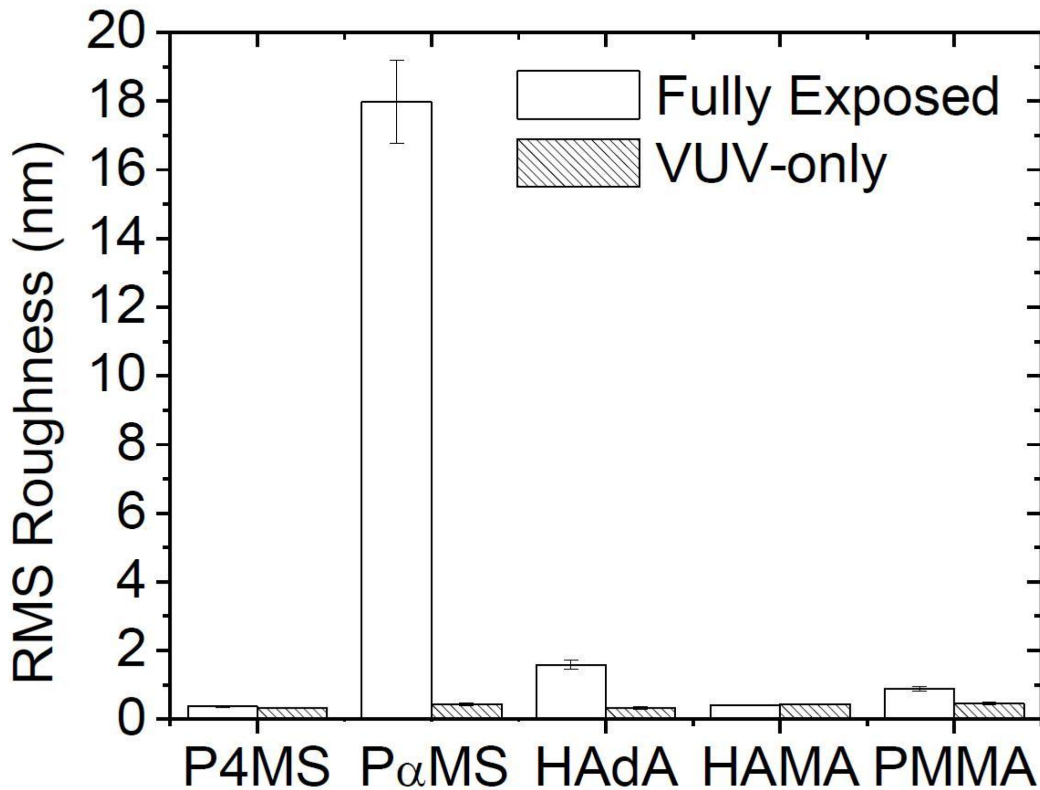

Figure 2.5: Etch-induced RMS roughness of polymers after plasma exposure for full exposed and VUV-only conditions. Samples without thermal grease heated with time from 10°C at plasma start to 120°C after 2 minutes of plasma exposure. Ar discharges were generated using 300W source power, 10 mTorr pressure, 40 sccm gas flow, no RF bias, and 2 minutes plasma exposure time.

2.3.2 Dependence of Etch Rate on Temperature and Polymer Degradation

In situ measurements of etch rate versus plasma exposure time are plotted in Figs. 2.6(a)-(c). Samples were thermally floating and exhibited a rise in temperature with plasma exposure time linearly from 10°C to 60°C after 1 minute. In order to look at the effect of plasma exposure on polymer degradation, samples were exposed to the plasma four consecutive times. The samples were exposed to the Ar plasma for 1 minute and left to cool for five minutes before another 1 minute plasma exposure.

Data for P4MS are shown in Fig. 2.6(a). As the thermally floating sample temperature increases, the etch rate remains the same. Also, the same low etch rate is observed during each subsequent plasma exposure. PαMS, shown in Fig. 2.6(b), exhibits different behavior. The etch rate at low temperature has a low value similar to P4MS. However, the etch rate rises rapidly with temperature. This dependence of etch rate with temperature is reproduced during each subsequent plasma exposure. PMMA, shown in Fig. 2.6(c), exhibits even more complex behavior. Almost immediately during the first plasma exposure, PMMA shows an extremely high etch rate. The etch rate quickly decreases, but then increases again as the temperature increases. In the next plasma exposure, the initial high etch rate no longer appears, however the etch rate continues to increase with temperature, but overall etch rates are lower than during the first plasma exposure. The next two plasma exposures show a continual decrease in overall etch rates.

P4MS shows little change in etch rate with temperature indicating that the polymer properties do not change within the temperature range of 10°C to 60°C. This is consistent with the result in Section 2.3.1, which showed that the removed

thicknesses for thermally floating samples were no different than for cooled samples. P4MS also shows no change in etch behavior during each subsequent plasma exposure. This indicates that there is little degradation that occurs to P4MS under plasma exposure at these conditions.

PαMS shows a steep rise in etch rate with temperature, which would indicate a change in polymer properties in this temperature range. At the beginning of the next plasma exposure, the etch rate returns to the same low etch rate as in the beginning of the first plasma exposure and increases with temperature in the same manner. The reproducibility of this behavior during each subsequent plasma exposure indicates that even though the polymer properties change with temperature, there does not seem to be any permanent change occurring to the bulk polymer properties of PαMS that would affect etch rate. From the results found in Section 2.3.1 it can be assumed that the etch rate increase with temperature is mostly due to VUV radiation.

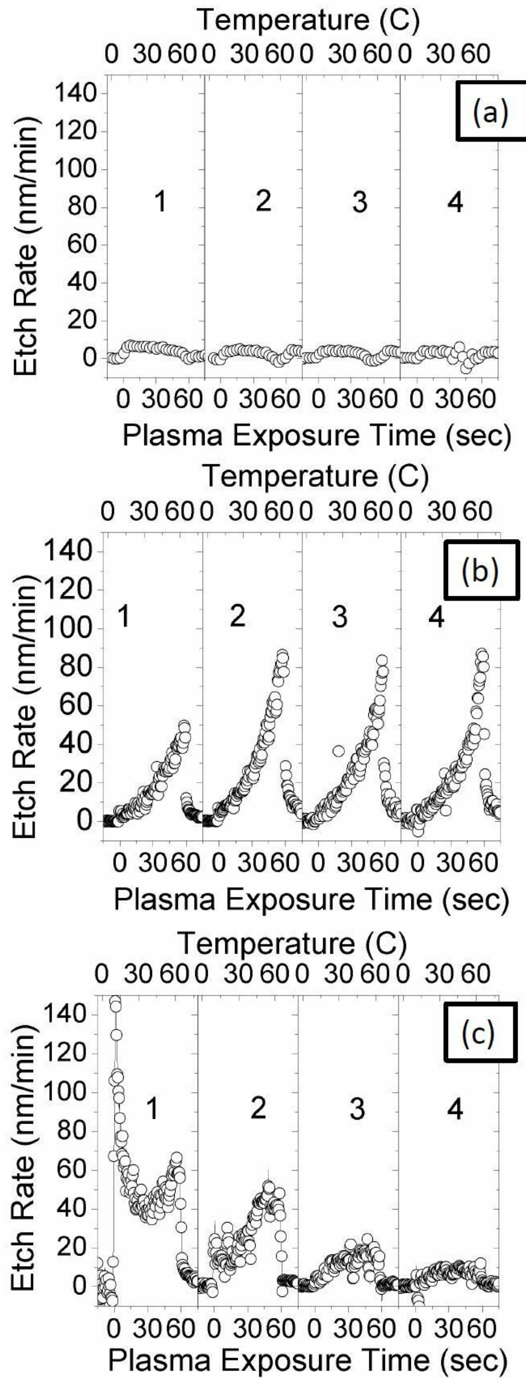

Figure 2.6: Etch rate of P4MS (a) PαMS (b) and PMMA (c) samples as a function of plasma exposure time. While the plasma is on, the thermally floating samples rise in temperature. After 60 seconds, the plasma is turned off and the samples are cooled down for 5 minutes. The samples are exposed to the plasma three more times with 5 minute cooling in between each run. Ar discharges were generated using 300W source power, 10 mTorr pressure, 40 sccm gas flow, no RF bias, and 2 minutes plasma exposure time.

In section 2.3.1, Fig. 2.4(b) showed that the majority of thickness removed for PMMA is caused by ion sputtering at low temperature. The increase in removed thickness at elevated temperature is small. The VUV-only contribution to removed thickness at low temperature is small, while at elevated temperature the VUV-only contribution is greatly enhanced. This is supported in Fig. 2.6(c). The highest etch rate in PMMA is at the beginning of the first plasma exposure at low temperature. Therefore, ion sputtering occurs initially providing the greatest amount of material removal. The disappearance of this initial high etch rate in subsequent plasma exposures shows that PMMA is permanently changed after the initial ion sputtering event. For the first plasma exposure, as the temperature increases, the etch rate begins to increase. Comparing the results to Fig. 2.4(b) in Section 2.3.1, this would correspond to material removal caused by VUV-only radiation. The increase in etch rate is also seen in subsequent plasma exposures, but the overall etch rates decrease showing that VUV-only radiation is also permanently damaging PMMA. During the fourth plasma exposure, the etch rate is low and constant with temperature, possibly due to the polymer structure of PMMA having been completely changed.

2.3.3 Ellipsometric Analysis of Ar Plasma Etched Polymers at Fixed Low Temperature

While the empirical study in Section 2.3.1 shows the contribution of plasma species to thickness removed, additional polymer modification can be observed through ellipsometric data analysis. Figure 2.7(a) shows the *in situ* ellipsometric data of P4MS and PαMS on cooled substrates exposed to an Ar plasma for 2 minutes. The

time of etch is indicated to show the path of Ψ and Δ trajectory as a function of time. At 0 seconds, the polymers have not been affected by the plasma and have properties of the unexposed polymers. After plasma exposure, there will be a change in the properties of the polymers due to change in film thickness and change in optical properties (i.e. refractive index (n) and extinction coefficient (k)). If the polymer is eroded but there is no material modification which would change its optical properties, there will be a characteristic Ψ-Δ trajectory that a polymer film will follow with change in thickness. In Fig. 2.7(a), the simulated characteristic Ψ-Δ trajectory for bulk P4MS and PαMS is shown. At 632.8 nm, unexposed P4MS has a refractive index of 1.582 while PαMS has a slightly higher refractive index of 1.602.

For P4MS, when exposed to an Ar plasma with no RF bias, the Ψ-Δ trajectory follows the bulk P4MS Ψ-Δ trajectory. This indicates that as thickness is removed from P4MS, there is very little material modification and the optical properties of the exposed P4MS are similar to unexposed P4MS. The Ar-exposed Ψ-Δ trajectory follows the bulk P4MS Ψ-Δ trajectory for the whole 2 minutes of plasma exposure time.

PαMS shows a different behavior. Immediately after turning on the Ar plasma, the Ψ-Δ trajectory deviates from the bulk PαMS Ψ-Δ trajectory. In this area of the Ψ-Δ trajectory, a deviation above the bulk Ψ-Δ trajectory corresponds to an increase in the optical constants n and k of the film. Furthermore, a deviation normal to the bulk Ψ-Δ trajectory corresponds to an increase in the optical properties of the overall film with little change in overall thickness.

The nature of the material modification of PαMS is considered. When the VUV-only exposed samples of PαMS are examined, they show the same increase in optical properties which would suggest that modification is purely due to VUV radiation. Also, under these particular plasma conditions with no RF bias the ion energy is ~20 eV, which would produce a negligible damaged layer as measured by the ellipsometer. This is evident since there is no change in optical properties in P4MS under no RF bias condition while there is a definite change in optical properties when the ion energy is increased, as is discussed in Section 2.3.5.

Polystyrene shows a VUV penetration depth of ~30 nm in the most absorbing region[2.22] and it is known that PαMS has an almost identical VUV absorbance spectra.[2.23] Therefore, the creation of a 30 nm densified layer during plasma exposure was considered. It was assumed that after establishing this layer during the plasma process, the layer would reach steady state in terms of layer thickness and optical properties while the undamaged layer underneath would continue to decrease in thickness. A refractive index of 1.727 provided the best fit for the 30 nm VUV damaged layer to the experimental Ψ-Δ trajectory.

Therefore, PαMS shows different behavior under VUV radiation at low temperature and at high temperature. At low temperature, VUV radiation causes densification in the top 30 nm of material. At high temperature, VUV radiation causes rapid removal of material and drastic thickness loss is observed. Both types of reactions may be explained by chain scission reactions. At low temperature, VUV radiation causes chain scission in the polymer chains that at low temperature crosslink.

However, at high temperature crosslinking does not occur and chain scission creates volatile products that are removed under vacuum.

For comparison, HAdA and HAMA on cooled substrates were also exposed to Ar plasma under no RF bias power condition and their Ψ-Δ trajectories are shown in Fig. 2.7(b). They show similar etch behavior where there is a deviation from bulk properties corresponding to densification at the surface. Unlike PαMS where the deviation at the beginning is normal to the bulk trajectory, the Ψ-Δ trajectory of plasma-exposed HAMA and HAdA corresponds to an increase in optical properties in conjunction with high thickness loss. It is possible that this etch behavior is characteristic of the ester-based polymers.

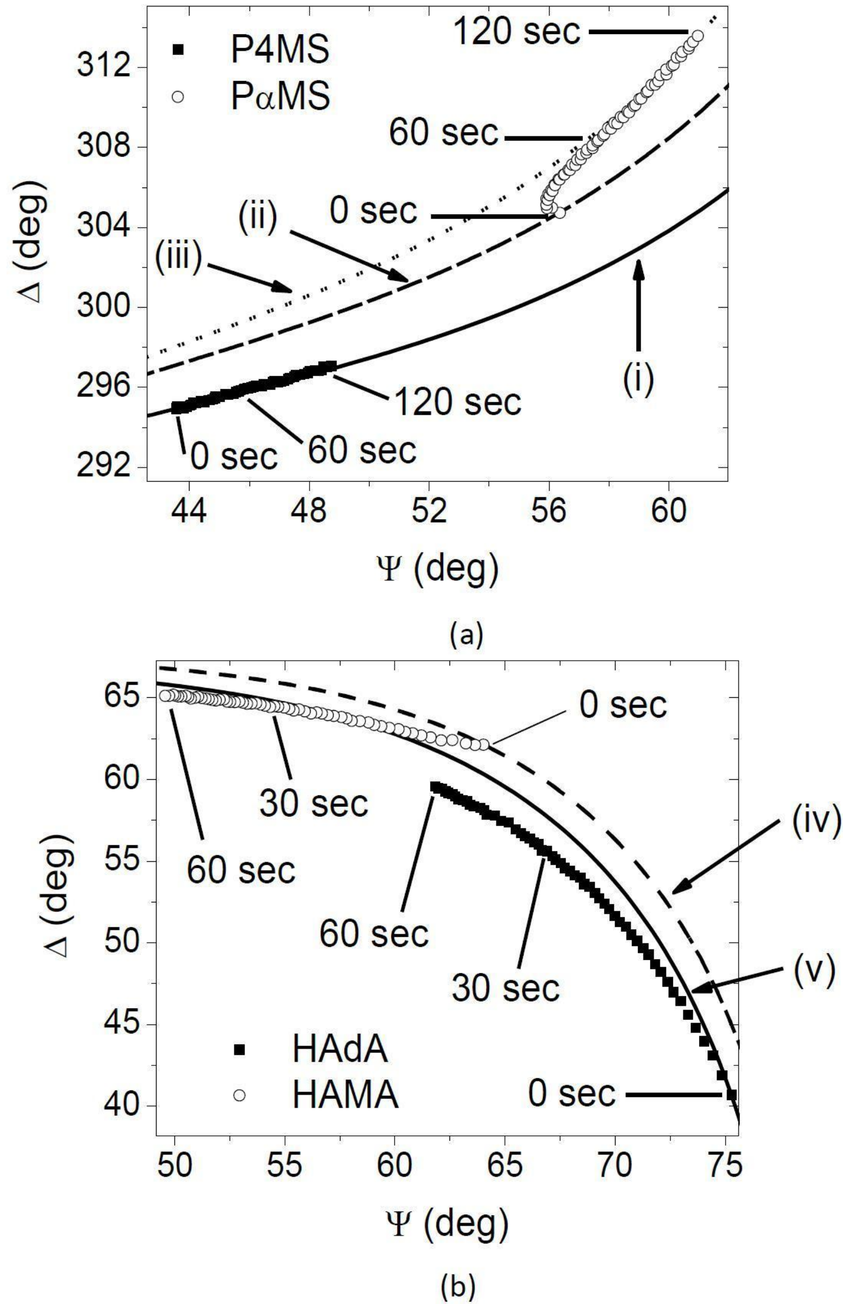

Figure 2.7: Ψ-Δ plots of P4MS and PαMS (a) and HAdA and HAMA (b) exposed to Ar discharges are shown. The Ψ-Δ simulated trajectories of unexposed P4MS (i), PαMS (ii), HAdA (iv) and HAMA (v) with varying thickness and constant refractive index are shown for comparison. Also, the Ψ-Δ simulated trajectory for a constant 30nm UV modified layer on top of a varying thickness of unexposed PαMS (iii) is shown in (a). Ar discharges were generated using 300W source power, 10 mTorr pressure, 40 sccm gas flow, and no RF bias.

In Fig. 2.8 the etch rate versus plasma exposure time is shown for P4MS, PαMS, and the three ester-based polymers: HAdA, HAMA, and PMMA. Comparing P4MS and PαMS, PαMS has slightly higher initial etch rate but after 15 seconds decreases to the same etch rate values as P4MS. The etch rates of both styrene polymers become constant at about 5 nm/min. HAdA and HAMA show an enhanced initial etch rate compared to the styrene polymers and drop to 10 nm/min. PMMA shows an even greater initial etch rate and drops to 20 nm/min. The increased initial etch rate and increased steady state etch rate correspond with the amount of oxygen.

The etch behavior of HAdA and HAMA are similar to PMMA in that they all show an initial high etch rate which decreases to a constant, steady state value. However, since HAdA and HAMA have significantly lower oxygen content compared to PMMA, the overall etch rate values are considerably reduced. We assume that the mechanism of material removal for all ester-based polymers to be the same. Therefore, the high etch rate at the beginning of exposure corresponds with oxygen depletion at the surface due to ion bombardment. Once the etch rate reaches a low, steady state value, the ester-based polymers continue to show a difference in etch rate that appears to be determined by the oxygen content in the polymer.

It is well known that hydrogen is preferentially removed over carbon in polymers under high energy ion bombardment.[2.4] A high etch rate is generally observed initially as hydrogen is depleted and a carbon-rich layer is formed at the surface. An in depth discussion of this effect will be presented in Section 2.3.4. However, only a slightly higher initial etch rate is observed in PαMS and none is

observed for P4MS as shown in Fig. 2.8. This is because no RF bias is used in these plasma conditions and ions in the plasma have relatively low energy (~20 eV). At low ion energies, the affected volume under ion bombardment is small because the penetration depth of the ions is small. While oxygen depletion is still observable under these conditions, hydrogen depletion is almost negligible. The slightly higher initial etch rate in PαMS is possibly due to VUV modification, which has a greater affected volume as the penetration depth is much deeper.

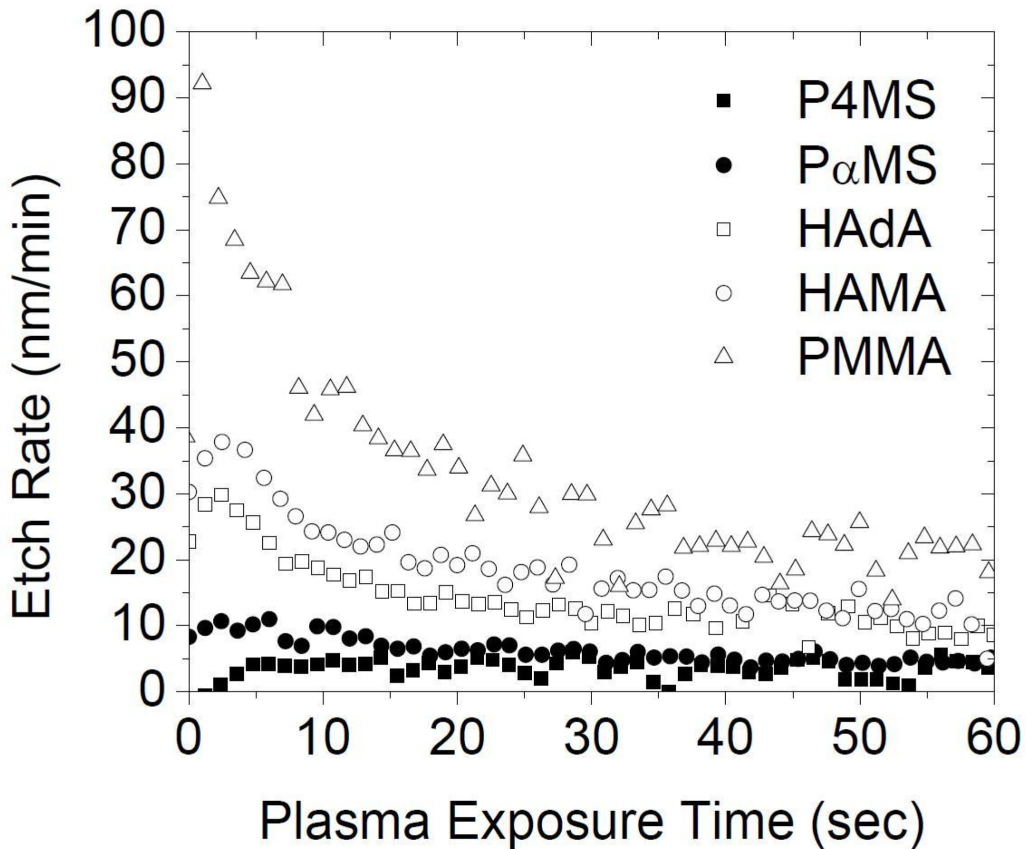

Figure 2.8: Etch rate versus plasma exposure time for P4MS, PαMS, HAdA, HAMA, and PMMA under Ar plasma discharge. Ar discharges were generated using 300W source power, 10 mTorr pressure, 40 sccm gas flow, no RF bias, and 1 minute plasma exposure time.

2.3.4 Characterization of Polymer Surface Modification by High Energy Ions

Several methods were used to characterize the polymer surface under high energy ion bombardment. It was reported in Ref. 2.4 that under 100 eV Ar^+ ion bombardment, a heavily crosslinked, dehydrogenated damage layer is formed at the polymer surface. Once steady state has been reached, the properties of the damage layer remain the same. For a model polystyrene surface, the damage layer was characterized after the system had reached steady state. The damage layer thickness was 1.61 nm.[2.4] This layer had a hydrogen content of 9.9%H and a density of 2.44 g/cm^3. A sideview image of the model polystyrene surface after steady-state is reached is shown in Fig. 2.9(a).

In an inductively coupled plasma, the ion energies can be independently controlled by increasing the RF bias power. In the ICP chamber, a polystyrene film was exposed to an Ar plasma at standard conditions but with an increased RF bias power so that the ion energy was maintained at 100 eV. The Ψ-Δ trajectory was measured and is shown in Fig. 2.9(b). At the beginning of plasma exposure, there is a quick deviation from the simulated bulk polystyrene trajectory, corresponding to an increase in the overall optical properties.

It was assumed that under an Ar plasma with 100 eV ions, polystyrene would only be modified by ions. Therefore, there would be no modification effect from VUV radiation, or chemical interaction with neutrals. These assumptions can be made since polystyrene and P4MS have nearly identical radiation-driven degradation

behavior[2.9] and, as was shown in Section 2.3.1 and 2.3.3, P4MS shows negligible effects from VUV-only conditions.

Therefore, the optical model that can reproduce the observed ellipsometric behavior was a two layer model with a constant thickness damage layer created by ion bombardment and a bulk polystyrene layer underneath that decreased during plasma exposure. The optical model was fitted with the experimental Ψ-Δ trajectory using 1.61 nm as the constant damage layer thickness and varying the refractive index and extinction coefficient of the damage layer.

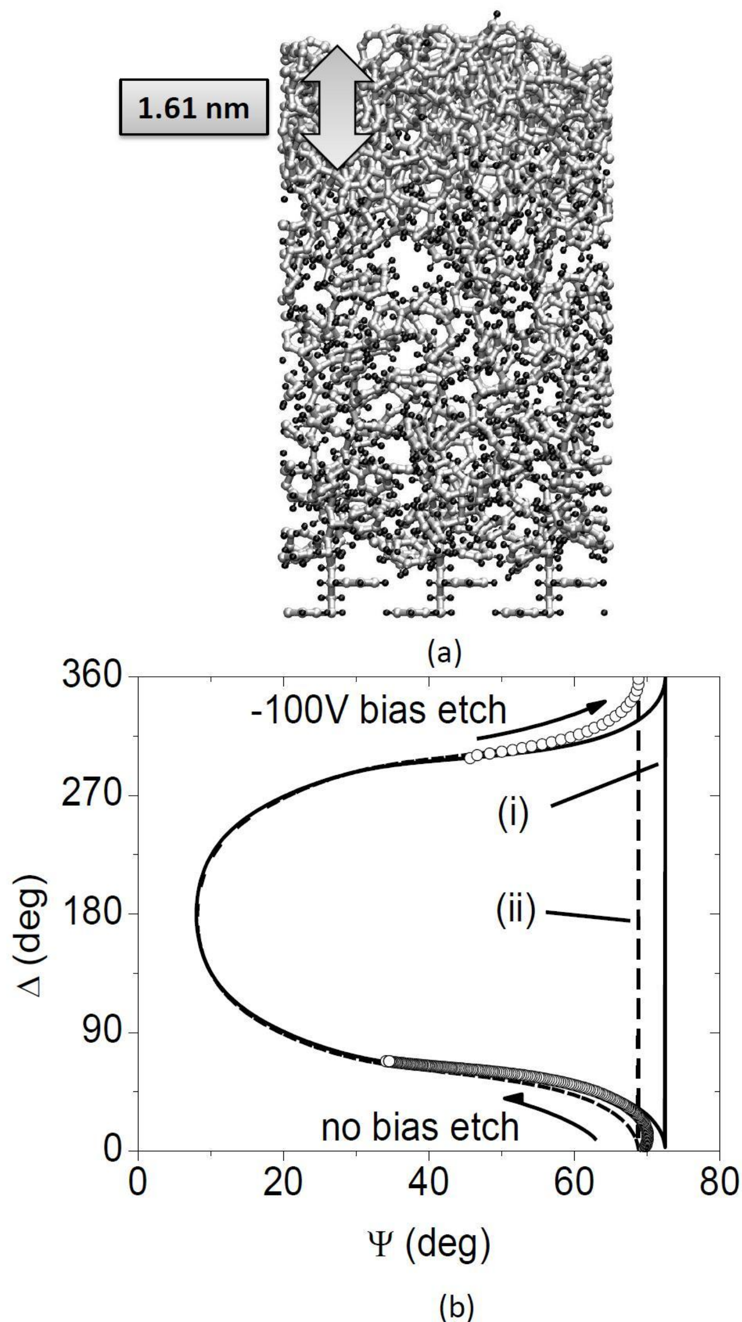

Figure 2.9: (a) Side view MD simulation image of PS after ~7800 impacts of 100 eV Ar^+ ions. The estimated thickness of the densified layer at the surface is 1.61nm. (b) Ψ-Δ plot of PS etched by Ar plasma with -100V bias and then etched again with no bias. Also shown are simulated trajectories of unmodified PS (i) and PS with a constant 1.61nm thickness damage layer and complex refractive index 2.39-0.4i (ii). Ar discharges were generated using 300W source power, 10 mTorr pressure, 40 sccm gas flow, -100V RF bias, and 1 minute plasma exposure time.

Hopf, et al.[2.24] showed a relationship between refractive index and extinction coefficient for amorphous carbon. It was assumed that the damage layer had similar properties to amorphous carbon so that the fit between the optical model and experimental data required varying only one independent variable. It can be seen that with refractive index 2.39 and extinction coefficient -0.4i, a simulated trajectory can be made that satisfies the experimental Ψ-Δ trajectory.

In addition, Hopf, et al. also showed a dependence of the optical properties on hydrogen content and density. This relationship can be used to deduce hydrogen content and density for the damaged layer seen in the ellipsometric measurements. For a refractive index n-ik of 2.39-0.4i, the hydrogen content is 15.8%H and density is 2.41 g/cm^3. These values are in agreement with the values of 9.9%H and 2.41 g/cm^3 calculated for the steady-state dehydrogenated layer measured using MD simulation.

Plasma processed polystyrene samples were also analyzed using X-ray photoelectron spectroscopy (XPS) and Raman spectroscopy. Polystyrene samples were processed under standard conditions with adjusted bias power so that the ion energy was 100 eV. Using XPS, the valence band spectrum was analyzed before and after processing. This is shown in Fig. 2.10(a). Before processing, the polystyrene valence band showed peaks that correspond to σ bonds in various configurations that change the binding energies of the valence electrons slightly. These peaks are characteristic of polystyrene. After processing, there was a decrease in σ bonds and an increase in lower binding energies that correspond to π bonds. The increase in π

bonding is possible if hydrogen is depleted in the layer and the remaining carbon established new bonds with each other, restructuring the layer. This would cause an increase in the sp^2/sp^3 ratio, giving the modified layer an increase in graphitic character. This result is similar to what was shown by Terrasi, et al.[2.25]

This interpretation is further confirmed by Raman analysis, as shown in Fig. 2.10(b). The Raman spectrum for unexposed polystyrene and polystyrene exposed to standard Ar plasma conditions with 150 eV ion energy was examined. At an ion energy of 150 eV a damage layer is created that is thick enough for detection by Raman spectroscopy. Between 1200 and 1800 cm^{-1} are located the disordered (D) and graphite (G) peaks of amorphous carbon.[2.26] With greater graphite crystallinity, the G peak becomes large. A greater mix of sp^2 and sp^3 bonds causes the D peak to become larger. For the unexposed polystyrene, there are no peaks present in this range. This is a reasonable result due to the amorphous nature of polystyrene. After exposure to Ar plasma at high RF bias power conditions, there is an appearance of D and G peaks. This further supports that graphitization occurs at the surface of polystyrene after Ar^+ ion bombardment in a plasma process.

2.3.5 Ellipsometric and Roughening Behavior of Ar Plasma Etched Polymers at High RF Bias

P4MS and PαMS under 100 eV Ar^+ ion bombardment were also modeled by MD simulation and the damage layer thickness and density for both polymers and polystyrene are shown in Table 2.1. The damage layer properties were very similar for all polymers. For fitting the experimental data of processed P4MS and PαMS, the damage layer thickness provided by MD simulation was used.

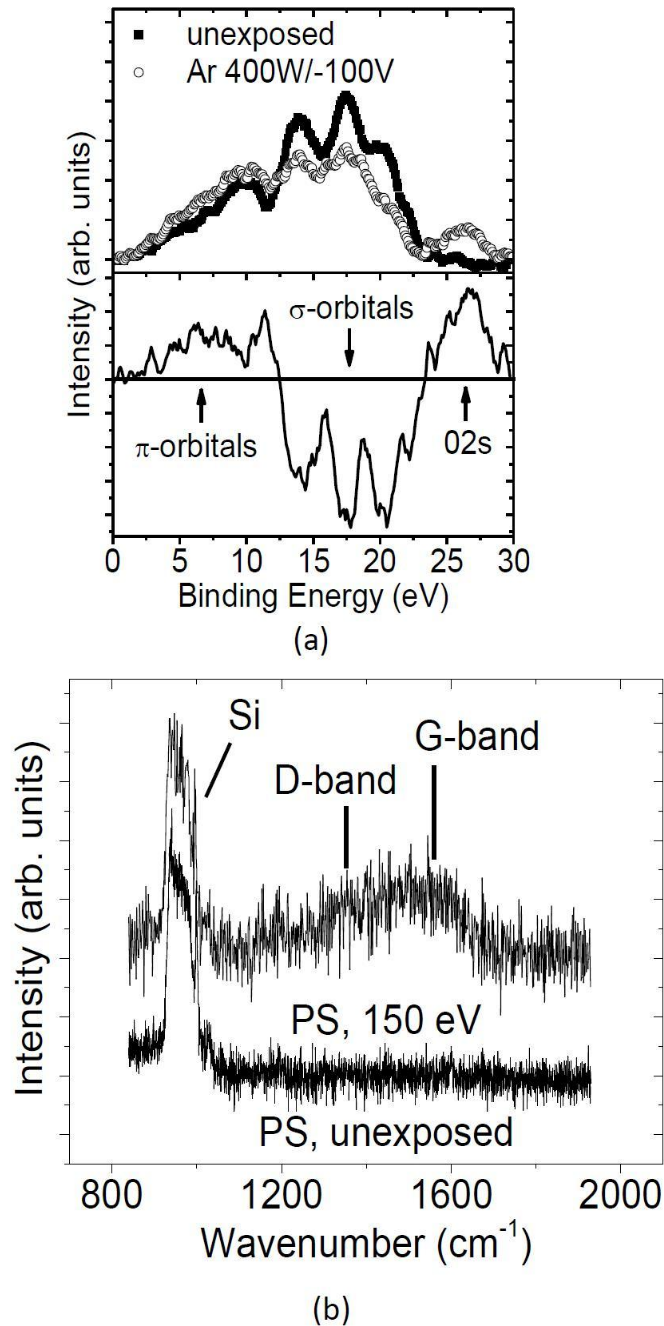

Figure 2.10: (a) The upper plot shows a comparison of valence bands for unexposed and plasma exposed with -100V RF bias PS measured by XPS. The lower plot is the difference between the unexposed and plasma exposed with -100V RF bias PS. (b) At a high RF bias of -150V, a graphitic peak can be seen in the Raman spectra.

Polymer	Damage Layer Thickness (nm)	Density (g/cm3)
PS	1.61±0.051	2.44±0.031
P4MS	1.58±0.037	2.51±0.018
PαMS	1.79±0.051	2.48±0.058

Table 2.1: Estimated steady state damage layer thicknesses and densities for PS, P4MS and PαMS under 100 eV Ar^+ ion bombardment calculated by MD simulations. Data is averaged over the last ~2500 impacts.

Figure 2.11(a) shows the Ψ-Δ trajectory of P4MS exposed to standard Ar conditions with 100 eV ions. Using a damage layer thickness of 1.58 nm, the same refractive index and extinction coefficient as for the damage layer for polystyrene can be used to establish a good fit with the experimental trajectory. This interpretation is valid because P4MS and polystyrene are very similar in properties and behavior, as is shown in literature[2.9,2.27]. Therefore, for P4MS only two layers on top of a Si substrate are required for modeling plasma exposure with high bias as shown in Fig. 2.11(b). The topmost layer is the ion-damaged layer that has properties similar to dehydrogenated amorphous carbon. The bulk layer is similar in properties to unexposed P4MS, and during steady state etch this layer decreases while the top damage layer remains constant.

The same rationale was applied to PαMS exposed to standard Ar conditions with an RF bias to produce 100 eV ions. The damage layer thickness used was 1.79 nm (see from Table I). However, as shown in Fig. 2.12(a), the deviation in trajectory

cannot be fit with just an ion-damage layer on bulk layer. The deviation requires a much larger increase in the optical properties than can be accommodated by the two layer assumption with only the influence of ion bombardment. However, it was shown in Fig. 2.7(a) that with an Ar^+ ion energy that would produce a negligible damage layer, there was still a substantial deviation in the Ψ-Δ trajectory from the bulk PαMS. This was interpreted as densification due to VUV radiation and a 30 nm VUV modified layer was added to the optical model in order to correctly fit the experimental data. The densification of the VUV modified layer is presumed to be much less than the significant densification due to ion bombardment.

Therefore, using a three-layer optical model (shown in Fig. 2.12(b)) consisting of 1.79 nm ion damage layer at the top, 30 nm VUV damage layer below, and unexposed PαMS underneath, the experimental trajectory was fit. The three-layer optical model fit well with the steady state etch regime. Therefore, unlike P4MS, PαMS requires that the contribution of VUV radiation be considered for successful modeling of the ellipsometric data.

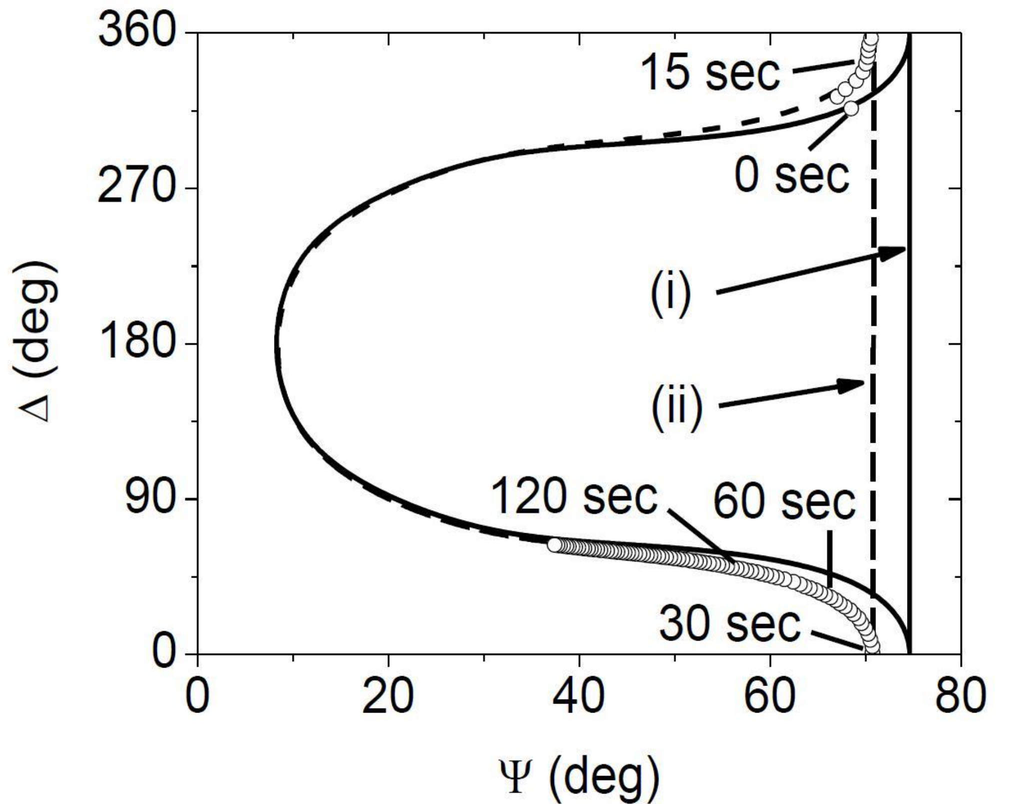

(a)

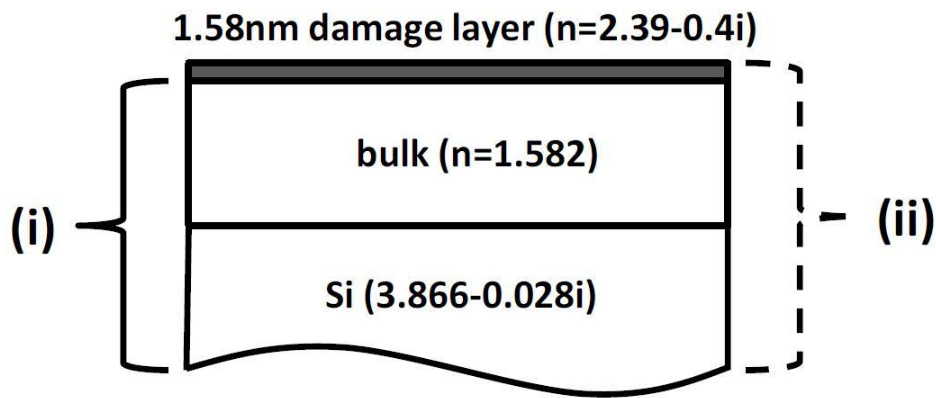

(b)

Figure 2.11: Ψ-Δ plot (a) and optical model (b) for P4MS under -100V self-bias conditions. Simulated trajectories for unmodified P4MS (i) and constant ion-damaged layer on top of P4MS (i) are also shown. Ar discharges were generated using 300W source power, 10 mTorr pressure, 40 sccm gas flow, -100V RF bias, and 5 minute plasma exposure time.

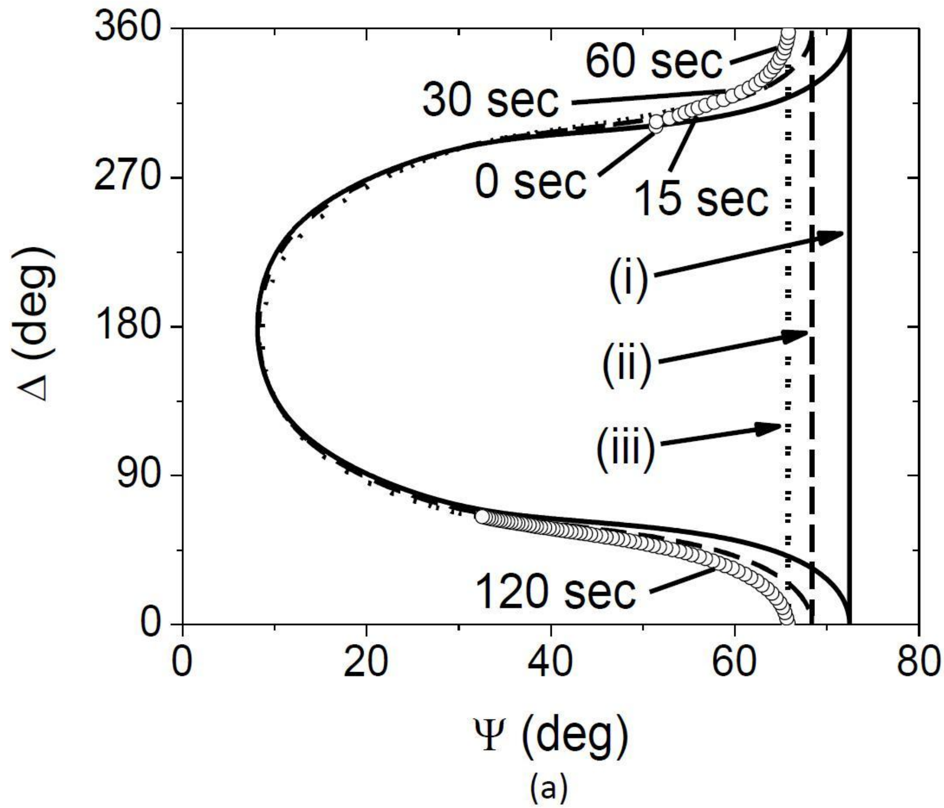

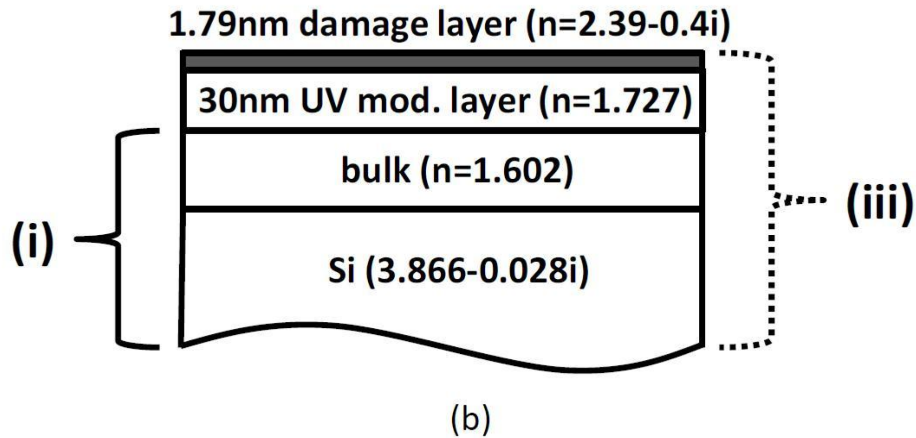

Figure 2.12: Ψ-Δ plot (a) and optical model (b) for PαMS under -100V self-bias conditions. Simulated trajectories for unmodified PαMS (i), constant ion-damaged layer on top of PαMS (ii) and constant ion-damaged layer and UV-damaged layer on top of PαMS (iii) are shown. Ar discharges were generated using 300W source power, 10 mTorr pressure, 40 sccm gas flow, -100V RF bias, and 5 minute plasma exposure time.

The etch rate versus plasma exposure time for P4MS, PαMS, HAdA, and HAMA at -100V bias Ar plasma are shown in Fig. 2.13. All polymers show an initially high etch rate that after 2 to 5 seconds decreases to a much slower etch rate. This high initial etch rate is due to the creation of the ion induced damage layer. Once this damage layer is converted to its steady state properties, it remains constant as the overall thickness continues to decrease. The etch rate of P4MS once steady state is reached is 10 nm/min, PαMS is 28 nm/min, HAdA is 35 nm/min, and HAMA is 30 nm/min. The increased etch rate in PαMS, HAdA, and HAMA may be due to the additional densification that occurs by VUV radiation.

Figure 2.14 shows RMS roughness versus plasma exposure time for P4MS, PαMS, HAdA, and HAMA. These polymer films were etched in the 300 mm ICP under the conditions discussed in Section 2.2. Gradient samples were made via the shutter approach so that RMS roughness versus plasma exposure time could be measured on a single sample for each polymer. For P4MS and PαMS, one gradient sample of each was processed. For HAdA and HAMA, three samples of each were processed and the RMS roughness and plasma exposure time data averaged.

It can be seen that the first 20 seconds shows rapid RMS roughness increase in all polymers and then the increase in roughness afterwards slows. This result is similar to the etch rate versus plasma exposure time plot shown in Fig. 2.13. The introduction of high roughness in Ar exposed polymers is within the very beginning of plasma exposure time as the surface is undergoing densification due to high energy ion bombardment. Specifically, the extent of material loss due to densification seems

to ultimately determine the amount of roughness introduced initially on the polymer surface.

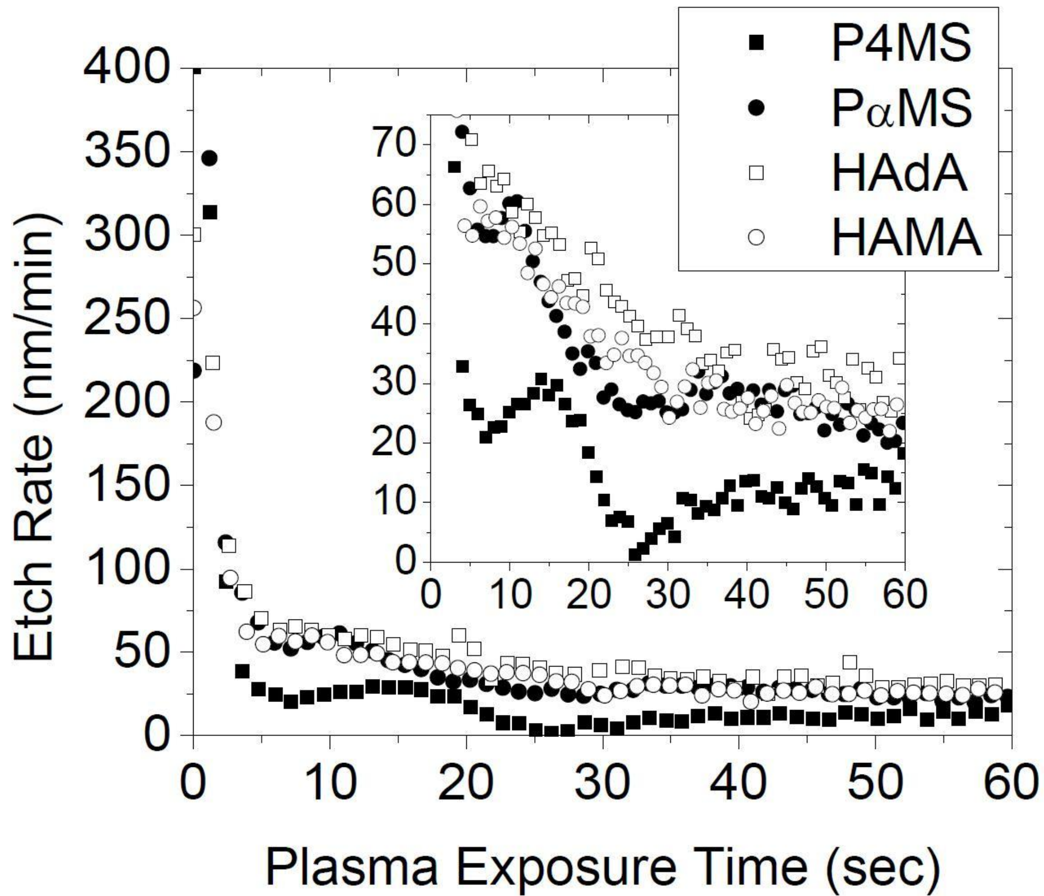

Figure 2.13: Etch rate versus plasma exposure time for P4MS, PαMS, HAdA, and HAdA under Ar -100V self-bias conditions. Inset is a close-up of the reduced etch rate steady-state regime. Ar discharges were generated using 300W source power, 10 mTorr pressure, 40 sccm gas flow, -100V RF bias, and 1 minute plasma exposure time.

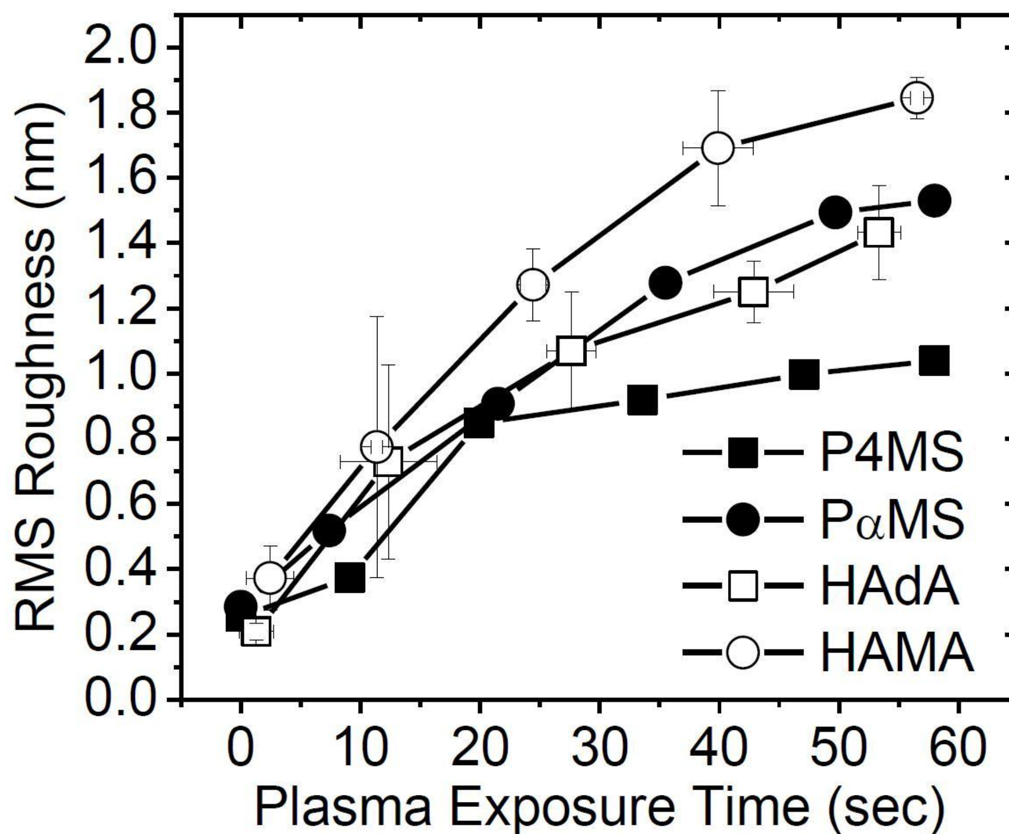

Figure 2.14: RMS roughness of polymers versus plasma exposure time is shown for P4MS, PαMS, HAdA, and HAMA under Ar -100V self-bias conditions. Ar discharges were generated using 400W source power, 10 mTorr pressure, 50 sccm gas flow, -100V RF bias, and 1 minute plasma exposure time. Gradient structures were made to be able to measure RMS roughness versus plasma exposure time.

2.3.6 Discussion: Mechanism of Etching in P4MS, PαMS, and Ester-based Polymers

The difference in etch behavior between P4MS and PαMS looks complex. At low temperature, while the removed thickness is similar, there is a formation of VUV-modified layer in PαMS not present in P4MS. When the temperature is raised, there is a large increase in etch rate in PαMS while the etch rate in P4MS remains constant. The deviation in behavior in PαMS seems to be due to VUV radiation degradation and temperature. However, the large difference in etch behavior is not seen between HAdA and HAMA under the same conditions even though their backbone structures show the same difference.

PαMS, unlike the other polymers, shows very low stability at elevated temperatures under VUV radiation. It is known that there is a low ceiling temperature (66°C) for converting α-methylstyrene monomers into PαMS. Other polymers show much higher ceiling temperature: P4MS is 395°C and PMMA is 198°C.[2.27] The ceiling temperature is the temperature at which the rates of polymerization and depolymerization are equal. Below this temperature, the rate of polymerization is much higher than the rate of depolymerization and the monomers will be converted to almost all polymer. Above the ceiling temperature, the rate of depolymerization is higher and the monomers wil not polymerize. When the polymer is made, the ceiling temperature no longer is an issue and the polymer can be heated past the ceiling temperature without anything occurring. However, under ionizing radiation depolymerization will occur until the monomer concentration increases to equilibrium at that temperature.[2.28] This is most likely the mechanism that occurs for PαMS

during plasma exposure. At high temperature PαMS undergoes VUV photodegradation creating new monomer and depolymerization suddenly occurs causing high thickness loss. At low temperature, the monomers created in PαMS repolymerize at random creating a VUV-modified layer with little thickness loss. A schematic of this mechanism is shown in Fig. 2.15.

P4MS has a very high ceiling temperature and so depolymerization reactions do not occur. Additionally, the polymer is heated past its glass transition temperature, but the etch rate remains the same and roughness is low. Apparently, in the low energy ion case, going above the glass transition temperature does not seem to have much effect on the polymer properties.

The ceiling temperatures of HAdA and HAMA have not been studied, but it is known that addition to the polymer side group does not affect ceiling temperature so much. HAMA should have similar ceiling temperature compared to PMMA. Also, removing the methyl group from the α-carbon, as is done in HAdA, significantly increases the ceiling temperature. Therefore, both polymers have ceiling temperatures above the temperature range for polymer exposure.[2.29,2.30]

The ester-based polymers – HAdA, HAMA, and PMMA show etch behavior dependent on oxygen not ceiling temperature. It is likely that before the temperatures are reached where ceiling temperature should be considered, the effect of ions and VUV to the polymer structure has already depleted the oxygen from the polymer. Once this change occurs, the polymer structure is no longer the same. These results are in agreement with previous work done by Nest, et al.[2.21] They reported that VUV

radiation from Ar plasma resulted in loss of carbon-oxygen bonds in ester-based 193 nm photoresist up to a depth of ~100 nm.

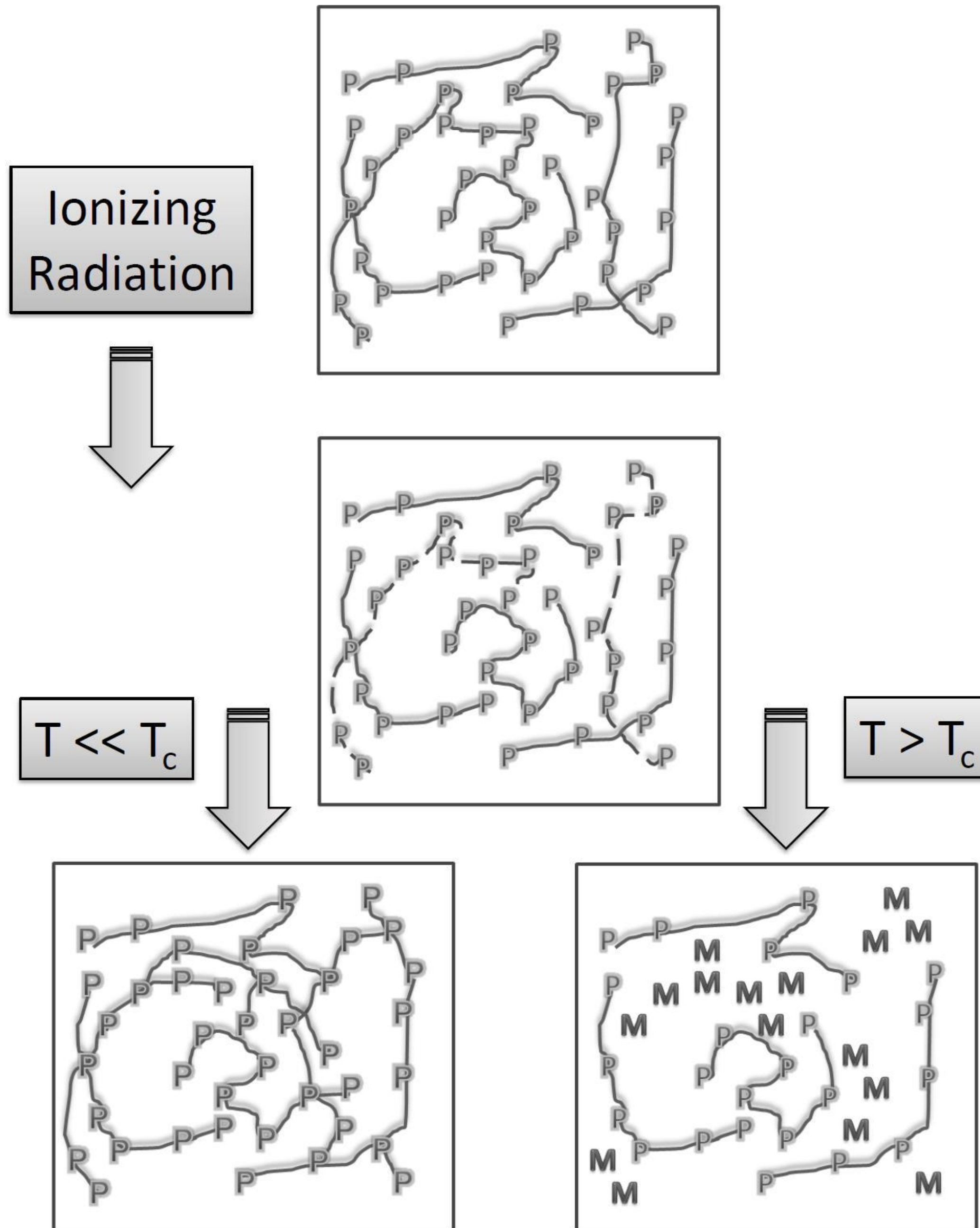

Figure 2.15: Schematic of polymer chains exposed to ionizing radiation for conditions above and below the ceiling temperature.

2.4 Summary and Conclusions

Five model polymers were exposed to Ar plasma conditions and their etch behavior was investigated. P4MS and PαMS, though having similar structure, showed very different etch behavior. P4MS showed no change in physical properties besides a slow etch rate, which remained constant even as the temperature was raised past its glass transition temperature. PαMS showed highly variable behavior depending on conditions. Near room temperature, the etch rate was similar to P4MS but the optical properties showed a densification at the surface. As the temperature increased, the etch rate increased tremendously. It was shown that VUV radiation appears to cause the densification at low temperature and high material loss at high temperature. The exposure temperature relative to the ceiling temperature of PαMS determines what mechanism of degradation occurs. Above the ceiling temperature, PαMS rapidly depolymerizes. Below the ceiling temperature, it repolymerizes randomly creating a denser, crosslinked surface.

The ester-based polymers HAdA, HAMA, and PMMA show etch rates that are determined by oxygen content. HAdA and HAMA have similar oxygen content and their etch rates are very close to one another. PMMA has much higher etch rate, which corresponds to its much greater oxygen content. Etch rates between subsequent exposures show that PMMA degrades with time and can be linked to oxygen depletion. This can be extended to etch behavior of HAdA and HAMA.

It was shown that a dehydrogenated, amorphous carbon layer is created in polymers with thickness determined by the ion penetration depth. Etch yield stabilizes after this layer is formed and afterwards the thickness and properties of the layer remains constant. This can be shown using MD simulation. The experiment can be reproduced in a plasma chamber by setting the self-bias to -100V so that ions impact the surface with energies close to those simulated by MD. The ellipsometric experimental data shows a sudden increase in optical properties in the polymer film. Using the damage layer thickness found in MD simulation, the experimental data is fit by varying the refractive index and extinction coefficient of the damaged surface. The values found that provided the best fit is close to optical properties found in dense amorphous carbon. The corresponding density and hydrogen constant are very close to those simulated by MD.

All the polymers showed the creation of a damage layer using -100V self-bias. P4MS showed very similar etch behavior and damage layer creation as polystyrene. PαMS shows a much greater increase in optical properties than P4MS. Taking into account the modification done to the surface by VUV radiation, the experimental data can be fitted well, implying the importance of VUV radiation for understanding the processing of this material. HAdA and HAMA show much greater etch rates at the beginning, which corresponds with greater thickness removed to establish the damage layer. This is because to make a carbon rich layer, more material needs to be removed.

At high ion energies, it was shown that the relatively high roughness introduction occurs during damage layer creation. The densification that occurs during the initial exposure and creation of the damage layer leads to high roughening.

The polymers that had the greatest amount of removed thickness during densification and damage layer creation showed the highest amount of roughness.

It has been shown that etch and surface roughness behavior in polymers exposed to plasma are dependent on many factors and cannot be described by only physical sputtering. Both ions and VUV radiation must be considered and can have substantial effect on polymer modification. The polymer structure is especially important to consider. Ceiling temperature, polymer oxygen content, and substrate temperature all affect plasma-polymer interactions.

ACKNOWLEDGEMENTS

The authors gratefully acknowledge financial support of this work by the National Science Foundation under award Nanoscale Interdisciplinary Research Team (NIRT) No. CTS-0506988. S. Buckhout-White is thanked for her assistance in Raman spectroscopic analysis. C. Dutton and M. Sweatt are thanked for support in parts of this work. L. Ling, X. Hua, F. Weilnboeck, M. Sumiya, M.-S. Kuo, B. Orf, and D. Lee are thanked for collaboration and helpful discussions of parts of this work.

Chapter 3: Relationship between Nanoscale Roughness and Ion-Damaged Layer in Argon Plasma Exposed Polystyrene Films

To be submitted to Journal of Applied Physics, 2010

R. L. Bruce, F. Weilnboeck, T. Lin, R. J. Phaneuf, G. S. Oehrlein, B. K. Long, C. G. Willson, J. J. Végh, D. Nest and D. B. Graves

ABSTRACT

The uncontrolled development of nanoscale roughness during plasma exposure of polymer surfaces is a major issue in the field of semiconductor processing. In this paper, we investigated the question of a possible relationship between the formation of nanoscale roughening and the simultaneous introduction of a nanometer-thick, densified surface layer that is formed on polymers due to plasma damage. Polystyrene films were exposed to an Ar discharge in an inductively coupled plasma reactor with controllable substrate bias and the properties of the modified surface layer were changed by varying the maximum Ar^+ ion energy. The modified layer thickness, chemical and mechanical properties were obtained using real-time *in situ* ellipsometry, X-ray photoelectron spectroscopy, and modeled using molecular dynamics simulation. The surface roughness after plasma exposure was measured using atomic force microscopy, yielding the equilibrium dominant wavelength λ and amplitude A of surface roughness. The comparison of measured surface roughness wavelength and amplitude data with values of λ and A predicted from elastic buckling theory utilizing the measured properties of the densified surface layer showed excellent agreement

both above and below the glass transition temperature of polystyrene. This agreement strongly supports a buckling mechanism of surface roughness formation.

3.1 Introduction

Polymers are used extensively as pattern transfer masks in semiconductor device fabrication[3.1] and are increasingly being incorporated in the device structures themselves.[3.2] In these applications, they often come into contact with gas discharges, e.g. during plasma etching. Polymers are prone to undesirable nanoscale surface roughening during plasma processing as a result of exposure to energetic ions, reactive species, and VUV radiation that interact and modify the surface.[3.3,3.4,3.5,3.6,3.7] Simultaneously, an ion-damaged surface layer is typically formed. This behavior has been observed in many types of polymers (e.g. poly(methyl methacrylate) (PMMA)[3.8], 193 and 248 nm photoresists[3.5,3.6,3.9,3.10]) and has been described as a thin, highly crosslinked and graphitized layer.[3.4,3.5,3.6,3.11,3.12,3.13,3.14,3.15,3.16] We have previously shown that under energetic Ar^+ ion bombardment during plasma etching, a dense, amorphous carbon-like modified layer is formed at the surface of a wide range of polymers (polystyrene (PS), poly(α-methylstyrene), poly(4-methylstyrene), PMMA, poly(hydroxyadamantyl acrylate) and poly(hydroxyadamantyl methacrylate)) with a thickness of a few nanometers.[3.17] This modified layer forms within the first few seconds of plasma exposure (corresponding to an ion fluence ~ 4×10^{16} cm^{-2}), concurrent with a period of rapid surface roughening.[3.17]

The bilayer structure formed by ion bombardment in the polymer films is reminiscent of similar bilayer structures composed of a compressed, stiff, thin film constrained to a much softer underlayer, such as SiO_2[3.18,3.19] or Si[3.20] on polydimethylsiloxane. Such bilayer structures have been shown to undergo a buckling

instability which leads to wrinkle formation in the micron scale range.[3.21,3.22] Wrinkling has also been observed and characterized in bilayer structures consisting of thin Al films evaporated onto PS films heated above their glass transition temperature (T_g)[3.23,3.24] and µm-thick SiO_2 layers sputtered onto PMMA films at room temperature.[3.25]

There has been little research on examining a possible relationship between plasma-induced modified layer formation and nanoscale surface and line edge roughness[3.26,3.27] that is relevant to polymer resists exposed to pattern transfer plasmas. Such a fundamental connection would have profound consequences on our ability to fabricate three-dimensional nanoscale structures and would assist in establishing new design criteria for reducing the minimum feature size in microelectronics processing. It has been reported that nanoscale roughness became larger when ion damage to a polymer surface was enhanced,[3.28,3.29,3.30] but a quantitative relationship was never established.

In this paper, we report a quantitative relationship between modified layer properties and surface roughness morphology in the well-characterized[3.4,3.11,3.17] and elementary case of polystyrene under Ar plasma exposure that suggests a buckling mechanism for nanoscale roughness formation. In this condition, it has been shown that the formation of an Ar^+ ion-induced modified layer at the surface of PS is the dominant effect, while little modification by other plasma species (e.g. VUV, neutrals) is observed.[3.17,3.31] A schematic of the ion-induced modifications is shown in Fig. 3.1.

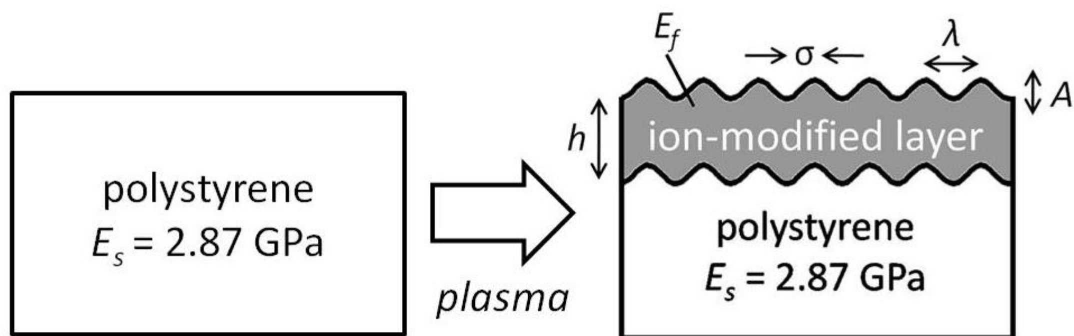

Figure 3.1: A schematic of the highly stressed, modified layer formation and roughening that occurs simultaneously at the surface of a polystyrene film under Ar plasma exposure. Important materials and morphological properties are also shown.

3.2 Experimental Details

Polystyrene films (2.5 × 2.5 cm^2, ~400 nm thick, glass transition temperature (T_g) ~ 100 °C[3.32]) were processed under Ar plasma conditions at a range of ion energies (50-150 eV), which formed modified layers of different thicknesses (1-2 nm). Samples were plasma-exposed in an inductively coupled plasma (ICP) reactor, described previously.[3.17] The following process conditions were employed: 300W source power using a 13.56 MHz RF power supply, 0-150W bias power using a 3.7 MHz RF power supply, an operating pressure of 10 mTorr, and Ar gas flow rate of 40 sccm. The bias power was set to establish a constant substrate bias and comparable Ar^+ ion energy bombardment on the PS film. The maximum ion energies were measured by adding the plasma potential (~ -25 V) to the substrate bias voltage (-25 V to -125 V). PS films were bonded to a chilled substrate (~10°C) by thermal grease and plasma-exposed for 60 seconds. During the plasma process, the PS films stayed very close to room temperature (~40 °C). This was monitored by real-time *in situ*

ellipsometry, utilizing the fact that the complex index of refraction (*n-ik*) of PS changes with temperature.[3.32] When the plasma was turned off, we did not observe any change in *n-ik* that would correspond to cooling down of the PS films with time.

X-ray photoelectron spectroscopy (XPS) analysis was performed in a Vacuum Generators ESCA Mk II surface analysis chamber using a nonmonochromatized Mg Kα X-ray source (1253.6 eV). Samples were transferred in air immediately after processing. All spectra were obtained at normal emission angle and in constant analyzer energy mode at 20 eV pass energy. The analyzer resolution was approximately 0.2 eV and the resolution of the spectra was limited by the linewidth of the X-ray source, approximately 1 eV.

Molecular dynamics (MD) simulations were performed using a Tersoff-Brenner style REBO potential to examine bombardment of a model PS cell by Ar^+ ions. From the MD simulations, the modified layer thickness, *h*, was obtained by measuring the depth of the modified region with constant H:C ratio after ~8000 impacts. The method of MD simulation and *h* measurement has been explained in detail in previous publications.[3.4,3.11,3.17]

The complex index of refraction (*n-ik*) of the modified layer formed on PS samples was measured *in situ* by a single wavelength (HeNe laser) ellipsometer. The ellipsometer is an automated rotating compensator ellipsometer working in the polarizer-compensator-sample-analyzer (PCSA) configuration and with an angle of incidence of 71.3°. The values Ψ and Δ were measured and were related to fundamental physical properties of the polymer film by using an optical model and solving the Fresnel reflection coefficients for the physical property values.[3.33] The

values of Ψ and Δ are interpreted using a three-layer optical model (modified layer/PS/Si substrate) where the complex index of refraction (*n-ik*) of Si was fixed at 3.866-0.28i[3.33] and PS was fixed at 1.600-0.00i.[3.32]

Atomic force microscopy (AFM) measurements were performed on PS samples after plasma exposure ($2 \times 2\ \mu m^2$ scan size) and after heating plasma-exposed samples above their T_g ($50 \times 50\ \mu m^2$ scan size). The dominant wavelength of the surface roughness was determined by measuring the peak value in the Fast-Fourier Transform (FFT) spectrum of the AFM images and the dominant amplitude of the surface roughness was determined by measuring the RMS roughness.

3.3 Results and Discussion

From buckling theory, in the small deformation limit, it is known that the wavelength and amplitude of wrinkles formed by buckling are linearly proportional to the thickness of the stiff overlayer.[3.18] Therefore, the measured values of modified layer thickness, h, and deduced elastic modulus of the modified layer, E_f, (see discussion below) at each maximum ion energy condition were used to calculate the wrinkle wavelength and amplitude, which were then compared with the dominant wavelength and amplitude of the plasma-induced surface roughness measured by atomic force microscopy (AFM).

The ion-modified layer thickness, h, was obtained by both XPS analysis and MD simulation. For the XPS analysis, it was assumed that the modified layer was homogeneous in chemical composition and density and that the aromatic ring

structure of PS was lost inside the modified layer due to ion damage.[3.34] Therefore, h can be calculated by measuring the intensity of the π-π* shake-up peak at 291.3 eV, which is unique to the aromatic ring structure of PS,[3.35] for damaged and undamaged PS. Here we utilize the fact that the π-π* shake-up peak intensity will decrease as the modified layer is formed and h is found using the equation[3.36]

$$h = \lambda_{IMFP} \ln \frac{I_0}{I} . \qquad (3.1)$$

Here λ_{IMFP} is the inelastic mean free path, and I_0 and I are the unattenuated and attenuated π-π* shake-up peak intensities, respectively. The two methods of extracting h were required because for accurate XPS analysis it is necessary that the density of the modified layer be known for proper assignment of λ_{IMFP}.[3.37,3.38] Assuming that the density remained constant and that λ_{IMFP} was 2.8 nm,[3.38] we compare h determined by XPS with the values found by MD in Fig. 3.2. The figure shows close agreement for both approaches and for both methods h increased with maximum ion energy.

The complex index of refraction, *n-ik*, of the modified layer was obtained from the *in situ* ellipsometry measurements made during plasma exposure. The modified layer thickness h obtained by MD simulations was used in the three-layer optical model to simulate values of Ψ and Δ. The simulated values were then fitted with experimental values of Ψ and Δ by varying the PS thickness and modified layer complex index of refraction, *n-ik*. This analysis has been explained in detail for the case of 100 eV Ar^+ bombardment of PS in a previous publication.[3.3] Since the modified layer is treated as an amorphous carbon layer[3.4,3.6,3.13,3.17] for which the relationship between *n-ik* to density is known,[3.39] the elastic modulus of the modified

layer, E_f, can also be established.[3.40] Values of h, n-ik, density, and E_f are shown in Table 3.1.

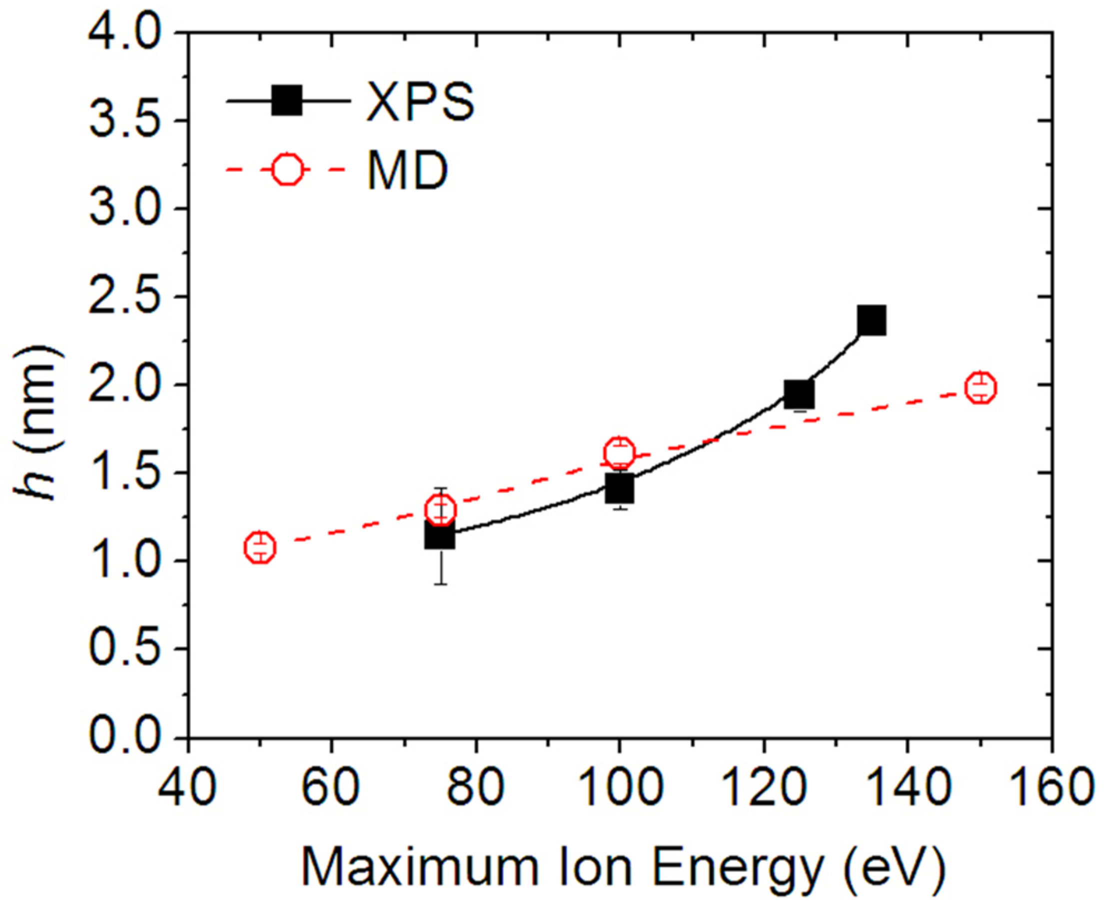

Figure 3.2: Dependence of ion-damaged layer thickness, h, on the maximum ion energy determined by XPS analysis and MD simulation.

Maximum Ion Energy (eV)	*h* (nm)	*n-ik*	*Density* (g/cm^3)	E_f (GPa)	σ (GPa)	σ_c (GPa)
50	1.08±0.03	(2.32±0.01)-(0.21±0.01)*i*	2.36±0.03	271.3±14.1	-15.50	-7.57±0.13
75	1.29±0.03	(2.38±0.01)-(0.36±0.02)*i*	2.61±0.02	406.6±11.3	-16.50	-8.66±0.08
100	1.61±0.05	(2.39±0.01)-(0.42±0.02)*i*	2.68±0.03	446.5±14.7	-16.75	-8.94±0.10
150	1.98±0.03	(2.42±0.01)-(0.56±0.05)*i*	2.84±0.05	549.3±34.0	-17.30	-9.57±0.20

Table 3.1: Shown are modified layer properties for the different maximum ion energy conditions. *h* and *n-ik* were determined by molecular dynamics simulation and ellipsometry, respectively. Density, E_f and σ were obtained from amorphous carbon property relationships in Ref. 3.39, 3.40, and 3.41, respectively. σ_c was calculated from Equation 3.2.

Overall, the modified layer densities obtained by ellipsometry are similar to densities measured for ion-enhanced amorphous carbon films grown at equivalent ion energies.[3.41,3.42] The high densities are achieved through a process called "atomic peening".[3.43] Here, bombarding ions cause atoms at the surface to be displaced, thereby creating a region of higher density and compressive stress. While carbon atoms become more densely packed, the same mechanism depletes hydrogen from the surface, since displaced hydrogen atoms recombine to form H_2, which is then released.[3.39] Ar incorporation was not considered since by XPS compositional analysis the atomic percent Ar was found to be less than 0.5% in all plasma-exposed PS samples. The relationship between amorphous carbon film density and the

compressive stress intrinsic to the film produced by this mechanism, σ, has been reported in a number of publications.[3.42,3.44] Using the experimental relationship from Schwan, et al.,[3.42] σ for the modified layer film densities are shown in Table 3.1.

For a thin, stiff film on a much thicker, softer film, a compressive stress applied in-plane to the stiff film above a critical value, σ_c, will create a buckling instability causing the bilayer structure to wrinkle. If both layers are treated as elastic, σ_c is

$$\sigma_c = -\frac{E_f}{4\left(1-\nu_f^2\right)}\left(\frac{3E_s\left(1-\nu_f^2\right)}{E_f\left(1-\nu_s^2\right)}\right)^{\frac{2}{3}}, \qquad (3.2)$$

where E and v is the elastic modulus and Poisson ratio, while subscripts f and s denote the stiff overlayer and soft underlayer, respectively.[3.20] For all modified layers, the Poisson ratio is 0.30.[3.45] At 40°C, E_s and v_s are 2.87 GPa and 0.33, respectively.[3.46] The calculated values for σ_c are shown in Table 3.1. For each case σ is larger than σ_c indicating that the stress generated by modified layer formation is sufficient to drive the buckling transition.

An elastic bilayer structure that undergoes a buckling instability will wrinkle at an equilibrium wavelength, λ, and amplitude, A, that minimizes the elastic energy of both films. In the small deformation limit, the equilibrium wavelength of buckling[3.20] is

$$\lambda = 2\pi h\left(\frac{E_f\left(1-\nu_s^2\right)}{3E_s\left(1-\nu_f^2\right)}\right)^{\frac{1}{3}}, \qquad (3.3)$$

and, in that same limit, the amplitude of the buckling instability[3.20] is

$$A = h\left(\frac{\sigma}{\sigma_c} - 1\right)^{\frac{1}{2}}. \qquad (3.4)$$

The morphological properties of the bilayer structure are schematically shown in Fig. 3.1.

In Fig. 3.3(a), 500 nm × 500 nm AFM images of PS after plasma exposure are shown. Figure 3.3(b) displays a comparison of calculated values of λ using equation 3.3 with experimental values obtained by determining the peak values in the Fast-Fourier Transform (FFT) spectra of the AFM images shown in Fig. 3.3(a). The agreement between calculated and experimentally measured values of λ can be considered excellent. The comparison of the calculated and experimental values of A is shown in Fig. 3.3(c). The experimental values were obtained by measuring the RMS roughness from the AFM images and subtracting the initial RMS roughness of the unexposed polymer film (0.3 nm). The figure shows that the experimental values of A are comparable to but vary more slowly with ion energy than the calculated values. It is possible that the agreement between experimental and calculated values of A can be improved by direct measurement of the compressive stress, σ, of the modified layer.

The contribution of plasma etching to the RMS roughness was not considered since the thickness removed was the same (~20 nm) for all conditions. In addition, the roughness increase was very small (less than 1 nm/min) as compared to the high roughening rate that takes place during modified layer formation.

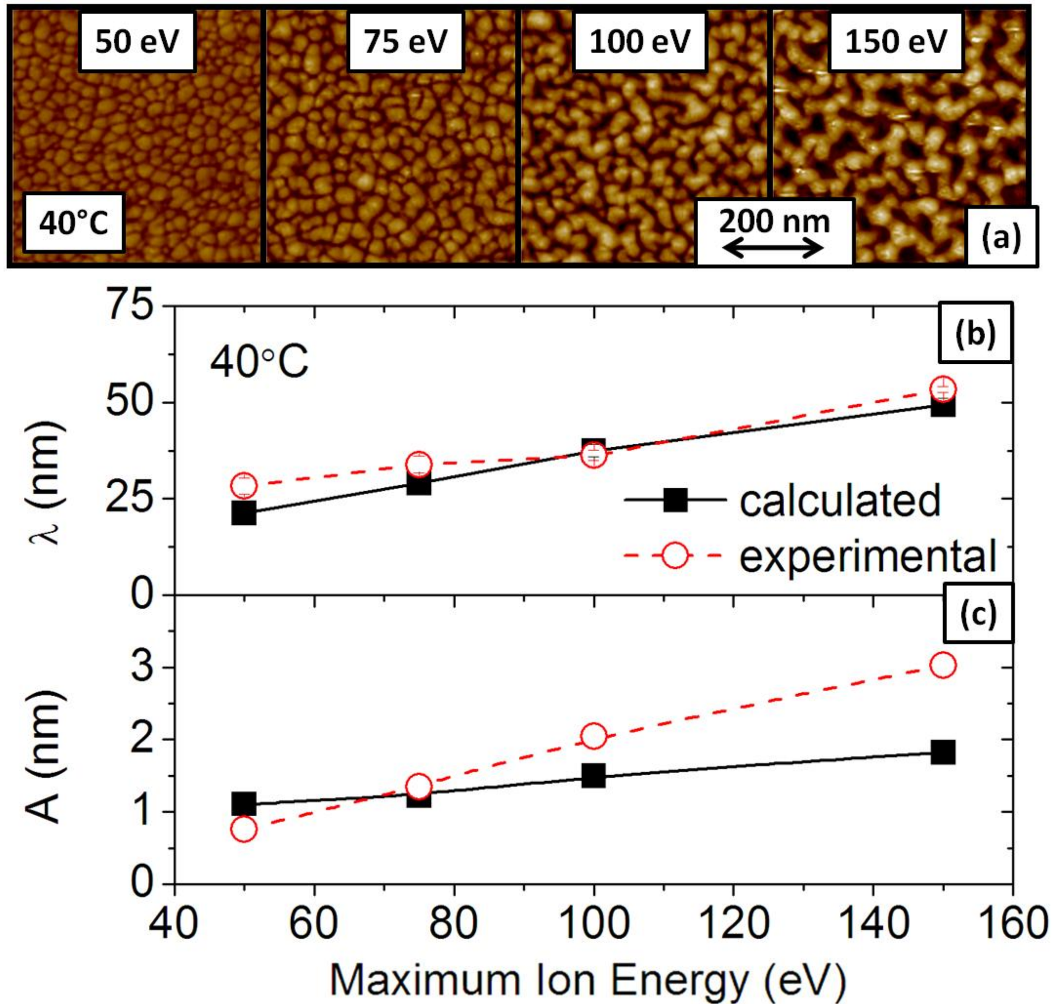

Figure 3.3: (a) 2 × 2 μm AFM images showing surface roughness in PS after ion bombardment at varying maximum ion energies. Also shown are calculated and experimental values of λ (b) and A (c) versus maximum ion energy of the nanoscale roughness processed at 40°C.

Further support that the plasma-induced modified layer was under compression was obtained by heating the plasma-processed samples above the glass transition temperature T_g of PS on a hot plate. Samples were heated for 15 min at 170 °C. By heating above T_g of PS, the underlayer undergoes a several orders of magnitude reduction in E_s. This method has been used in the past to produce micron-

sized wrinkles in PS with thin metal films deposited at the surface.[3.23,3.24] At 170°C, E_s and ν_s are 1×10^{-4} GPa and 0.5.[3.47] It is unknown if after plasma etching the modified layer remains under compressive stress or if stress relaxation causes the bilayer structure to be permanently deformed into its wrinkle morphology. Using equation 3.3 and assuming that σ and the properties of the modified layer stayed the same, we would expect that at 170°C λ should increase by ~30×.

Figure 3.4(a) shows 12.5 × 12.5 μm AFM images of PS after plasma exposure and after heating to 170°C. By visual inspection, the wavelength of roughness is much larger than before heating. The wrinkles are not merely larger in scale, but dramatically different in shape, i.e. anisotropic and folded rather than isotropic and compact. Figures 3.4(b) and 3.4(c) show comparisons of the calculated and experimental values of λ and A, respectively. For the 170°C case, the expected ~30× increase in λ was confirmed and the agreement between measured and calculated values of λ and A can be considered satisfactory.

The observation that λ and A obtained from the measured surface roughness were of the same order of magnitude as values derived from elastic buckling theory in the small displacement limit both below and above the glass transition temperature T_g of PS suggests a mechanical stress origin of plasma-induced surface roughness. For the 170°C case, the expected ~30× increase in λ relative the 40°C case was confirmed. Additionally, the same compressive stress σ of the modified layer was sufficient to explain the change in A from the 40°C case.

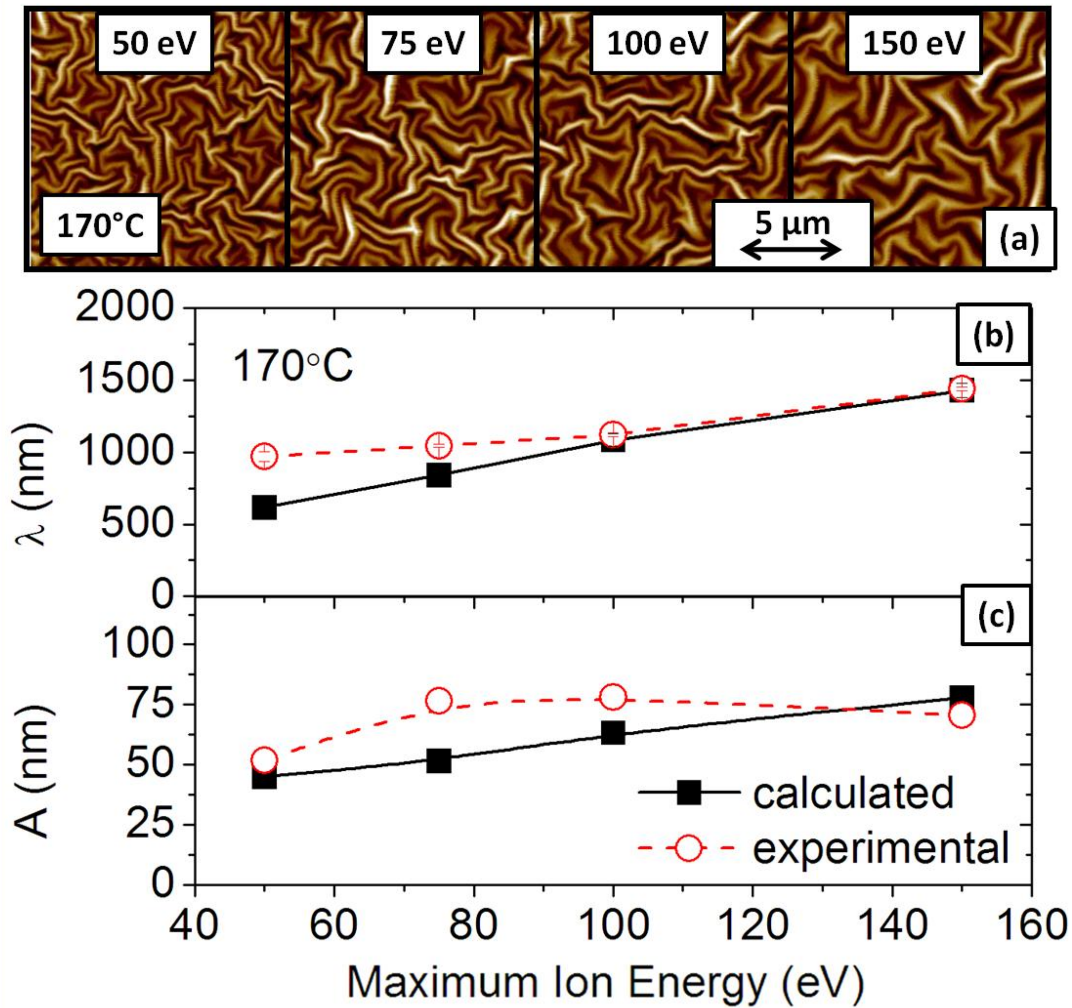

Figure 3.4: (a) 50 × 50 μm AFM images showing surface roughness in PS after the samples processed under the same conditions are heating to 170°C. Also shown are calculated and experimental values of λ (b) and A (c) versus maximum ion energy of plasma processed samples after heating to 170°C.

3.4 Conclusions

In conclusion, the agreement found between calculated values of λ and A based on modified layer characteristics in conjunction with elastic buckling theory

and λ and A values obtained by analysis of experimental roughness morphology is compelling. This agreement strongly suggests that buckling caused by the ion-induced formation of a highly compressed, modified surface layer is the origin of the nanoscale roughness that develops during plasma etching. Understanding how a polymer will roughen based on polymer structure following a buckling mechanics interpretation will require further study. UV-sensitive polymers show increased post-plasma etch surface roughness compared to UV-insensitive polymers such as PS.[3.5,3.9] From wrinkling theory, a reduced underlayer elastic modulus would increase the magnitude of wrinkling that occurs during formation of the highly stressed, modified layer by ions. We suspect that the observed plasma-generated UV damage[3.5,3.48] in UV-sensitive polymers (i.e. 193 nm PR[3.5], poly(α-methylstyrene)[3.17]) reduces their underlayer modulus and is responsible for the enhanced surface roughness compared to UV-insensitive polymers (i.e. 248 nm PR[3.5], PS) observed under simultaneous ion bombardment and UV exposure. Characterizing the extent of plasma modification (ions, UV, radicals) in different polymers and determining the effect on the mechanics of buckling will help shed light on this important field of research.

Acknowledgements

The authors gratefully acknowledge financial support by the National Science Foundation under awards CTS-0506988 and DMR-0705953.

Chapter 4: On the Absence of Post-Plasma Etch Surface and Line Edge Roughness in Vinylpyridine Resists

To be submitted to J. Vac. Sci. Technol. B, 2010

R. L. Bruce, F. Weilnboeck, T. Lin, R. J. Phaneuf, G. S. Oehrlein, B. K. Long, C. G. Willson and A. Alizadeh

ABSTRACT

We show that poly(4-vinylpyridine) (P4VP) resist eliminates plasma-induced surface roughening for dry etch process conditions (100% Ar, 90% Ar/C_4F_8) that produce significant roughness in a wide variety of other polymers. In hot-embossed patterned structures, P4VP also shows no sidewall striations and line edge roughness (LER) after plasma etching, in contrast to other polymers investigated in this work. The mechanism underlying the retention of smooth surfaces for P4VP was investigated based on the observation that plasma-induced surface roughness in polystyrene (PS) has been linked to wrinkling caused by the formation of a thin, dense, ion-damaged layer. By X-ray photoelectron spectroscopy and *in situ* ellipsometry analysis, we studied two possible mechanisms that would suppress wrinkling in plasma-exposed P4VP: softening of the ion-damaged layer by nitrogen addition and stiffening of the polymer underlayer by VUV modification. While we report that the elastic modulus of the ion-damaged layer is reduced in Ar plasma-exposed PS when nitrogen is added to the gas discharge, the ion-damaged layer of P4VP showed no significant change relative to PS. However, by examining only the VUV radiation effect of the Ar discharge on P4VP, evidence of VUV crosslinking

was observed, which would likely suppress wrinkling in P4VP when an ion-damaged layer is formed during normal plasma exposure.

4.1 Introduction

Reducing formation of line edge roughness (LER) during pattern transfer by plasma etching is becoming increasingly important as device critical dimensions (CD) continue to shrink.[4.1,4.2] A major contributor to high LER is the plasma etch pattern transfer step, in which a pattern in a polymer resist is transferred into a dielectric layer used as a hard mask.[4.3,4.4] The standard gas chemistry used for dielectric etch is a mixture of Ar and a polymerizing fluorocarbon gas (e.g. 90% Ar/C_4F_8)[4.5], enabling high selectivity of etching the dielectric relative to the resist mask.

Under Ar rich, high substrate bias conditions, the polymer surface is subjected to bombardment by high energy Ar^+ ions. This ion bombardment dehydrogenates the surface and establishes a carbon-rich ion-damaged layer several nanometers thick.[4.6] In a previous publication,[4.7] we linked the onset of plasma-induced surface roughening to the creation of the ion-damaged layer at the beginning of plasma exposure. We have established in a separate publication[4.8] that the ion-damaged layer induces a compressive stress on the polymer that causes a buckling instability and leads to nanoscale wrinkling of the surface.

Polymer structure can have a major impact on LER, as was found during the transition from 248 nm to 193 nm UV lithography. The use of 193 nm photoresists (PR) led to a major increase in surface and line edge roughness.[4.9] Choice of polymer structure for resists has been restricted due to requirements of transparency to the UV exposure wavelength and ability to undergo acid-catalyzed reactions to increase solubility after photoexposure.[4.10] The advent of alternative lithographic techniques[4.11], e.g. imprint lithography, EUV and self-assembly, provides the opportunity to

optimize polymer structure and composition so that surface and line edge roughness is minimized during the plasma pattern transfer steps.

The observation of strongly reduced surface roughness[4.12,4.13] in grown CN_x films suggests the use of N-containing polymers as resists or N_2 addition to pattern transfer plasmas as a novel approach to reduce surface and line edge roughness for plasma etched resist surfaces and structures. In this manuscript, we observed remarkably smooth surfaces and sidewalls in poly(4-vinylpyridine) (P4VP) after plasma etch, while significant roughening was found in two other polymers representative of conventional PR polymers for the same process conditions.

Currently, the mechanism behind P4VP smoothness after plasma etch is not known. We examine the effects of nitrogen addition to the ion-damaged layer and vacuum ultraviolet (VUV) bulk modification as possible causes of the lack of surface roughness in P4VP.

4.2 Experimental Setup

The primary polymers (inset, Fig. 4.1(a)) studied were polystyrene (PS), poly(α-methylstyrene) (PαMS) and P4VP. We also tested poly(4-methylstyrene) (P4MS), poly(hydroxyadamantyl acrylate) (HAdA), poly(hydroxyadamantyl methacrylate) (HAMA), and 248 nm and 193 nm photoresists.[4.9] All polymers were spin-coated onto Si wafers and the average thickness of the polymer films was 400 nm.

Patterned structures of PS, PαMS and P4VP were fabricated by hot embossing.[4.14] The pattern is an array of identical columns with a center-to-center

distance of 1800 nm. The columns are tapered cylinders each with 500 nm height, 700 nm top CD and 1000 nm bottom CD.

Polymers were processed using Ar, 2.5% N_2/Ar and 5% N_2/Ar plasma conditions at a range of maximum ion energies (75-135 eV). Samples were plasma-exposed in an inductively coupled plasma (ICP) reactor, described previously.[4.7] The following process conditions were employed: 300W source power using a 13.56 MHz RF power supply, 0-150W bias power using a 3.7 MHz RF power supply, an operating pressure of 10 mTorr, and combined gas flow rate of 40 sccm. The bias power was set to establish a constant substrate bias and comparable ion energy bombardment on the polymer film. The maximum ion energies were measured by adding the plasma potential (~ -25 V) to the substrate bias voltage (-25 V to -125 V).

For 90% Ar/C_4F_8 gas discharges, polymers were processed in another ICP reactor, described previously,[4.9] with the following process conditions: 800W source power using a 13.56 MHz RF power supply, fixed -100V substrate bias, an operating pressure of 10 mTorr, and combined gas flow rate of 50 sccm. For all conditions, polymer films were bonded to a chilled substrate (~10°C) by thermal grease and plasma-exposed for 60 seconds.

X-ray photoelectron spectroscopy (XPS) analysis was performed in a Vacuum Generators ESCA Mk II surface analysis chamber using a nonmonochromatized Mg Kα X-ray source (1253.6 eV). Samples were transferred in air immediately after processing. All spectra were obtained at normal emission angle and in constant analyzer energy mode at 20 eV pass energy. The analyzer resolution was

approximately 0.2 eV and the resolution of the spectra was limited by the linewidth of the X-ray source, approximately 1 eV.

The complex index of refraction (*n-ik*) of the modified layer formed on PS samples was measured *in situ* by a single wavelength (HeNe laser) ellipsometer. The ellipsometer is an automated rotating compensator ellipsometer working in the polarizer-compensator-sample-analyzer (PCSA) configuration and with an angle of incidence of 71.3°. The values Ψ and Δ were measured and were related to fundamental physical properties of the polymer film by using an optical model and solving the Fresnel reflection coefficients for the physical property values.[4.15] The values of Ψ and Δ are interpreted using a three-layer optical model (modified layer/polymer/Si substrate) where the complex index of refraction (*n* and *k*) of Si was fixed at 3.866-0.28i[4.15] and PS and P4VP were fixed at 1.600-0.00i[4.16] and 1.581-0.00i,[4.17] respectively.

Atomic force microscopy (AFM) measurements were performed on polymer samples after plasma exposure (2 × 2 μm^2 scan size) and after heating plasma-exposed samples 10 °C above their T_g (50 × 50 μm^2 scan size). For PS, samples were heated to 110 °C and for P4VP, samples were heated to 155 °C. The dominant wavelength of the surface roughness was determined by measuring the peak value in the Fast-Fourier Transform (FFT) spectrum of the AFM images and the buckle amplitude was determined by measuring the RMS roughness. Cross-sectional images of patterned films were acquired using a LEO 1550 SEM.

4.3 Results and Discussion

4.3.1 Comparison of Surface and Line Edge Roughness in PS, PαMS, and P4VP

Fig. 4.1(a) shows the AFM scanned images and Fig. 4.1(b) the corresponding RMS roughness of PS, PαMS and P4VP films processed under 100% Ar and 90% Ar/C_4F_8 gas discharge conditions at -100V substrate bias. The RMS roughness of PS and PαMS films was considerably lower after etching in 100% Ar conditions compared to after etching in 90% Ar/C_4F_8 conditions. PαMS undergoes enhanced degradation compared to PS,[4.7] which results in higher RMS roughness values. P4VP showed no significant change in surface roughness in either condition.

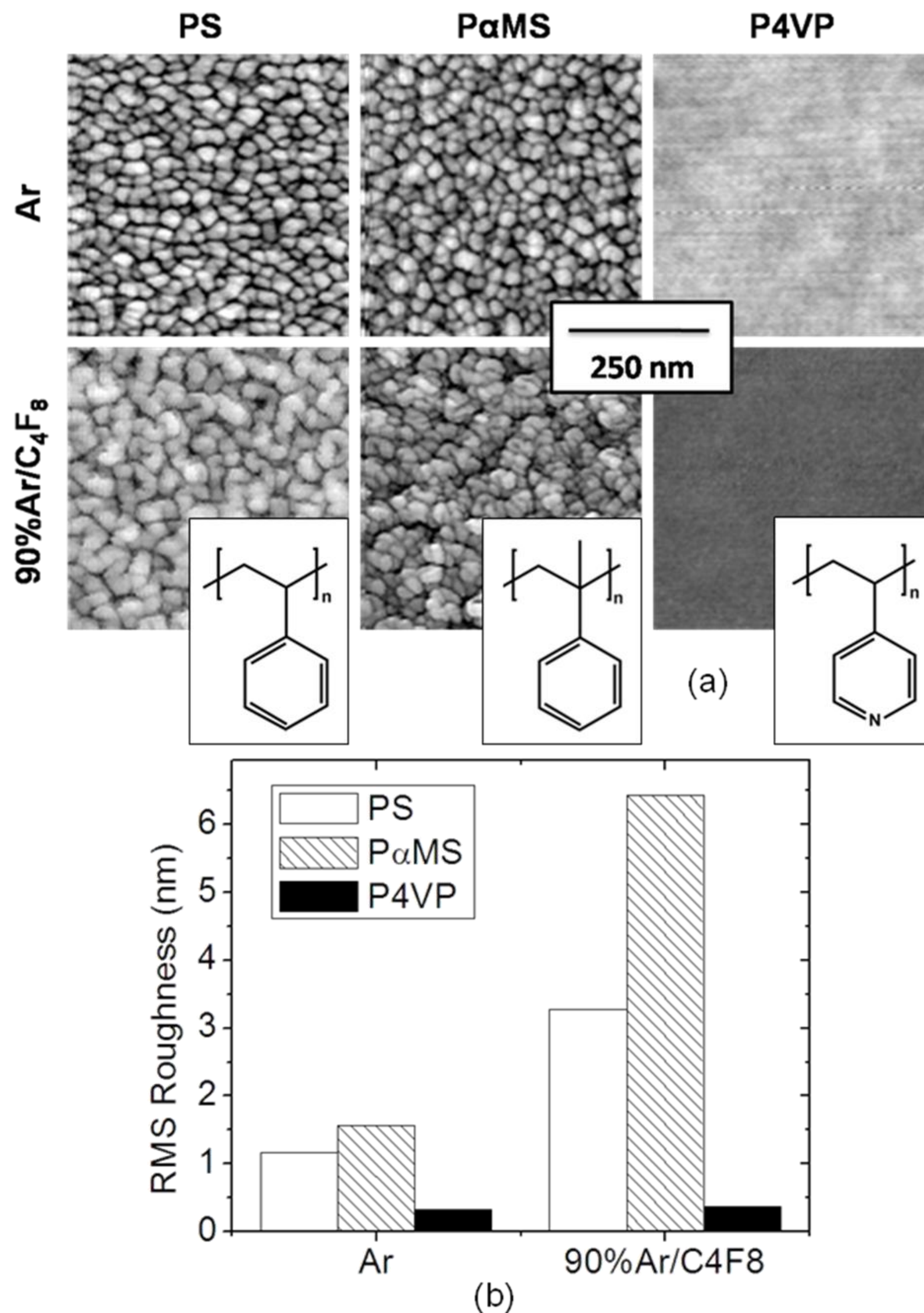

Figure 4.1: (a) AFM images with corresponding polymer structures as inset and (b) comparison of RMS roughness for PS, PαMS and P4VP after 100%Ar and 90% Ar/C_4F_8 plasma exposures. Samples were etched for 60 seconds.

The smooth surface of P4VP after processing made it unique among many polymers tested. The RMS roughness values of a wide range of polymers under Ar and 90% Ar/C_4F_8 conditions are shown in Fig. 4.2 and only P4VP remained smooth after processing.

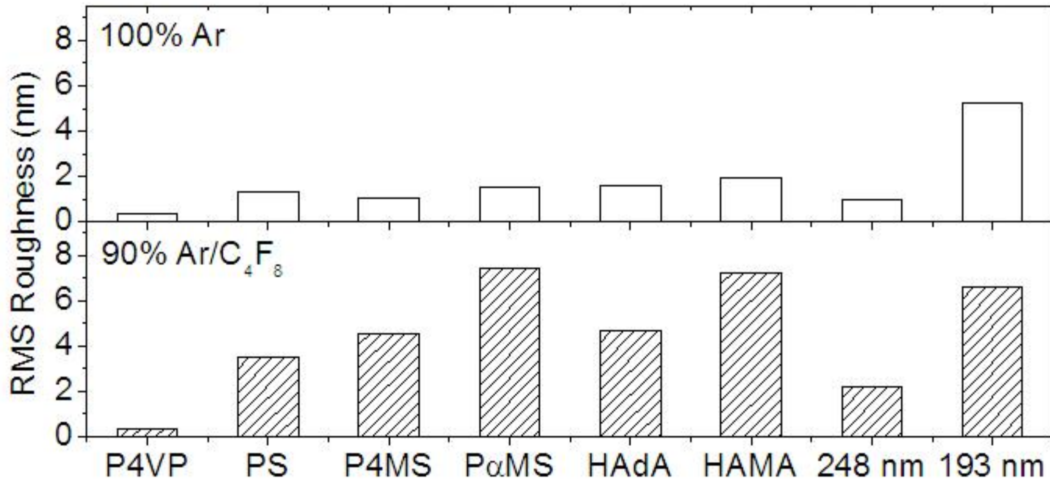

Figure 4.2: RMS roughness of selected polymers (P4VP, PS, P4MS, PαMS, HAdA, HAHA, 248 nm PR and 193 nm PR) after Ar and 90% Ar/C_4F_8 plasma exposures. Samples were etched for 60 seconds.

We also examined the impact of 100% Ar and 90% Ar/C_4F_8 plasma exposures on patterned structures of PS, PαMS and P4VP. SEM images of structures after 100% Ar and 90% Ar/C_4F_8 plasma exposures are shown in Figs. 4.3(a) and (b), respectively.

In Fig. 4.3(a), PS and PαMS showed surface roughening after 100% Ar exposure at 100 eV with PαMS showing the greatest roughness. Similar to the RMS roughness results, P4VP showed no visible roughness after processing. In PS and PαMS, longitudinal striations were also observed along the sidewalls. It is known that striation development along sidewalls leads to a significant increase in LER.[4.3] For

both polymers, the striations ran alongside the cylinders from the top to midway along the cylinder. This suggested that the striations were created by surface roughness at the top and transferred along the sidewall during plasma etch, which is supported by observations reported by Hua, *et al*.[4.18] Furthermore, the absence of striations in the P4VP cylinders shows that elimination of surface roughness at the top leads directly to elimination of LER along the sidewalls. A change in the profile shape of the cylinders was also observed after 100% Ar plasma etch. The top critical dimension (CD) was reduced more than the bottom CD, which resulted in a horn-like shape. All polymers showed this characteristic profile change, suggesting similar material removal and, therefore, etch behavior in all polymers.

Similar results were found for 90% Ar/C_4F_8 processing, and are shown in Fig. 4.3(b). PαMS had greater roughness than PS, while P4VP showed no roughness after plasma exposure. In PS and PαMS, the visible roughness was greater after 90% Ar/C_4F_8 condition as compared to 100% Ar, the sidewall striations were coarser and extended from the top of the cylinder all the way to the bottom. In addition, the profile shapes did not change as much as for the 100% Ar condition, remaining tapered cylinders.

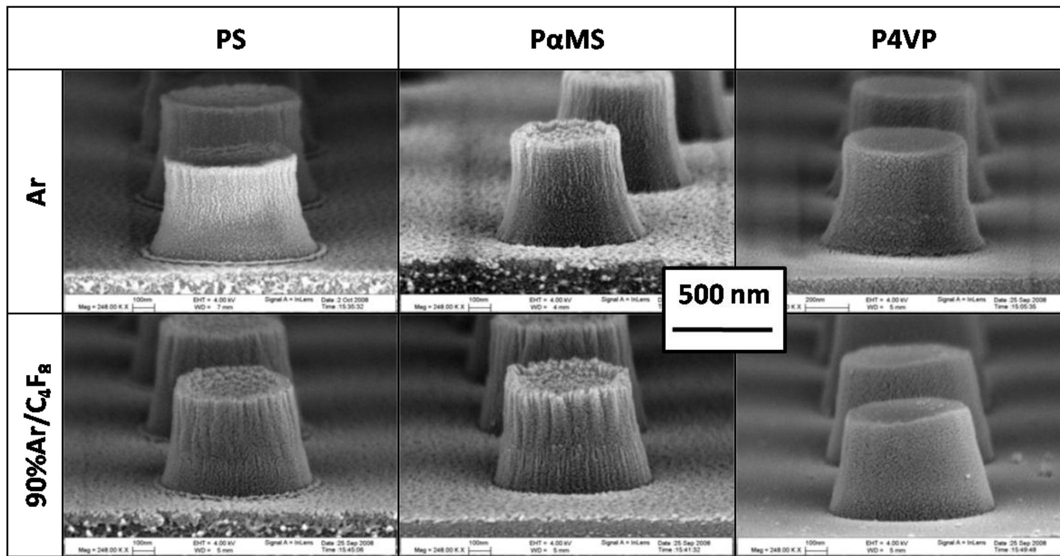

Figure 4.3: SEM images of hot embossed patterned samples of PS, PαMS and P4VP are shown after (a) 100% Ar and (b) 90% Ar/C_4F_8 plasma exposure.

In Fig. 4.4(a), we compare the etch behavior in an Ar discharge at -100V substrate bias for PS, PαMS and P4VP. PαMS exhibited the highest removed thickness (45.7±1.2 nm) after 60 seconds while PS and P4VP showed similar, lower removed thicknesses (27.5±2.1 nm and 28.1±0.6 nm, respectively). The higher removed thickness of PαMS as compared to PS correlates well with the larger RMS roughness seen for PαMS as compared to PS. We have shown previously[4.7] that increased surface roughness is observed in polymers with greater plasma-induced material loss. However, while the removed thickness values for PS and P4VP were similar, there was a clear change in roughness for PS that was absent in P4VP. Therefore, for P4VP, plasma-induced roughening was decoupled from material removal by plasma etching.

In Fig. 4.4(b), a rapid decrease in the etch rate corresponding to ion-damaged layer formation was observed in all polymers. However, while ion-damaged layer formation coincided with surface roughening for PS and PαMS, P4VP remained smooth.

We investigated the mechanism that prevented P4VP from roughening by examining the properties of the ion-damaged layer formed and the properties of the polymer not affected by ion bombardment.

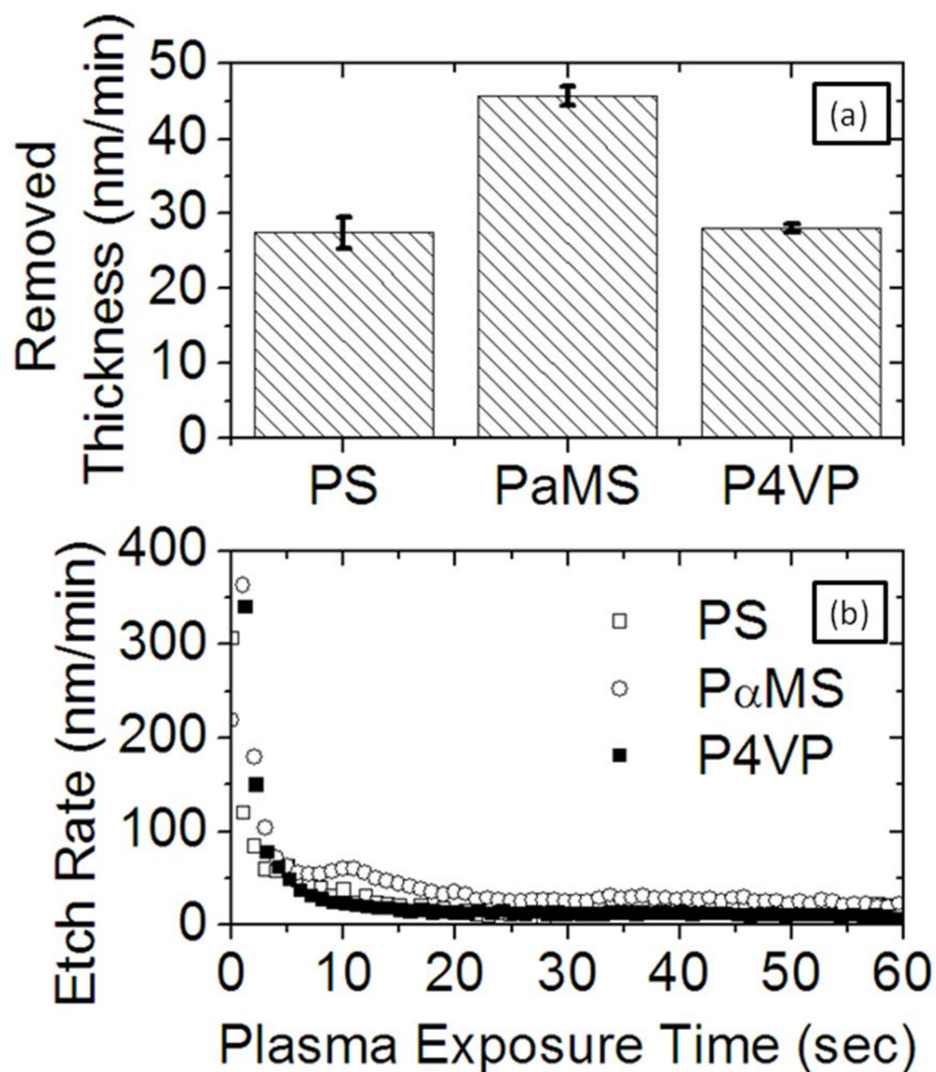

Figure 4.4: (a) Removed thickness and (b) etch rate for PS, PαMS and P4VP after Ar plasma exposure.

4.3.2 Modification of Ion-Damaged Layer by N_2 Addition

Adding small amounts of nitrogen to amorphous carbon lowers the compressive stress,[4.19,4.20] elastic modulus,[4.19,4.21] and surface roughness[4.11,4.12] of grown films. We examined whether N addition to the ion-damaged layer affected the

plasma-induced surface roughness produced by exposing PS to discharges fed with Ar/N_2 gas mixtures with increasing $\%N_2$. The ion-damaged layer formed for each condition was characterized using XPS and *in situ* ellipsometry.

In the limit of small deformation, theory[22] predicts the amplitude (A) and wavelength (λ) of buckling-induced surface roughness are proportional to the ion-damaged layer thickness, h_f, and the cube root of its elastic modulus, E_f.

The ion-modified layer thickness, h_f, was obtained by XPS analysis. We assumed the modified layer was homogeneous in chemical composition and density and that the aromatic ring structure of PS and P4VP was lost inside the modified layer due to ion damage.[4.23] Therefore, h_f was calculated by measuring the intensity of the π-π* shake-up peak at 291.3 eV for PS[4.24] and 292.2 eV for P4VP[4.25] for damaged and undamaged polymers. We utilize the fact that the π-π* shake-up peak intensity will decrease as the modified layer is formed and h_f is found using the equation[4.26]

$$h_f = \lambda_{IMFP} \ln \frac{I_0}{I} . \qquad (4.1)$$

Here λ_{IMFP} is the inelastic mean free path, and I_0 and I are the unattenuated and attenuated π-π* shake-up peak intensities, respectively. Assuming that the density remained constant and that λ_{IMFP} was 2.8 nm,[4.27] we determined the dependence of h_f in PS with ion energy and increasing $\%N_2$ and in P4VP with ion energy in Fig. 4.5. For all conditions and polymers, the ion-damaged layer thickness showed similar values that were mainly dependent on the maximum ion energy.

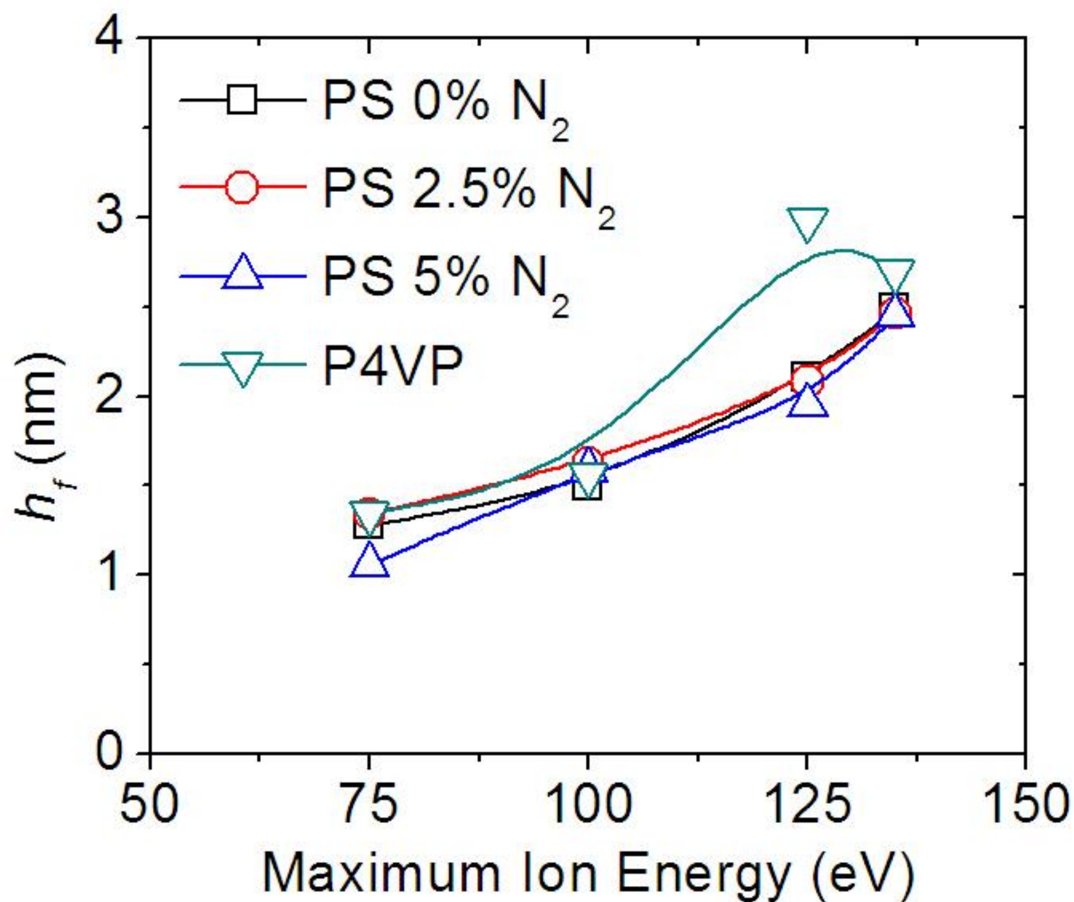

Figure 4.5: Dependence of ion-damaged layer thickness, h_f, on maximum ion energy for PS exposed to 0%, 2.5% and 5% N_2 added to an Ar discharge and P4VP exposed to an Ar discharge.

The complex index of refraction, *n* and *k*, of the ion-damaged layer was obtained from *in situ* ellipsometry measurements made during plasma exposure. The modified layer thickness h_f obtained by XPS was used in the three-layer optical model to simulate values of Ψ and Δ. The simulated values were then fitted with experimental values of Ψ and Δ by varying the PS thickness and modified layer complex index of refraction *n* and *k*. An example of this procedure is shown in Fig. 4.6 for PS exposed to Ar discharges with increasing %N_2 at 100 eV maximum ion energy. This analysis

has been explained in detail for the case of PS exposed to pure Ar at 100 eV in a previous publication.[4.7] The modified layer is treated as a nitrogen-containing amorphous carbon layer for which the relationship between n and k to density, ρ, and E_f is known.[4.19,4.20,4.28] Values for ρ and E_f are shown in Fig. 4.7.

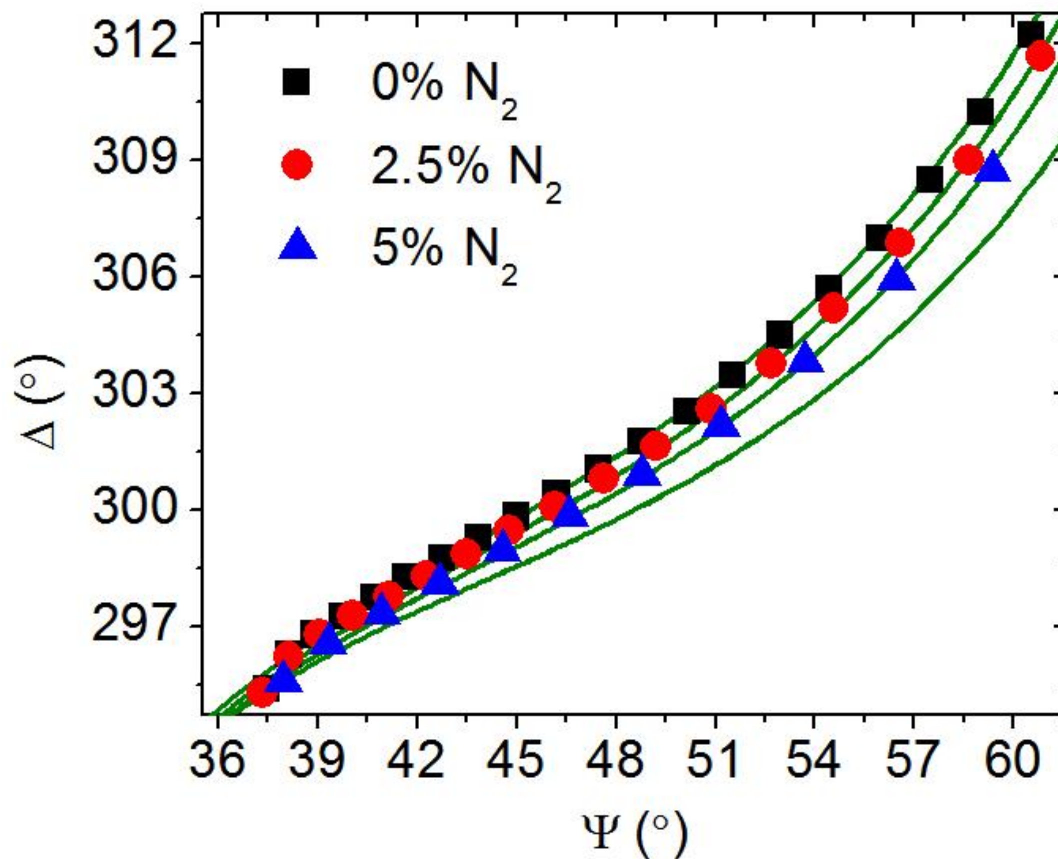

Figure 4.6: Ψ-Δ plot for PS exposed to 0%, 2.5% and 5%N_2 added to an Ar discharge.

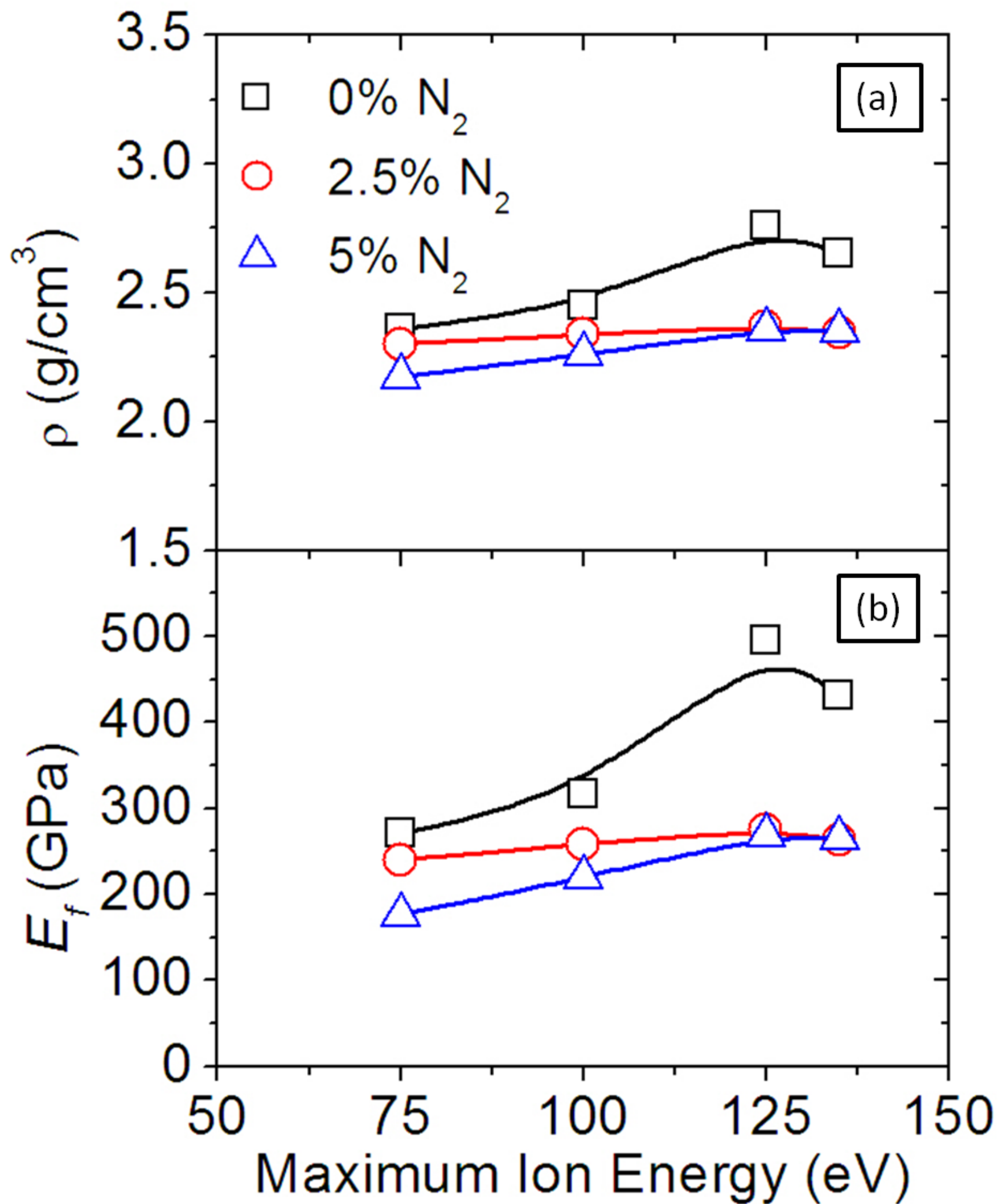

Figure 4.7: Dependence of (a) density, ρ, and (b) elastic modulus, E_f, of the ion-damaged layer on maximum ion energy for PS exposed to 0%, 2.5% and 5% N_2 added to an Ar discharge.

While there was an overall trend of increasing values with ion energy, adding $\%N_2$ lowered the derived values of ρ and E_f. Therefore, the ion-damaged layer softened with $\%N_2$, which is consistent with the results of N addition in grown amorphous carbon films.[4.24] However, as shown in Fig. 4.8, the impact on surface roughness was ambiguous. The measured values of A determined by AFM showed equivalent or greater values with an increase in $\%N_2$, whereas λ was consistently shorter.

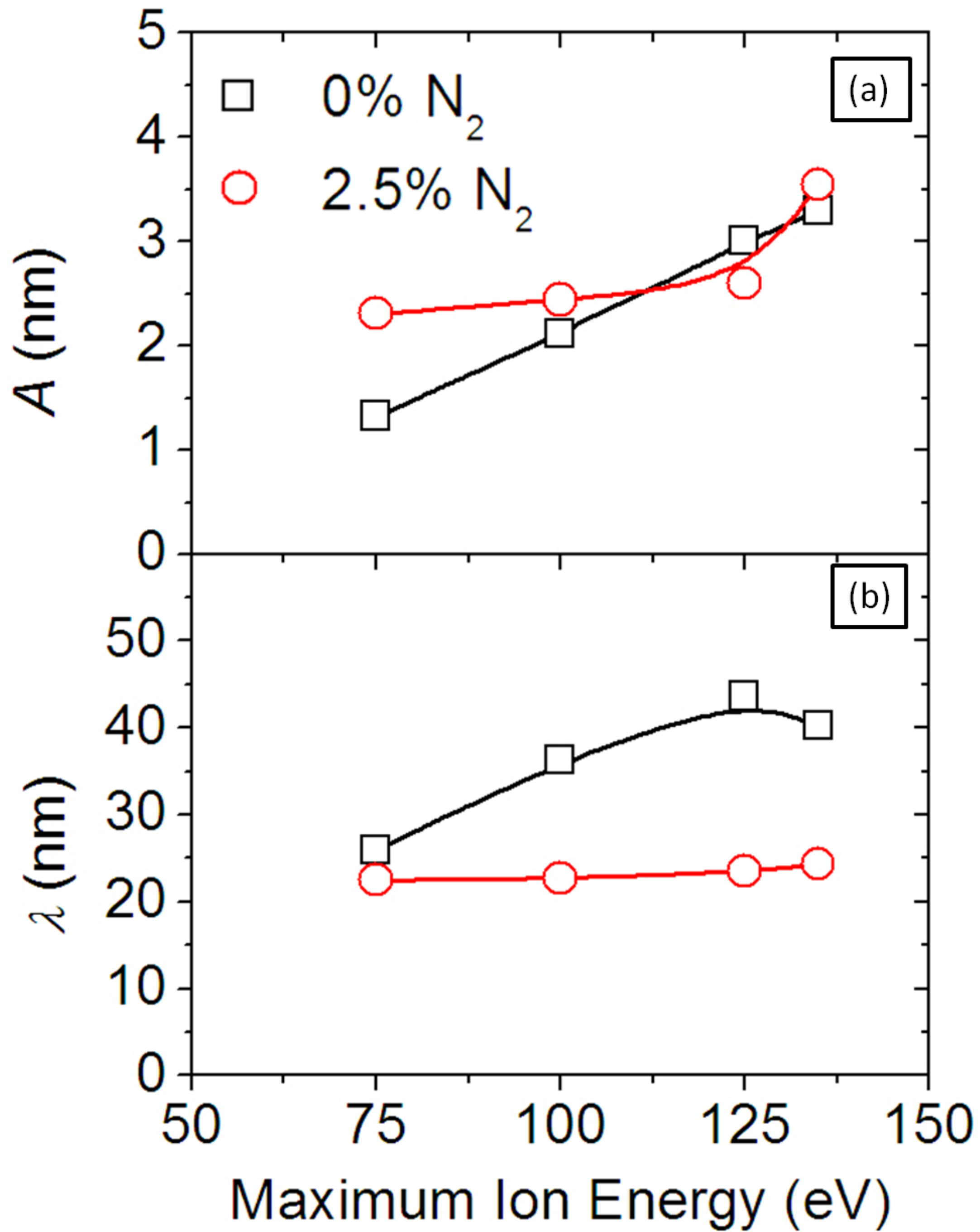

Figure 4.8: Dependence of (a) amplitude, A, and (b) wavelength, λ, on maximum ion energy 0% and 2.5% N_2 added to an Ar discharge.

In Fig. 4.9, examination of the AFM scans after plasma exposure without N_2 and with N_2 showed markedly different surface morphology. While the roughness without N_2 was in the form of smooth, rounded bumps, adding N_2 changed the morphology to sharp, jagged spikes. We concluded that the surface roughness after Ar/N_2 plasma exposure deviated from the predicted buckled morphology most likely due to the addition of a radical etching component. Enhanced etching by radicals was demonstrated by plotting etch rate versus %N, and is shown in Fig. 4.10.

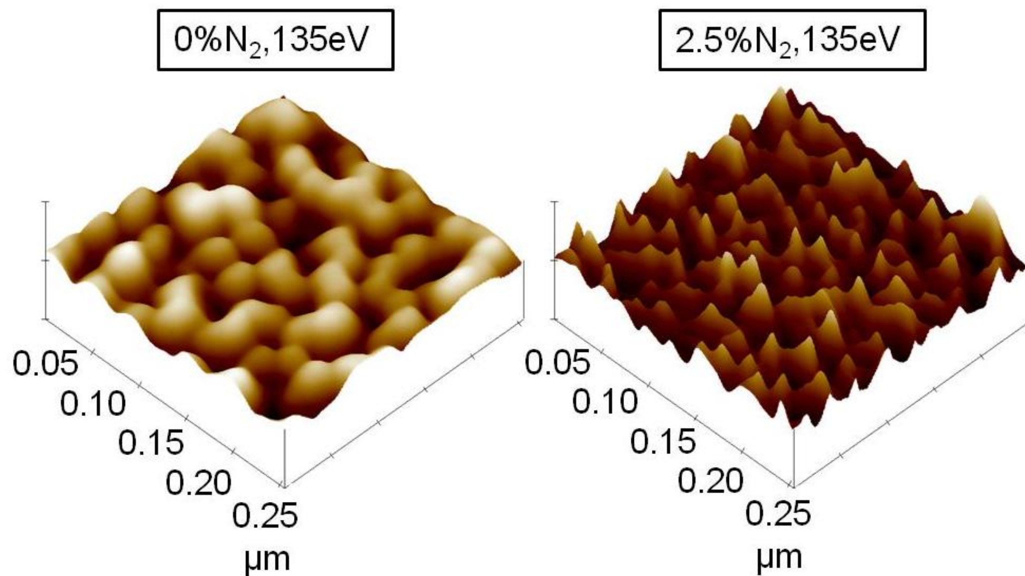

Figure 4.9: AFM images of PS exposed to 0% and 2.5% N_2 added to an Ar discharge with maximum Ar^+ ion energy at 135 eV.

We showed in Ref. 4.8 that the effect of the ion-damaged layer on surface roughness can be enhanced by heating plasma-processed polymer films above their glass transition temperature. The elastic modulus of the polymer underlayer decreases by four orders of magnitude when heated above the glass transition temperature, while the ion-damaged layer properties stay the same. We produced anisotropic wrinkling in films by scratching a line in films with a diamond scribe after plasma exposure and before heating. Therefore, wrinkling occurred in only one direction. As shown in Fig. 4.11, the amplitude and wavelength of the resulting surface morphology of the plasma processed films was magnified by many times. The addition of N to the ion-damaged layer was then observed to cause substantial decreases in *A* and *λ*.

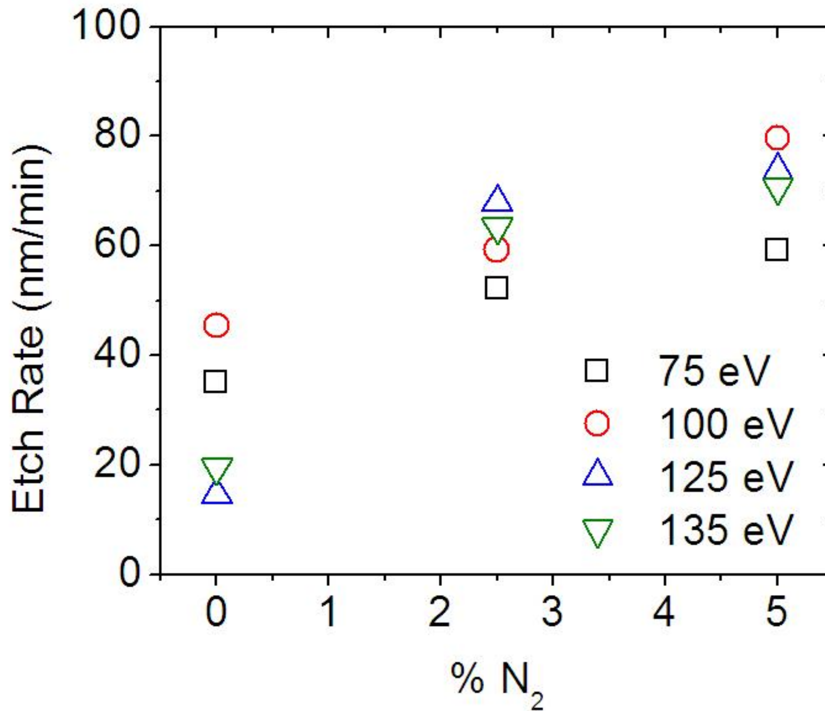

Figure 4.10: Etch rate versus %N_2 addition in an Ar discharge is shown for PS from 75 eV to 135 eV.

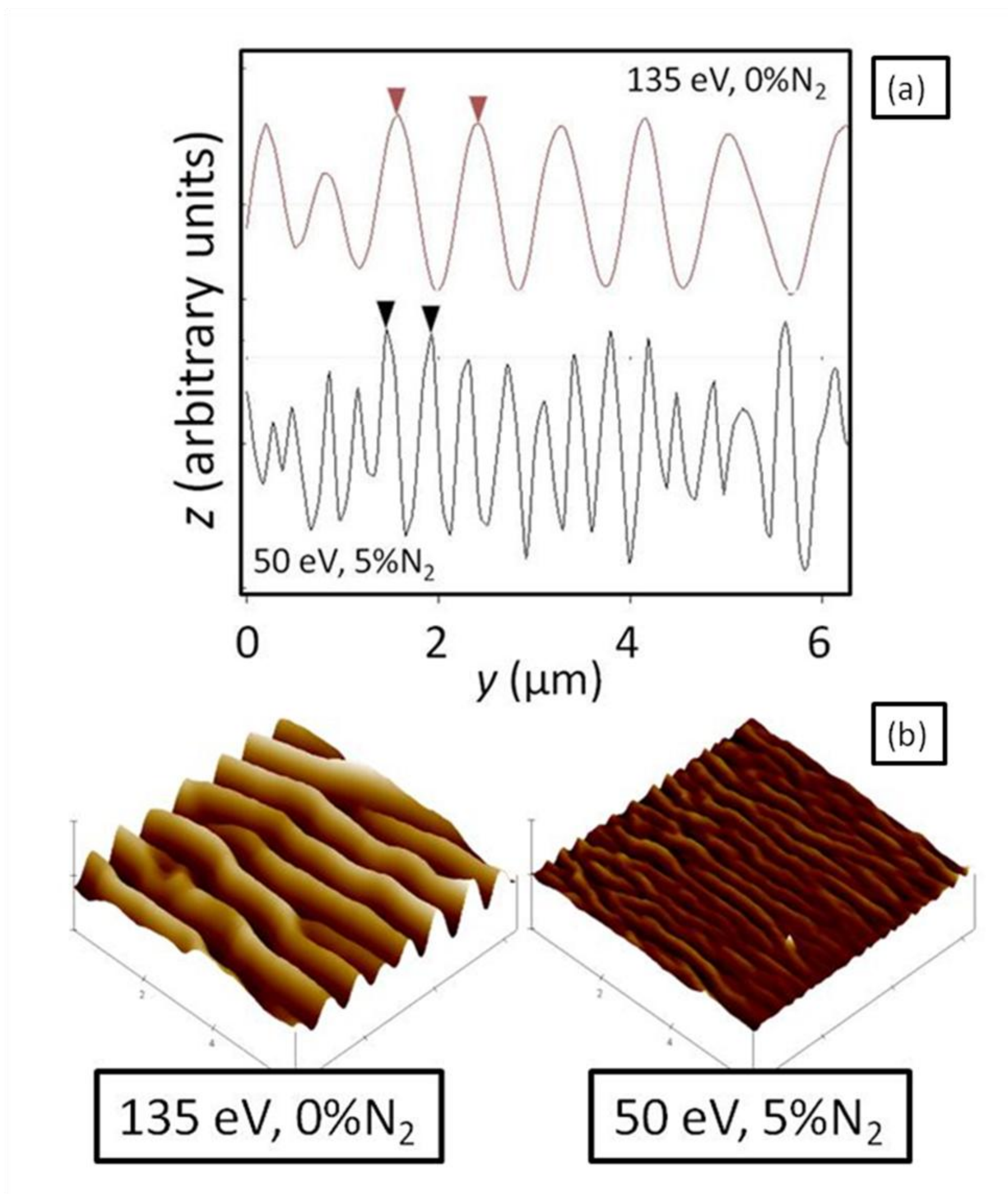

Figure 4.11: (a) AFM section scan and (b) AFM images of PS exposed to 0% N_2 in an Ar discharge at 135 eV maximum ion energy and 5% N_2 in an Ar discharge at 50 eV maximum ion energy, both heated afterwards to 110 °C.

A plot of A and λ with ion energy and $\%N_2$ is shown in Fig. 4.12 for plasma-processed PS after heating. The relationship was very similar to the relationship of E_f with ion energy and $\%N_2$ that was shown in Fig. 4.7.

Therefore, the softening effect of N addition to the ion-damaged layer was established. We were not able to compare values of A and λ of plasma-induced surface roughness between PS and P4VP since P4VP showed no presence of surface morphology, as shown in Fig. 4.13. However, when heating PS and P4VP above their respective glass transition temperatures T_g, the enhanced surface morphologies could be compared. In Fig. 4.14, we compared λ of Ar/N_2 plasma processed PS and Ar plasma processed P4VP with ion energy after heating. We expected that if the cause of smoothness in P4VP was the softening of the ion-damaged layer, the measured λ would be less for P4VP than for PS. The reason is that both the ion-damaged layer thickness (Fig. 4.5) and the elastic modulus above T_g[4.29] is the same for unmodified PS and P4VP. Therefore, the wrinkled surface morphology should only depend on the elastic modulus of the ion-damaged layer. However, P4VP instead shows significantly greater values for λ as compared to PS, which would indicate a much larger ion-damaged layer elastic modulus.

By ellipsometry analysis, we determined the elastic modulus of the ion-damaged layer of P4VP with increasing maximum ion energy and compared the values to PS under Ar and Ar/N_2 plasma discharge conditions. The results are shown in Fig. 4.15. The ion-damaged layer elastic modulus of P4VP was very similar to PS and in conjunction with the ion-damaged layer thickness results shown in Fig. 4.5, we

concluded that the ion-damaged layer did not change significantly between Ar plasma-exposed PS and P4VP.

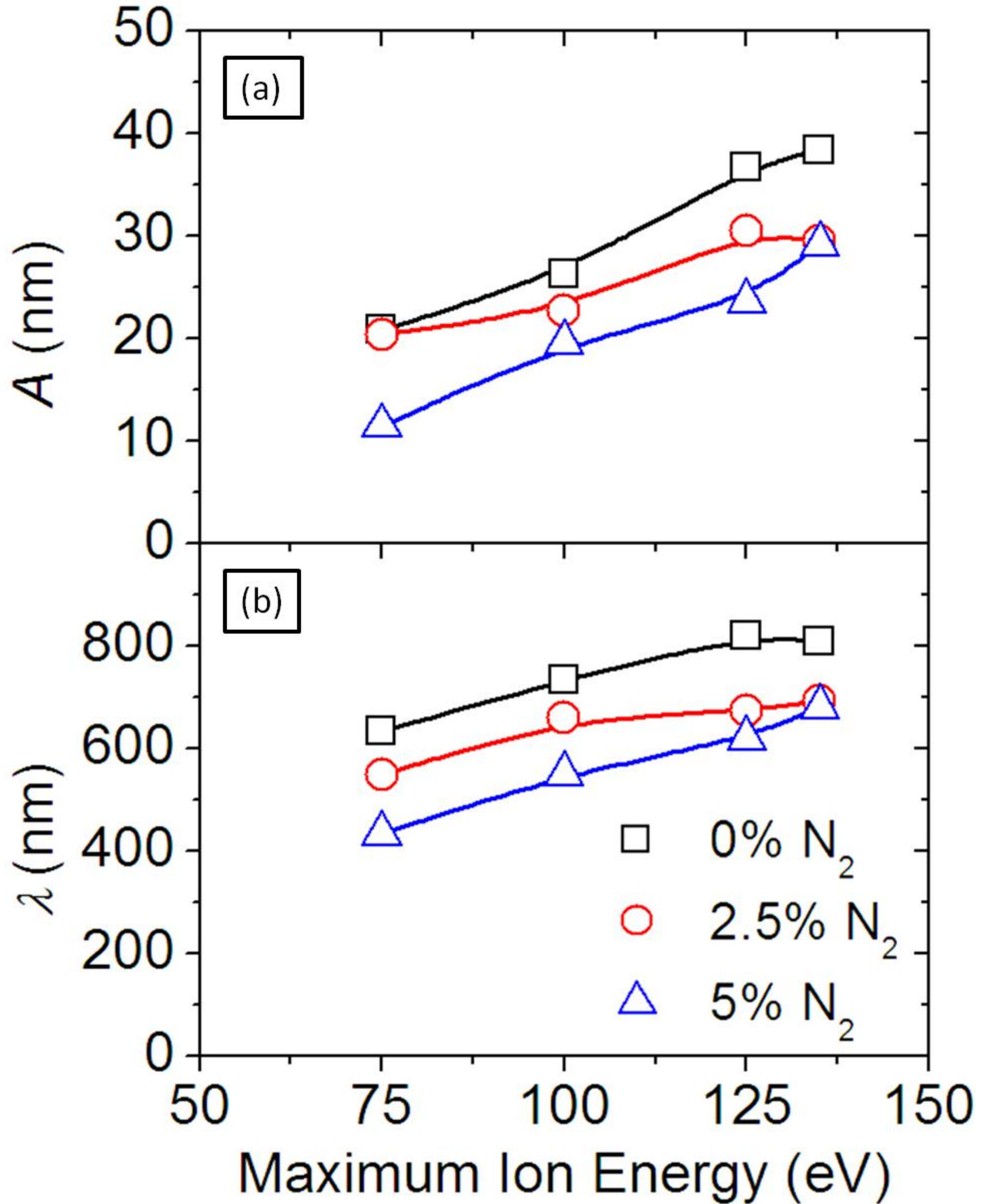

Figure 4.12: Dependence of (a) amplitude, A, and (b) wavelength, λ, on maximum ion energy for PS exposed to 0%, 2.5% and 5% N_2 added to an Ar discharge and then heated to 110 °C.

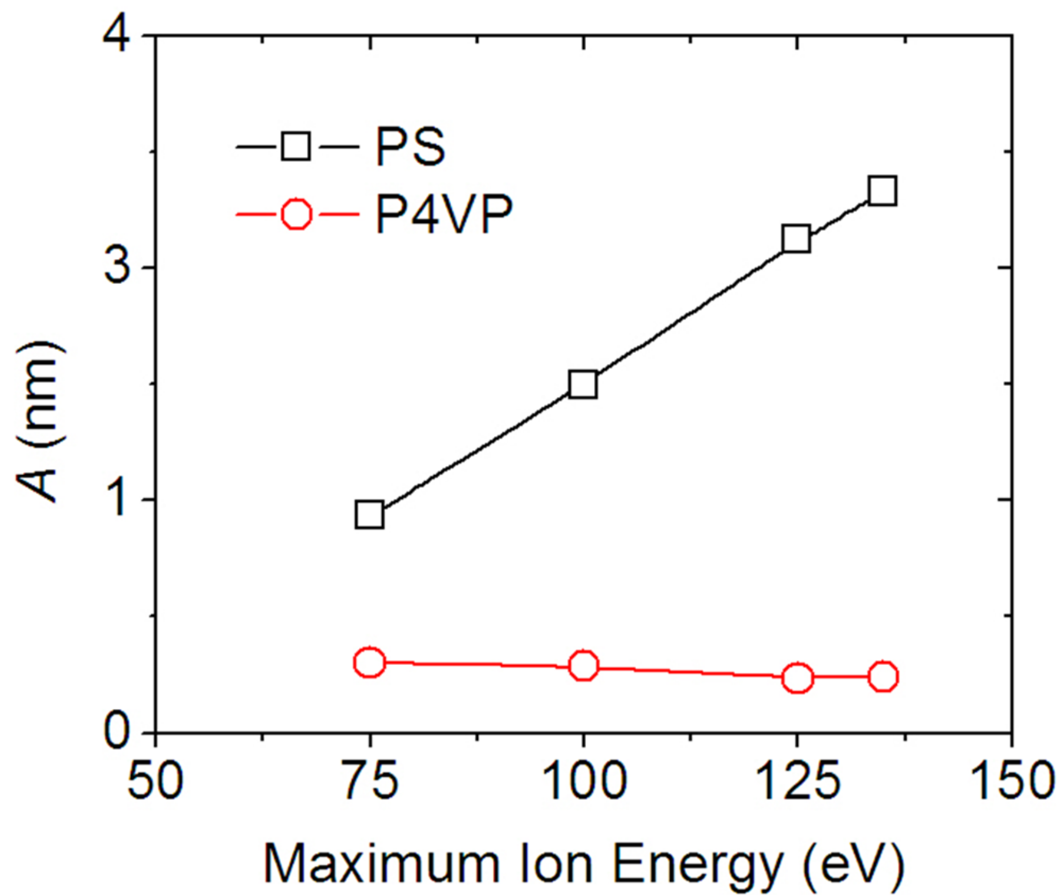

Figure 4.13: Comparison of the dependence of amplitude, *A*, in PS and P4VP on maximum ion energy after exposure to an Ar discharge.

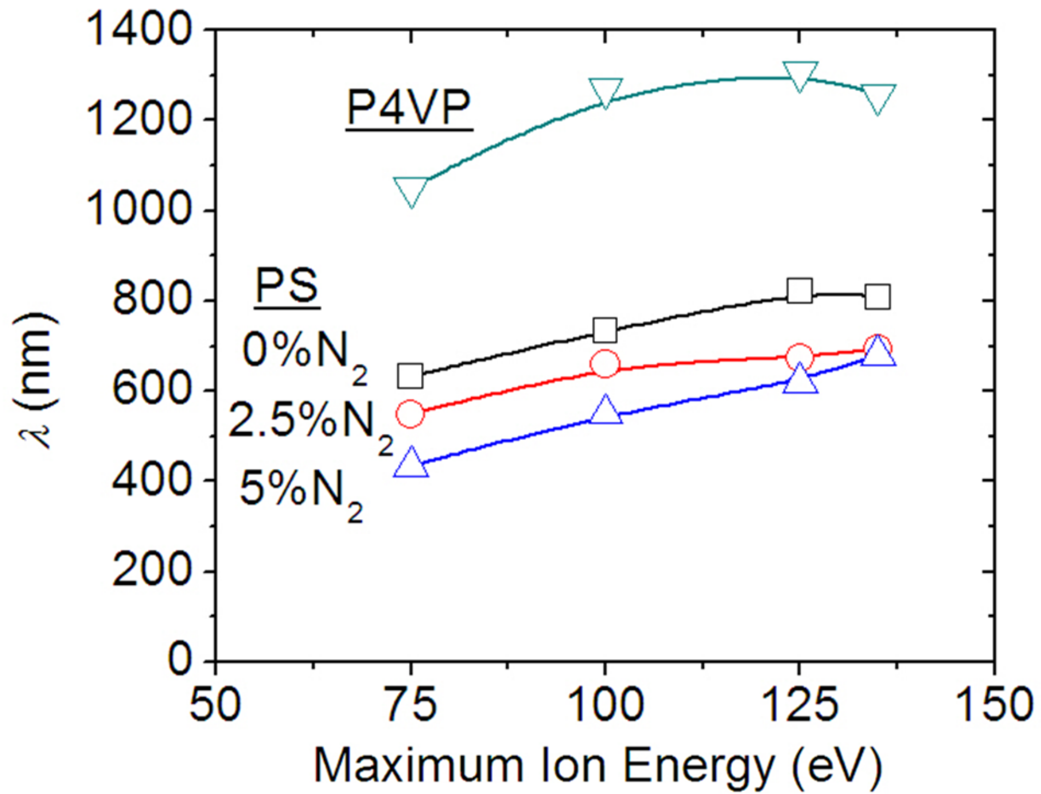

Figure 4.14: Comparison of the dependence of wavelength, λ, on maximum ion energy in PS after exposure to Ar and Ar/N_2 discharges and P4VP after exposure to an Ar discharge and then both heated above their respective T_g (PS, 110 °C, and P4VP, 155 °C).

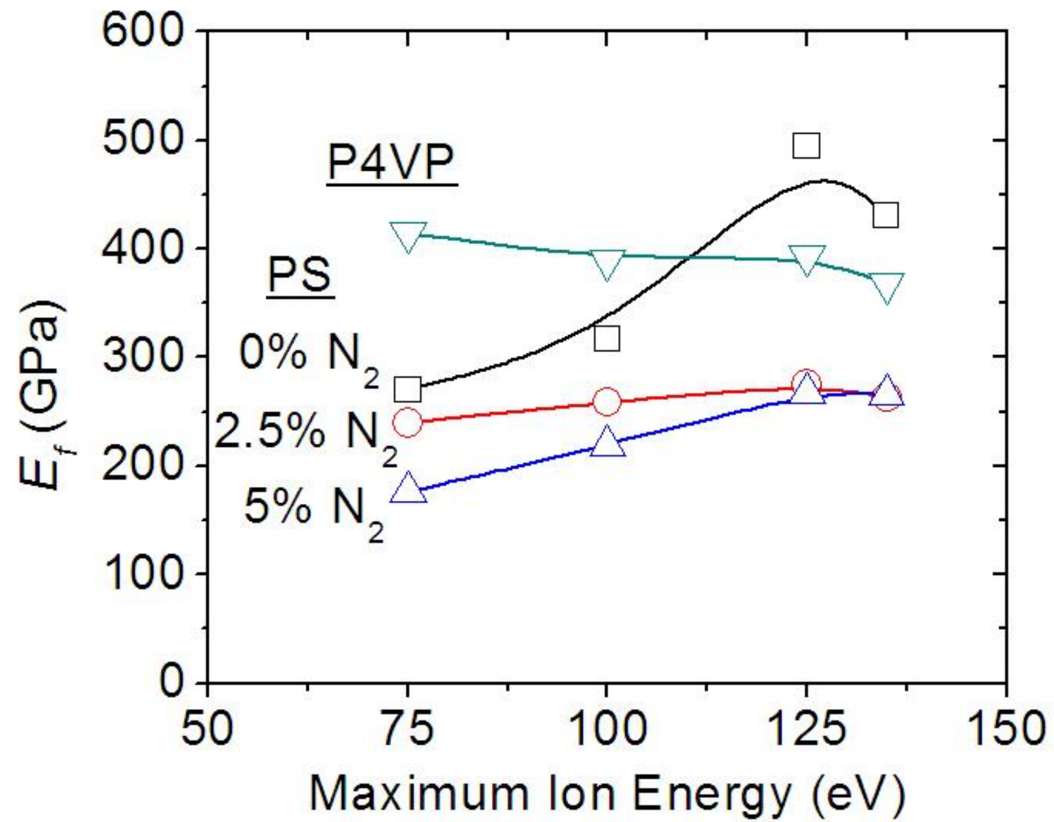

Figure 4.15: Comparison of ion-damaged layer elastic modulus, E_f, of Ar/N_2 exposed PS and Ar exposed P4VP versus maximum ion energy.

4.3.3 Modification of Polymer Underlayer by Plasma VUV Radiation

We saw in the Section 4.3.2 that there was little difference in the ion-damaged layer properties of Ar plasma-exposed PS and P4VP, but that above T_g wrinkling was much greater in P4VP. If an additional, thicker layer was formed below the ion damaged layer, it may suppress the buckling instability when the ion-damaged layer is formed during plasma exposure. In addition, when the plasma-exposed P4VP film is heated above T_g causing a several orders of magnitude decrease in the unmodified P4VP underlayer, both layers could act in congress to wrinkle the polymer to roughness values much greater than if the ion-damaged layer acted alone.

We reported previously that VUV radiation of Ar discharges caused significant material removal in PαMS, but showed no effect on PS. Therefore, we investigated the effect of VUV irradiation on P4VP. For this PS, PαMS, and P4VP were exposed to the VUV radiation component of an Ar discharge by placing a MgF_2 window on top of the polymer films to block ion bombardment. Fig. 4.16 shows the change in refractive index using real-time *in situ* ellipsometry. P4VP exhibited a large increase in refractive index, while PS and PαMS showed no increase. A refractive index increase relates to an increase of the polymer density in a film. This result indicates that VUV irradiation may have crosslinked some of the P4VP.

However, in Fig. 4.15, our ellipsometric results of fully exposed P4VP (ions and VUV) showed that the ion-damaged layer elastic modulus was similar in properties to PS. Since the optical property changed measured by ellipsometry is the combined effect of all surface modification occurring within the polymer film, a refractive index change due to VUV crosslinking would impact the overall

ellipsometric response during the full plasma exposure. Therefore, the ion-damaged layer may possibly be softened by nitrogen addition from the polymer structure in conjunction with crosslinking occurring below it, which may produce a refractive index change that looks similar to the PS condition if the two layers are treated as a single layer.

In addition, VUV-exposed P4VP was examined by XPS and the change in the XPS N1*s* spectra is shown in Fig. 4.17. An increase in quaternization of the nitrogen atom in the pyridine ring is indicated by these data, and would be consistent with crosslinking. This result further supports VUV crosslinking in P4VP.

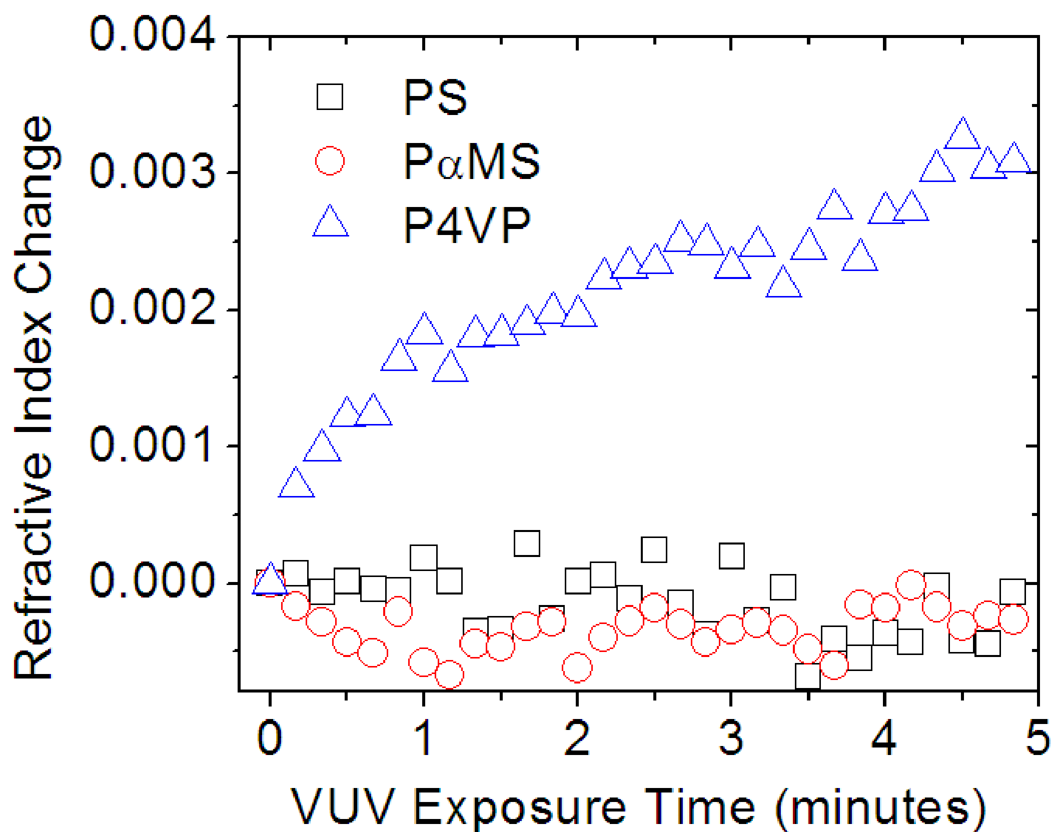

Figure 4.16: Dependence of the change in refractive index on VUV exposure time for PS, PαMS, and P4VP.

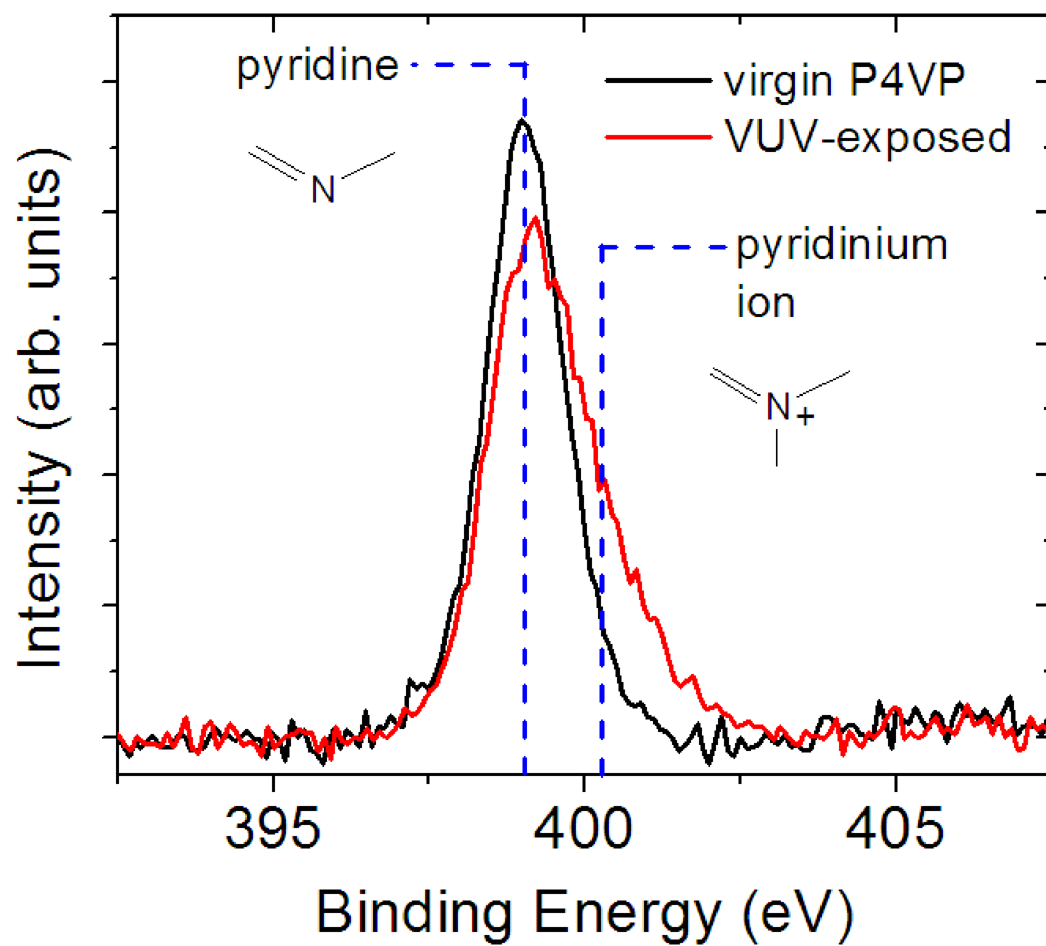

Figure 4.17: XPS N 1*s* spectra of unexposed P4VP and VUV-exposed P4VP.

4.3.4 Discussion

From our results, we have established mechanisms for the resistance of surface roughening in P4VP and the great enhancement of surface roughening above its T_g. The mechanisms are shown schematically in Fig. 4.18. For the case of PS, the creation of an ion-damaged layer after plasma exposure caused a buckling instability that formed nanoscale wrinkles at the surface. Heating the plasma-exposed PS above T_g reduced the polymer underlayer elastic modulus and greatly increased the surface roughness wavelength and amplitude. For P4VP, plasma exposure created an ion-damaged layer in addition to a VUV crosslinked layer. In Fig. 4.5, it was shown that the ion-damaged layer thickness was on the order of a few nanometers. In contrast, VUV penetration depths range from tens to hundreds of nanometers.[4.30] The increase in the elastic modulus of the polymer underlayer prevented the buckling instability from occurring and wrinkles from forming. Therefore, P4VP showed complete smoothness after plasma exposure even though an ion-damaged layer was created. However, heating P4VP above T_g rapidly reduced the elastic modulus of the polymer underlayer below the ion-damaged and VUV crosslinked layers. A buckling instability occurred between the softened polymer underlayer and the combined ion-damaged and crosslinked layer that produced surface morphology much greater than in the case of wrinkling in PS above T_g.

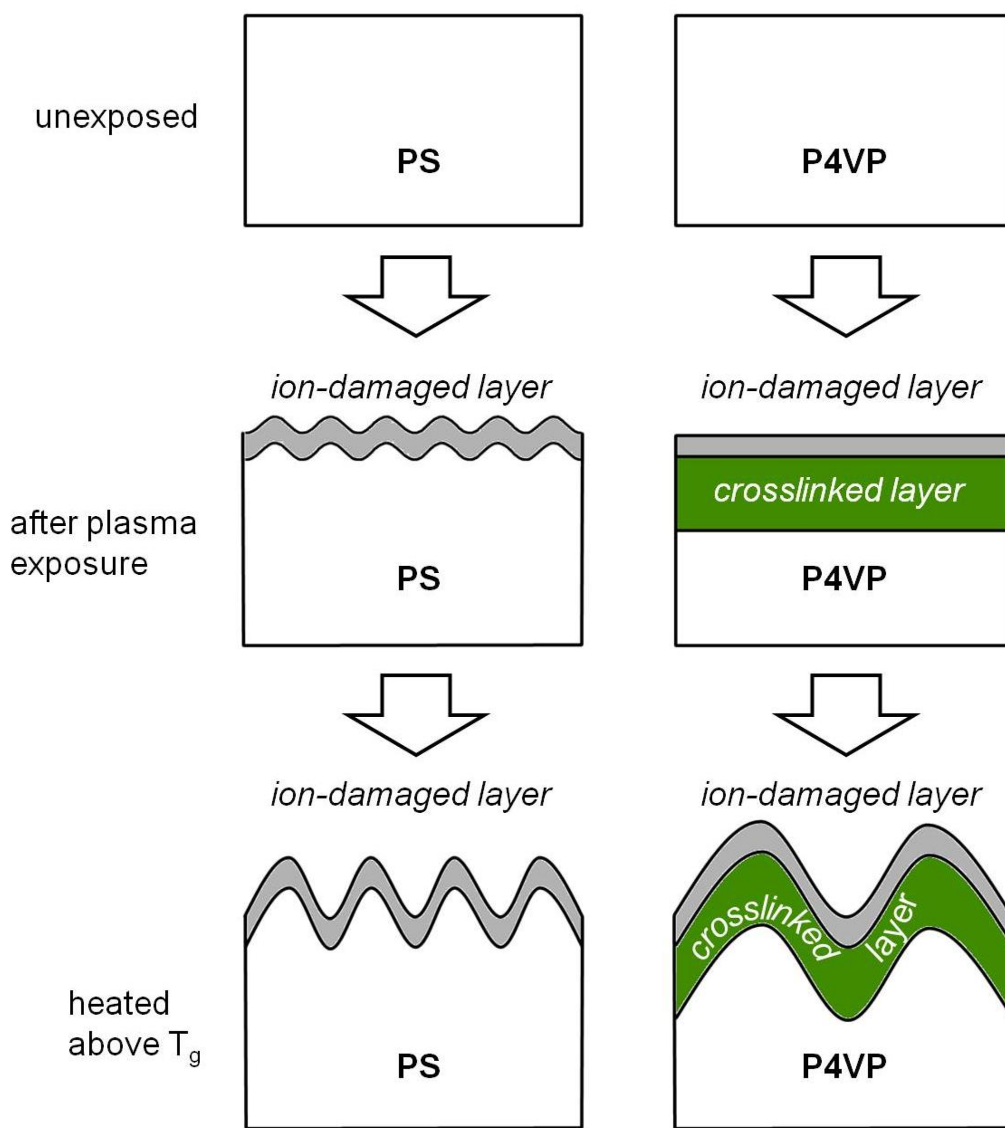

Figure 4.18: Schematic of the mechanisms of surface morphology development in PS and P4VP after plasma exposure and after plasma exposure and subsequent heating above glass transition temperature.

4.4 Conclusions

Understanding etch phenomena, such as the formation of LER in polymer resists during plasma processing is becoming increasingly important as the CD of devices continue to shrink. The lack of surface and line edge roughness in P4VP resist structures during plasma processing is believed to offer a potential approach to control plasma-induced LER for nanoscale manufacturing. Plasma-induced surface roughening in PS has been linked to wrinkling caused by the formation of an ion-damaged layer at the polymer surface. While nitrogen addition causes significant softening of the ion-damaged layer, the properties of the ion-damaged layers that are formed in Ar plasma-exposed PS and P4VP are very similar. We observed that crosslinking by VUV irradiation of P4VP caused an increase in the elastic modulus of P4VP below the ion-damaged layer. This VUV modification is not seen for PS. It is likely that VUV modification of P4VP, possibly in conjunction with softening of the ion-damaged layer by the presence of nitrogen, prevents wrinkling of P4VP surfaces, enabling the elimination of LER in 3D structures resulting from plasma etch.

ACKNOWLEDGEMENTS

The authors gratefully acknowledge financial support of this work by the National Science Foundation under award Nanoscale Interdisciplinary Research Team (NIRT) No. CTS-0506988. T. Corrigan of LPS is thanked for SEM analysis.

Chapter 5: Molecular Structure Effects on Dry Etching Behavior of Si-containing Resists in Oxygen Plasma

To be submitted to J. Vac. Sci. Technol. B, 2010

R. L. Bruce, T. Lin, R. J. Phaneuf, G. S. Oehrlein, W. Bell, B. Long and C. G. Willson

ABSTRACT

We have studied the influence of Si-O bonding in the polymer structure of Si-containing resists on O_2 plasma etch behavior. Three polymers were synthesized with the same Si weight percent (12.1%) and varying number of Si-O bonds (0, 1 or 2). The etch resistance during the plasma process was measured by monitoring the film thickness removed using real-time *in situ* ellipsometry. After plasma exposure surface chemical changes and roughness were characterized by x-ray photoelectron spectroscopy and atomic force microscopy, respectively. For O_2 plasma exposure without substrate bias, all polymers showed the formation of a ~1 nm SiO_2 layer at the surface that acted as a barrier to further oxygen etching. Adding Si-O bonds to the polymer structure greatly reduced the etch rate and Si loss during plasma etching relative to the case of no such bonds. Polymers with one Si-O bond in the polymer structure showed identical etch behavior to polymers with two Si-O bonds. However, increasing Si-O bonds decreased the glass transition temperature of the polymer, leading to micron-sized wrinkles after plasma exposure. When a substrate bias was applied, the etch rate and Si loss increased due to sputtering of the SiO_2 layer by

energetic ions. For 90% N_2 / O_2 discharges with substrate bias, a typical oxygen-based pattern transfer plasma, the etch rates were lower and the SiO_2 layer thicknesses formed were larger compared to O_2 discharges with substrate bias. For all gas discharge conditions, polymers with pre-existing Si-O bonds showed less Si loss.

5.1 Introduction

Silicon-containing resists are used in many lithographic technologies such as photolithography,[5.1,5.2,5.3] top surface imaging,[5.4,5.5,5.6] block copolymer lithography[5.7] and nanoimprint lithography.[5.8,5.9,5.10] In each case, an oxygen-based plasma transfers a pattern in the resist into an underlying organic layer. The oxygen reacts and forms SiO_2 at the resist surface,[5.11,5.12,5.13] which acts as a barrier while etching proceeds uninhibited in the organic underlayer.

Increasing the Si content in Si-containing resists increases the etch resistance and overall etch selectivity, but degrades lithographic performance by reducing transparency to UV light and solubility.[5.14,5.15] It has been widely reported that approximately 12 weight percent (wt%) Si is required for acceptable etch selectivity (10:1).[5.9] However, this value is based on empirical etch rate ratio measurements without considering the nature of Si atomic bonding within the resist. In particular, whether Si is bonded to carbon or oxygen may influence the etching behavior if the mechanism of etch resistance is SiO_2 surface layer formation. In this article, we report studies on the effects of increasing the amount of Si-O bonds while maintaining 12.1 wt% Si in the polymer structure of Si-containing resists on their etch behavior in oxygen-based plasmas.

The organization of this paper is as follows. We first describe the experimental setup in Sec. 5.2. In sections 5.3.1-5.3.3 we describe the influence of an O_2 plasma without substrate bias on the properties of polymers with varying Si-O bonds. The etching kinetics, modified surface characterization, and surface roughness development are described in sections 5.3.1, 5.3.2, and 5.3.3, respectively. In section

5.3.4 we describe the effect of adding substrate bias and varying the gas chemistry (from O_2 to 90% N_2 / 10% O_2) on the plasma modification behavior. In section 5.3.5 the mechanism of etching in Si and Si-O containing polymers is discussed.

5.2 Experimental Setup

5.2.1 Description of Materials

Three polymers containing equivalent weight percent Si but varying numbers of Si-O bonds per Si atom were synthesized. The polymer structures are described in Table 5.1 and shown in Fig. 5.1. The polymer hereafter referred to as P(Si) contained no Si-O bonds in the polymer structure (Fig. 5.1(a)), that referred to as P(Si-O) contained one Si-O bond per monomer (Fig. 5.1(b)), and that referred to as P(Si-O2) contained two Si-O bonds per monomer (Fig. 5.1(c)). The procedures for polymer synthesis were described previously,[5.16] and the important parameters of each polymer are given in Table 5.1. The polymers P(Si) and P(Si-O) were copolymerized with methyl methacrylate (MMA) so that the weight percent Si of the resulting polymers were constant and the same as P(Si-O2) (12.1 wt% Si). All polymers were spun onto Si wafers at ~400 nm thickness and baked at 90 °C.

Polymer	#Si-O Bonds	Chemical Name	Si Monomer: MMA Ratio	Weight percent silicon (%)	T_g[a] (°C)	Molecular Weight[b] (g/mol)
P(Si)	0	Poly(trimethylsilylmethyl methacrylate)-b-poly(methyl methacrylate)	1:0.6	12.1	94	61000
P(Si-O)	1	poly[3-(methoxydimethylsilyl) propyl methacrylate]-b-poly(methyl methacrylate)	1:0.16	12.1	Unknown; T_g < RT	68000
P(Si-O2)	2	poly[3-(dimethoxymethylsilyl) propyl methacrylate]	-	12.1	Unknown; T_g < RT	49000

[a]As determined by differential scanning calorimetry.

[b]As determined by gas permeation chromatography.

Table 5.1: Important parameters of polymers P(Si), P(Si-O), and P(Si-O2).

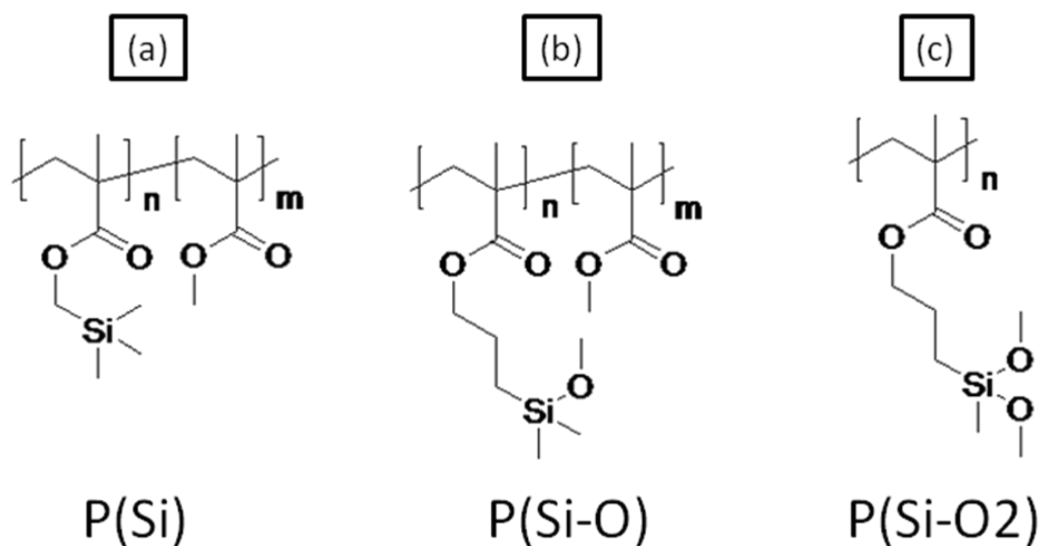

Figure 5.1: Molecular structures of (a) P(Si), (b) P(Si-O) and (c) P(Si-O2).

5.2.2 Plasma Processing

The inductively coupled plasma (ICP) reactor used in this study has been described in previous publications.[5.17,5.18] The configuration is a planar coil on top of a quartz window that is powered through an L-type matching network with a 13.56 MHz RF power supply. Ion energy on a 125 mm diameter substrate was independently controlled using a 3.7 MHz RF bias power supply. The distance between the quartz window and substrate was 14.5 cm. The temperature of the bottom electrode was maintained at 10 °C using a chiller. 2.5×2.5 cm^2 polymer-coated Si substrates were thermally coupled to this electrode. The chamber base pressure before processing was 5×10^{-5} Torr. The processing conditions used were 10 mTorr operating pressure fixed by a throttle valve, 40 SCCM (SCCM denotes cubic centimeter per minute at STP) flow rate, and an inductive power set to 300W.

Three plasma processing conditions were used: O_2 with no substrate bias, O_2 with -100V substrate bias, and 90% N_2 / 10% O_2 with -100V substrate bias. The ion current densities for O_2 and 90% N_2 /10% O_2 gas discharges were 4.7 mA/cm^2 and 4.9 mA/cm^2, respectively.

5.2.3 Surface Characterization

The polymer film thickness during plasma processing was measured *in situ* using a rotating compensator He-Ne ellipsometer operating in the polarizer-

compensator-sample-analyzer configuration. The angle of incidence was 71.3° and for the simulation of ellipsometric data the Si substrate refractive index was fixed at 3.866-0.028*i*.[5.19]

X-ray photoelectron spectroscopy (XPS) analysis was performed in a Vacuum Generators ESCA Mk II surface analysis chamber using a nonmonochromatized Mg Kα X-ray source (1253.6 eV). 2.5×2.5 cm^2 samples were transferred in air immediately after processing. Spectra were obtained at normal emission relative to the surface and in constant analyzer energy mode at 20 eV pass energy. The analyzer resolution was approximately 0.2 eV and the resolution of the spectra was limited by the linewidth of the x-ray source, approximately 1 eV.

Atomic force microscopy (AFM) measurements were performed on virgin and etched samples. Etched samples were transferred to the AFM in air. The surface roughness values reported were calculated from the root mean square (rms) of the surface profile after the measurement.

5.3 Results and Discussion

5.3.1 Etching Kinetics

Polymer films were etched in an O_2 discharge without substrate bias for 300 seconds. The thickness removed versus plasma exposure time measured by *in situ* ellipsometry is shown in Fig. 2(a). P(Si-O) and P(Si-O2) showed very similar etching behavior, while P(Si) showed significantly more thickness removed. Ellipsometry data for P(Si-O2) is only shown for 150 seconds as laser scattering due to substantial

roughening of the polymer surface caused disruption of the ellipsometric signal at later times. Polymer roughening will be discussed in Sec. 5.3.3.

The etch rate versus plasma exposure time is shown in Fig. 5.2(b). All polymers showed a qualitatively similar etching behavior: an initial high etching rate at the start of plasma exposure and a very low etching rate for long plasma exposure times. This behavior is indicative of SiO_2 layer formation at the surface that creates a barrier that limits any additional etching by the plasma. Initially, the etch rate of P(Si) was larger compared to the other polymers, leading to greater overall thickness removed. However, for all polymers, the etch rate decreased by more than 2 orders of magnitude at longest exposure times studied.

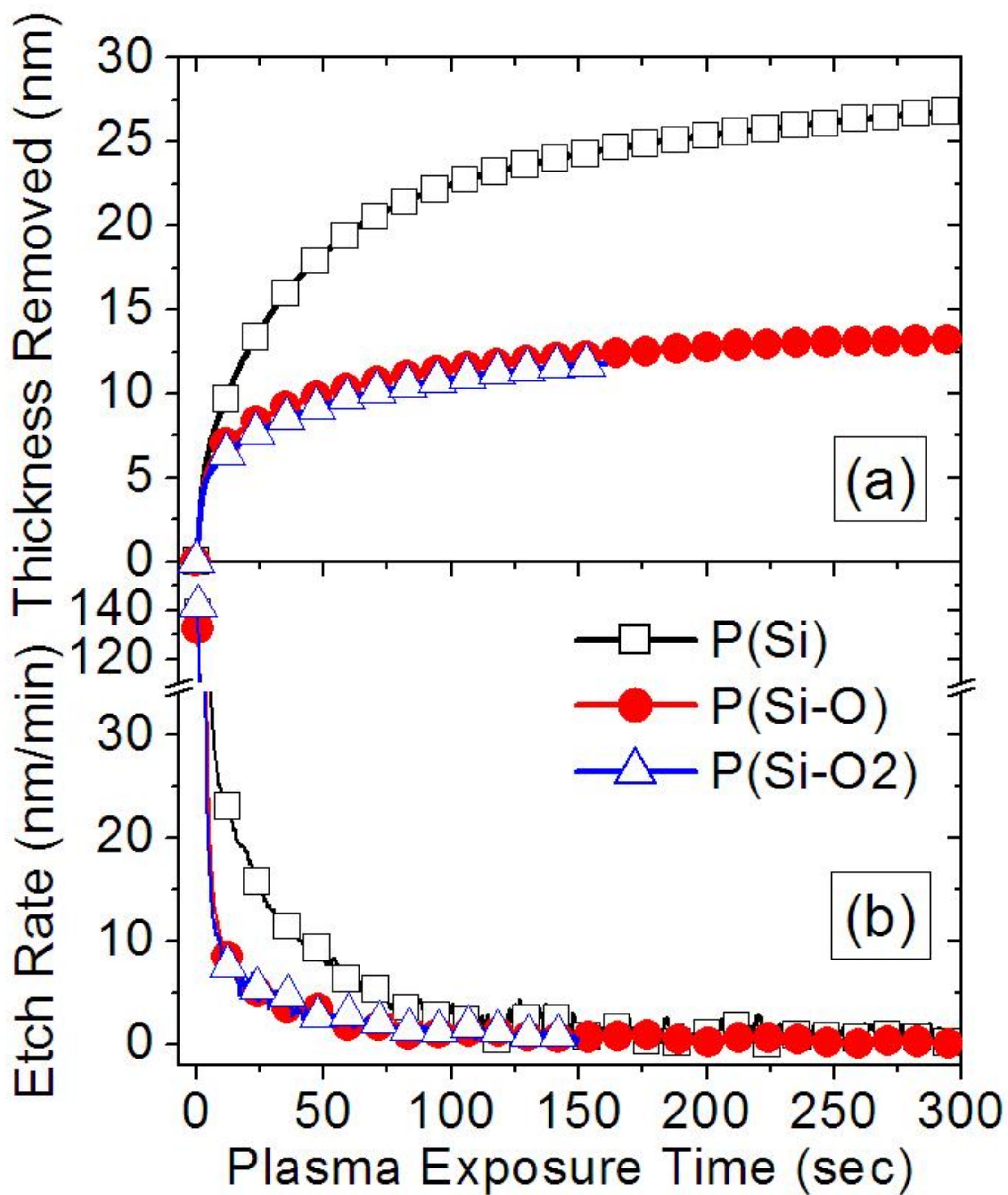

Figure 5.2: (a) Thickness removed and (b) etch rate dependence on plasma exposure time for P(Si), P(Si-O) and P(Si-O2). Polymers were etched using O_2 plasma without substrate bias.

5.3.2 XPS Analysis and SiO_2 Layer Characterization

XPS was used to measure the chemical changes in the polymer films with plasma exposure time. In Fig. 5.3, the C 1*s*, Si 2*p*, and O 1*s* spectra for the virgin polymer films and after 5 seconds and 120 seconds of plasma exposure time are shown. For all polymers, the C 1*s* peak decreased while the Si 2*p* and O 1*s* peak increased with exposure time. XPS measures chemical changes to a depth of about 10 nm and the formation of a thin SiO_2 layer at the surface would cause these changes. In the Si 2*p* spectra, the Si-C peak decreased while the Si-O peak intensity rapidly increased to a value greater than the virgin Si 2*p* peak intensity. Since no new Si atoms were introduced during the plasma etching process, the increase of the Si atomic density at the surface due to SiO_2 formation explains this behavior.

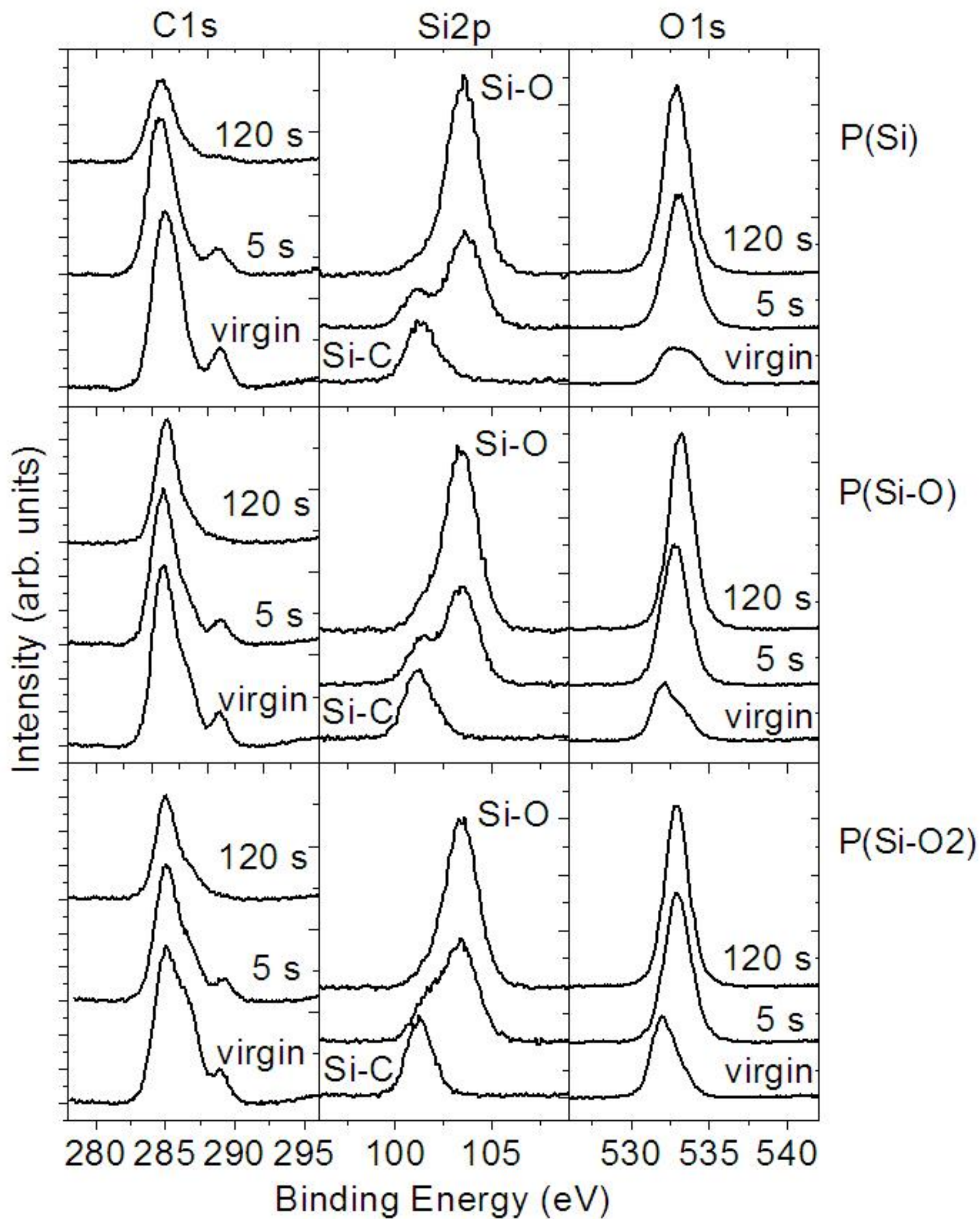

Figure 5.3: The changes in the XPS C1*s*, Si 2*p*, and O 1*s* spectra with plasma exposure time are shown for P(Si), P(Si-O), and P(Si-O2). Polymers were etched using O_2 plasma without substrate bias.

The thickness of the SiO_2 layer formed on the polymer films after plasma exposure was obtained by XPS analysis. For this we assume that the C1s peak intensity is attenuated through a homogeneous SiO_2 layer and according to the equation,[5.20]

$$d_{SiO2} = \lambda \ln \frac{I_0}{I} \qquad (5.1)$$

where d_{SiO2} is the SiO_2 layer thickness, λ is the inelastic mean free path through SiO_2, I_0 is the unattenuated C1s peak intensity and I is the attenuated C1s peak intensity. For λ, we used a value of 2.2 nm from the literature[5.21]. We assumed that λ_{IMFP} did not depend on the nature of the SiO_2 layer grown on the polymers. A plot of SiO_2 layer thickness versus plasma exposure time is shown in Fig. 5.4. P(Si) showed formation of slightly larger values of SiO_2 layer thickness compared to the other polymers.

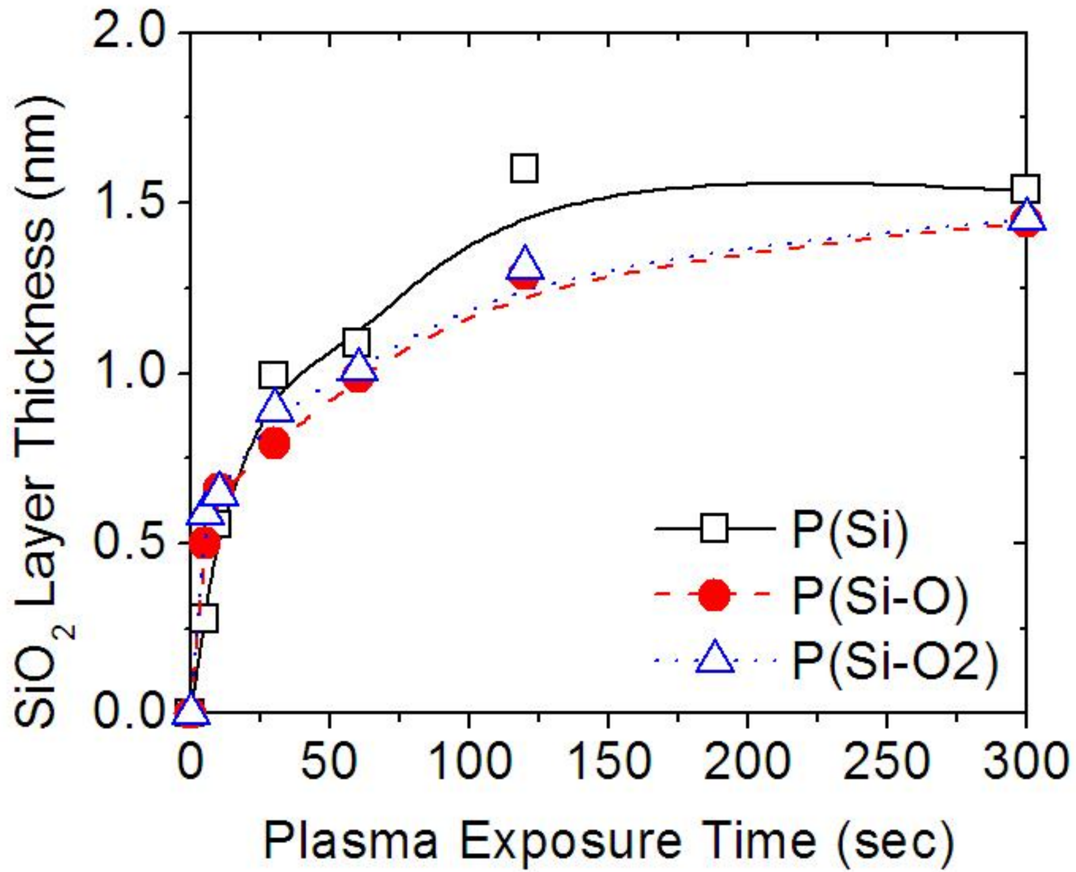

Figure 5.4: SiO_2 layer thickness measured by XPS for P(Si), P(Si-O), and P(Si-O2). Polymers were etched under O_2 plasma without substrate bias.

In Fig. 5.5, the thickness removed is plotted versus SiO_2 layer thickness. All polymers showed linear relationships, with P(Si) having a larger slope and the Si-O containing polymers nearly identical slopes.

If it is assumed that there is no Si loss during the conversion of the surface layer from a polymer with 12.1 wt% Si to SiO_2, the theoretical thickness removed, Δx_0, is

$$\Delta x_0 = d_{SiO2}\left(\frac{w_{SiO2}\rho_{SiO2}}{w_{poly}\rho_{poly}} - 1\right) \qquad (5.2)$$

where w is the weight percent of Si, ρ is the mass density, and the subscripts SiO2 and poly denote SiO_2 and the polymer, respectively. For the SiO_2 layer, w was 0.467 and ρ was 2.2 g/cm^3 and for the polymer, w was 0.121 and ρ was 1.0 g/cm^3. This method to measure the SiO_2 layer thickness has been discussed by Watanabe and Ohnishi[5.11] and is included in Fig. 5.5.

A larger slope of thickness removed versus SiO_2 layer thickness as compared to the case of no Si loss indicates a greater amount of Si loss during the experiments. P(Si), having the highest slope, had constantly more Si lost with SiO_2 layer thickness formed compared to P(Si-O) and P(Si-O2). Using equation 5.2, the %Si lost is

$$\% Si\ wt\ loss = 1 - \frac{\Delta x_0 / d_{SiO2} + 1}{\Delta x / d_{SiO2} + 1} \qquad (5.3)$$

where $\Delta x_0/d_{SiO2}$ is the slope for the case of no Si loss and $\Delta x/d_{SiO2}$ are the slopes for P(Si), P(Si-O), and P(Si-O2). For P(Si), %Si wt loss was 50% during SiO_2 layer formation while for P(Si-O) and P(Si-O2) the calculated value was 20%.

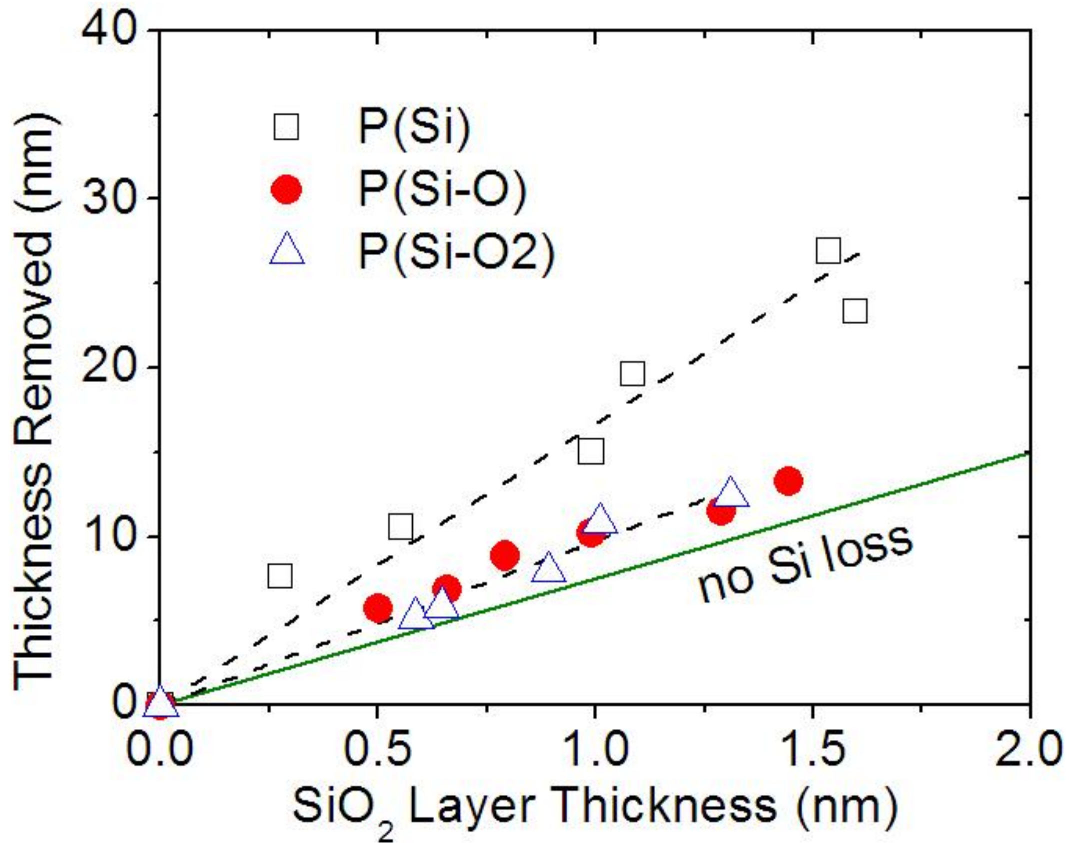

Figure 5.5: Thickness removed versus SiO_2 layer thickness formed is shown for P(Si), P(Si-O), and P(Si-O2) under O_2 plasma with no substrate bias conditions. Dashed lines are linear fits of the experimental data. The solid line is the theoretical linear relationship of thickness removed and SiO_2 layer thickness if no Si is lost during the formation of the SiO_2 layer calculated using equation 5.2.

In addition, the etch rate was plotted against SiO_2 layer thickness, and this is shown in Fig. 5.6. The dashed lines show an exponential decay behavior of etch rate with SiO_2 layer thickness, the form expected for a diffusion limited process. The etch rate converges to zero as the SiO_2 layer thickens since the reactive plasma species need to diffuse further before reaching the polymer to volatilize more material.[5.22] For P(Si), the etch rate was higher for equivalent SiO_2 layer thicknesses in P(Si-O) and P(Si-O2), suggesting a difference in the properties of the SiO_2 layer. The SiO_2 layer

formed in P(Si) may be more porous due to enhanced Si loss compared to P(Si-O) and P(Si-O2).

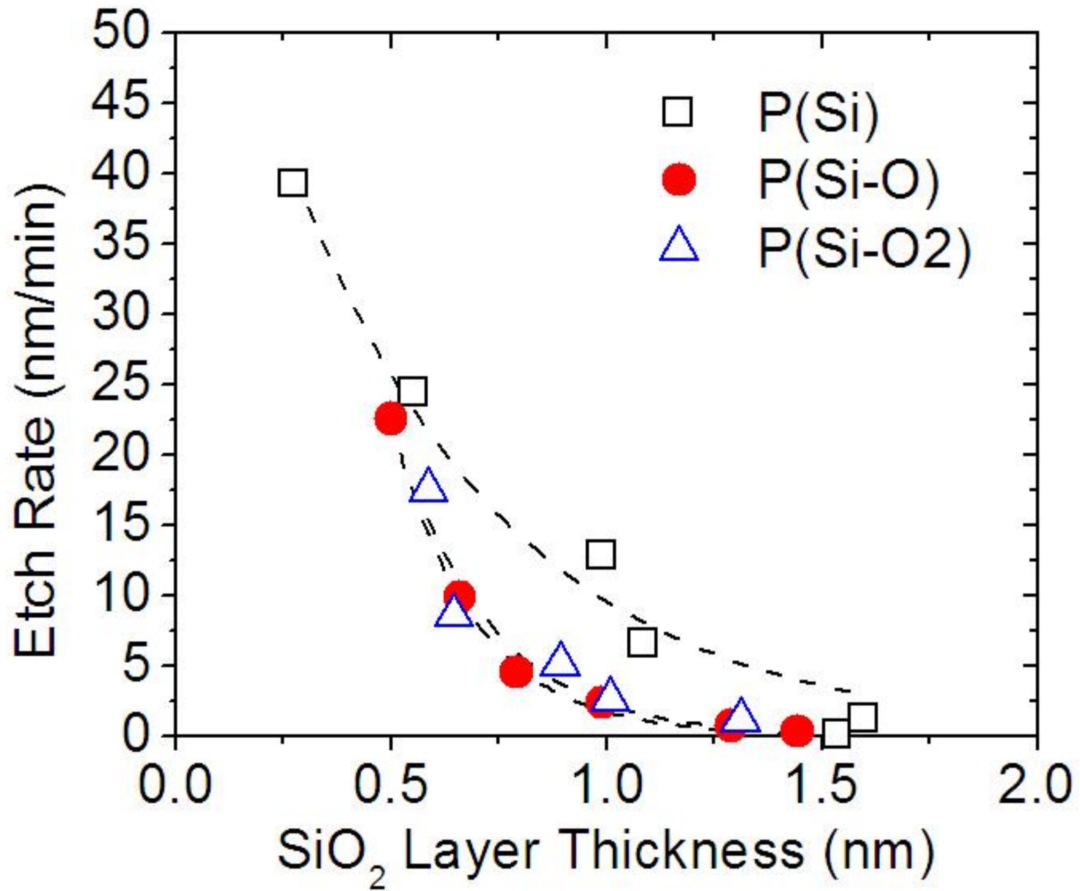

Figure 5.6: Etch rate versus SiO_2 layer thickness is shown for P(Si), P(Si-O), and P(Si-O2) under O2 plasma with no substrate bias conditions. Dashed lines are exponential decay fits of the experimental data.

5.3.3 Roughness Analysis

P(Si), P(Si-O) and P(Si-O2) showed widely varying roughening behavior as displayed in Fig.5.7(a). The lowest rms roughness values for a given exposure time were found in P(Si-O), with P(Si) showing slightly greater roughness and P(Si-O2) showed significantly larger rms roughness compared to the other polymers.

Differences in the roughening behavior of the Si-containing polymers were analyzed by examining the overall morphology of the surface roughness. AFM images of P(Si), P(Si-O) and P(Si-O2) after 120 seconds of plasma exposure are shown in Fig. 5.7(b). The surface roughness in P(Si) appeared as fine grains, with lateral length scale of ~50 nm. P(Si-O) and P(Si-O2), on the other hand, showed ~1 μm wrinkles along the polymer surface. The appearance of microscale roughening is known as reticulation,[5.23] which is highly undesirable during plasma processing. The onset of reticulation in P(Si-O) and P(Si-O2) during plasma exposure is indicated by an abrupt change in slope in the curves in Fig. 5.7(a).

The development of isotropic wrinkles can be linked to the formation of a bilayer structure composed of a thin, stiff film on soft substrate.[5.24,5.25] For Si-containing polymers, a bilayer structure is created during O_2 plasma exposure when the ~1 nm SiO_2 layer is formed on the surface. As measured by XPS, it was confirmed that the SiO_2 layer formed in P(Si), P(Si-O) and P(Si-O2) was similar in thickness and composition. From elastic buckling theory, it is the elastic modulus of the underlying polymer layer that dictates the magnitude of the wrinkle amplitude.[5.22] While the elastic modulus is very similar between linear polymers with similar degree of polymerization, it is dependent on temperature.[5.26] Above T_g the elastic modulus

decreases by four orders of magnitude,[5.23] thereby increasing the wrinkle amplitude and lateral length scale significantly[5.22] when a stressed SiO_2 layer[5.27] is formed at the surface. Referring to Table 5.1, the T_g of P(Si-O) and P(Si-O2) is below room temperature while P(Si) is 94 °C. Therefore, after SiO_2 layer formation in all polymers, P(Si-O) and P(Si-O2) formed microscale roughness morphology while P(Si) formed nanoscale roughness morphology. It is unclear why P(Si-O2) showed much larger rms roughness values compared to P(Si-O). The actual T_g values for the two polymers were too low to measure during this work. P(Si-O2) may have a lower T_g as compared to P(Si-O), leading to a smaller elastic modulus at equivalent temperatures.

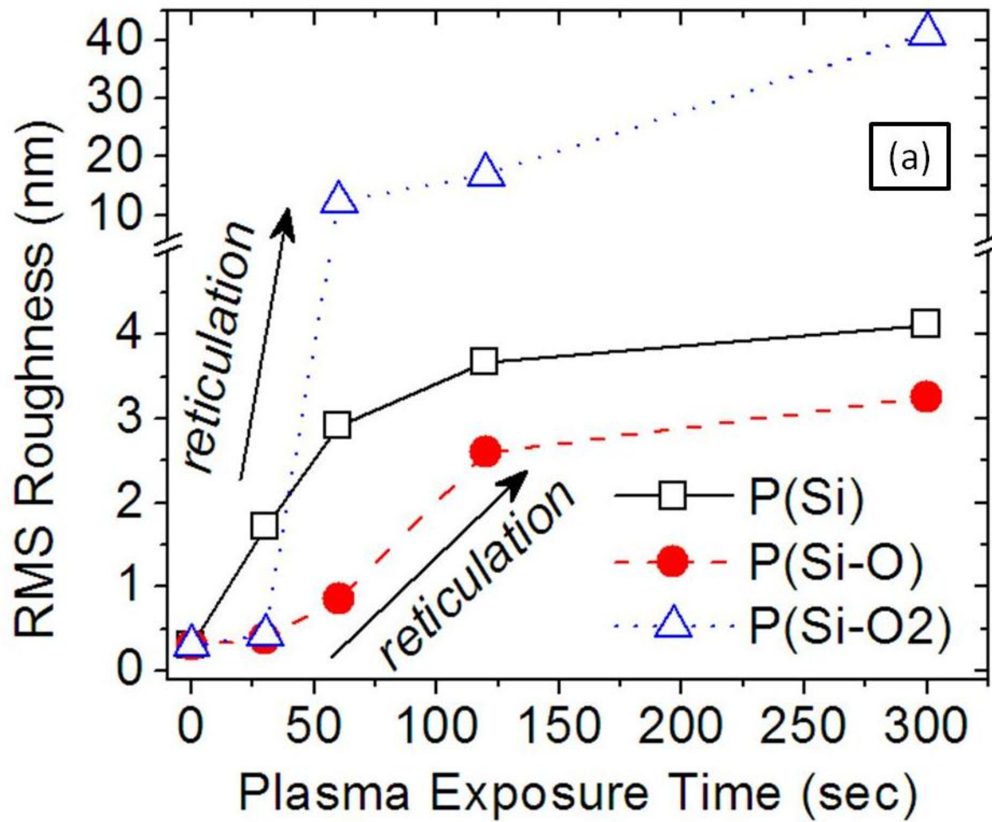

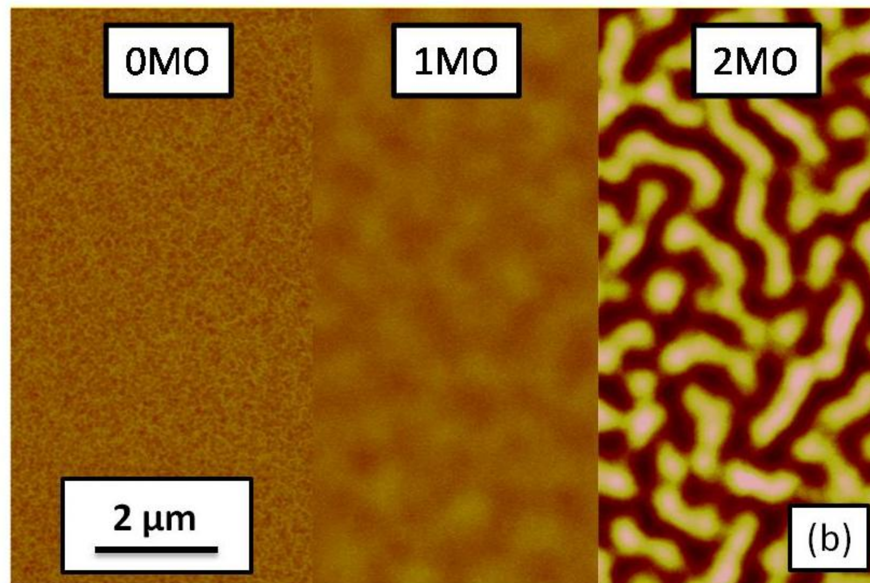

Figure 5.7: Plot (a) of rms roughness dependence on plasma exposure time in P(Si), P(Si-O) and P(Si-O2). Also shown are AFM images (b) of P(Si), P(Si-O) and P(Si-O2) after 120 seconds of plasma exposure. Polymer were etched under O_2 plasma without substrate bias.

5.3.4 Influence of Substrate Bias

P(Si), P(Si-O) and P(Si-O2) were also processed at -100V substrate bias under O_2 and 90% N_2/O_2 gas discharge conditions for 120 seconds to compare the etch behavior and roughness with the O_2 no bias condition. Substrate bias is a requirement for real plasma-based pattern transfer processes because it provides directional etch properties to limit opening the critical dimension size of patterned structures.[5.28] The etch properties of the polymers in 90% N_2/O_2 was examined as well since this gas discharge composition has been shown to provide good etch selectivity as well as sidewall passivation during the pattern transfer process.[5.29]

Etch rates versus thickness removed are shown in Fig. 5.8 for the three polymers in the different discharge conditions. Fig. 5.8(a) shows the polymer etch rate in O_2 discharges without substrate bias. P(Si) exhibited consistently greater etch rates with thickness removed compared to the other polymers. Fig. 5.8(b) shows the polymer etch rates in O_2 discharges with -100V substrate bias. The etch rates for all polymers became greater, indicating the contribution of ion sputtering of the SiO_2 layer to the etch rate. In addition, the difference in etch rate between P(Si) and the Si-O containing polymers became less. In Fig. 5.8(c), 90% N_2/O_2 discharges with -100V substrate bias was used and the etch rates for the polymers became similar to the O_2 discharge condition without substrate bias.

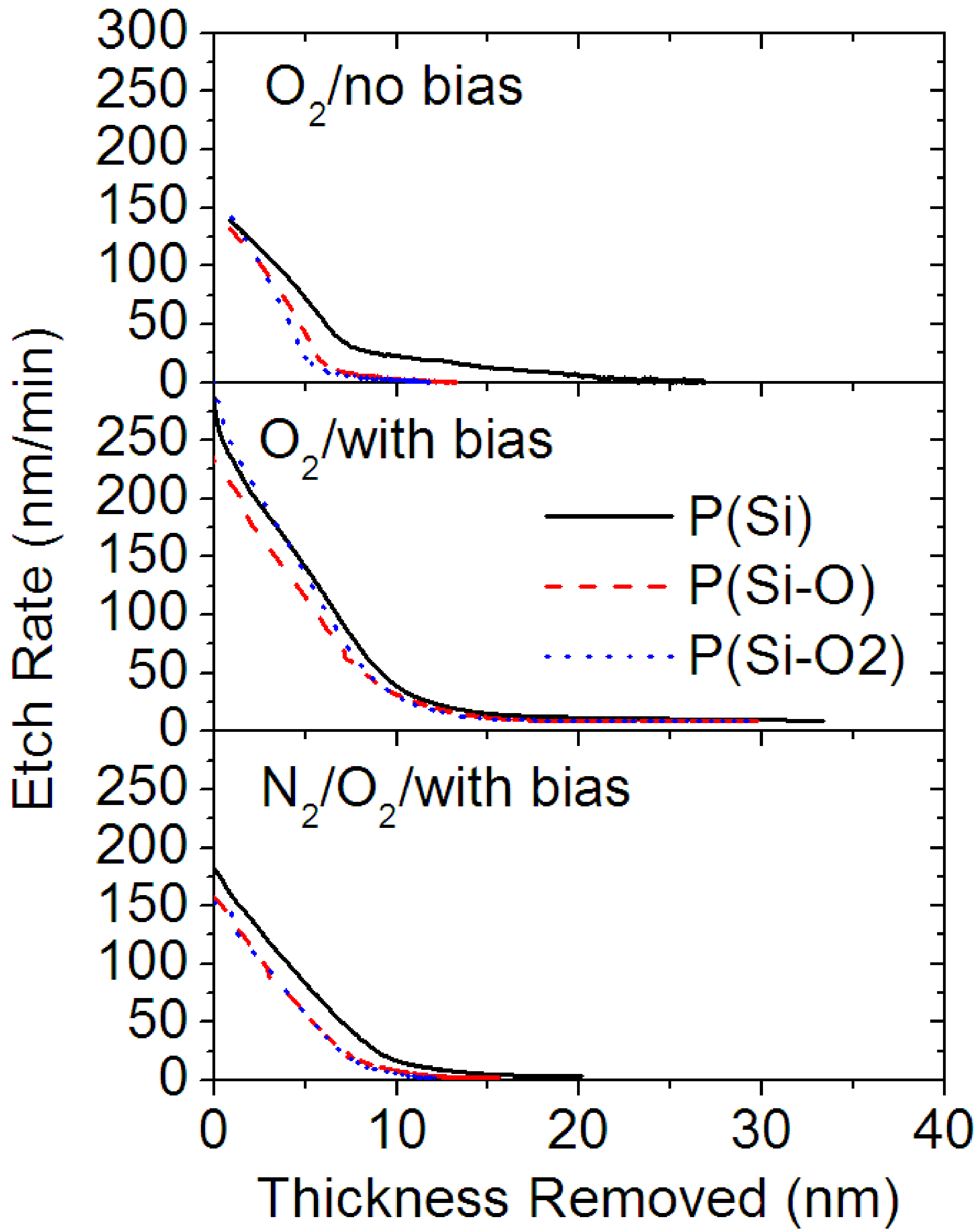

Figure 5.8: Etch rate dependence versus thickness removed is shown for P(Si), P(Si-O) and P(Si-O2) under (a) O_2 without substrate bias, (b) O_2 / -100V substrate bias, and (c) (90% N_2 / O_2) / -100V substrate bias processing conditions.

Figure 5.9(a) shows the thickness removed of the three polymers for all conditions after 120 seconds plasma exposure time. The condition of O_2 discharge without substrate bias showed the greatest difference in thickness removed for P(Si) as compared to the other polymers. For both cases with substrate bias, the difference in thickness removed is not so significant between P(Si) and the other polymers but is measureable. Adding N_2 to the gas discharge in the presence of a bias caused a significant reduction in overall thickness removed to a value intermediate between that for pure O_2 with and without such a bias.

SiO_2 layer thickness as measured by XPS analysis after 120 seconds plasma exposure is shown in Fig. 5.9(b). For the O_2 without substrate bias case, the SiO_2 layer thickness was larger for P(Si) as compared to the other polymers. However, with substrate bias, SiO_2 layer thickness showed lower values in P(Si). Overall, SiO_2 layer thickness was larger for the 90% N_2/O_2 discharge as compared with the O_2 discharges with and without substrate bias.

The rms roughness values measured by AFM after 120 seconds of plasma exposure are shown in Fig. 5.9(c). AFM measurements are only shown for the O_2 without bias and 90% N_2/O_2 with substrate bias conditions. Surface roughening in P(Si) and P(Si-O) was reduced in 90% N_2/O_2 with substrate bias compared to O_2 without bias. P(Si-O2) showed almost twice the rms roughness value in 90% N_2/O_2 with substrate bias compared with O_2 without bias and the morphology observed was microscale wrinkling (not shown).

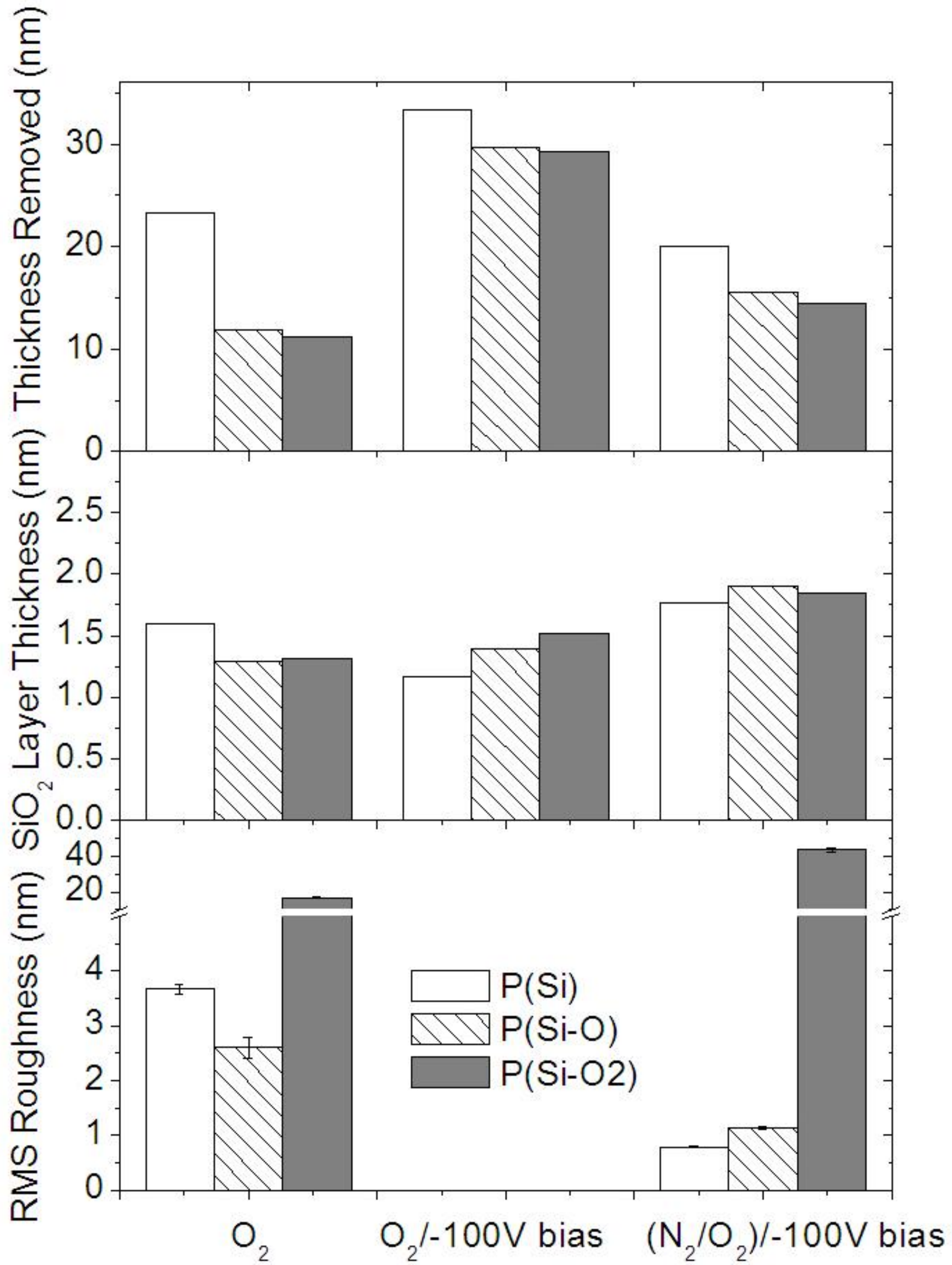

Figure 5.9: Thickness removed (a), SiO_2 layer thickness (b) and rms roughness (c) for P(Si), P(Si-O) and P(Si-O2) in O_2 without substrate bias, O_2 / -100V substrate bias, and (90% N_2 / O_2) / -100V substrate bias processing conditions.

Values for SiO_2 layer thickness versus thickness removed for the substrate bias conditions after 120 seconds of plasma exposure were combined with the data presented in Fig. 5.5. This is shown in Fig. 5.10(a). For the O_2 with substrate bias case, there is a greater deviation of values from the no Si loss case, which can be attributed to the physical sputtering of the SiO_2 layer by high energy ions leading to greater thickness removed values for equivalent SiO_2 layer thicknesses. For 90% N_2 /O_2 with substrate bias, the values were similar to the O_2 with no substrate bias case. However, values for P(Si) indicated greater Si loss compared to P(Si-O) and P(Si-O2) for all conditions.

The values for the substrate bias conditions were also combined with the data presented in Fig. 5.6 and this is shown in Fig. 5.10(b). For the condition of O_2 with substrate bias, the overall etch rates of the polymers were greater for equivalent SiO_2 layer thicknesses as compared to the condition without substrate bias. For the 90% N_2 /O_2 with substrate bias condition, overall etch rates were lower and characterized by a greater SiO_2 layer thickness values.

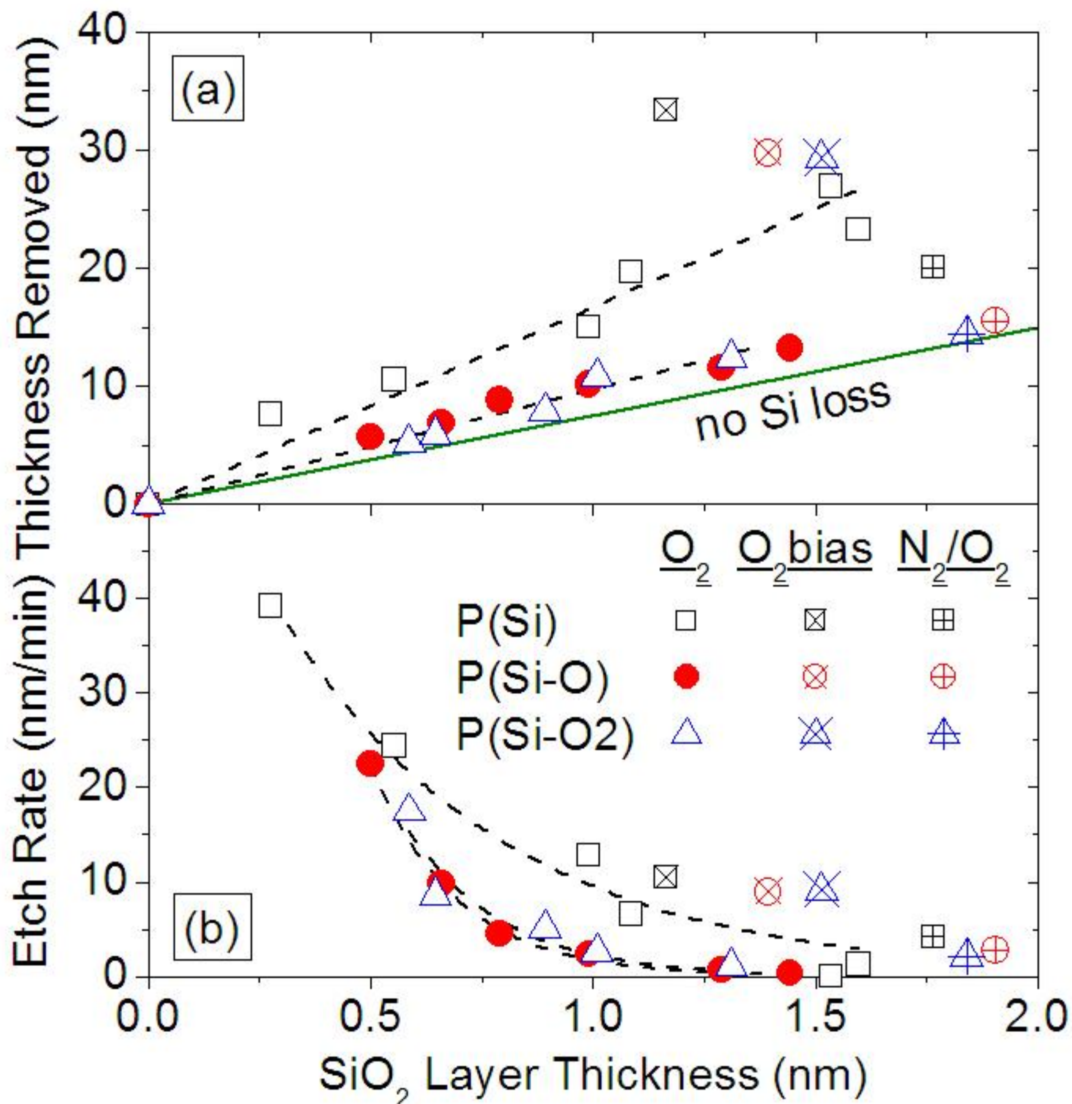

Figure 5.10: Thickness removed (a) and etch rate (b) versus SiO_2 layer thickness formed is shown for P(Si), P(Si-O), and P(Si-O2) under O_2 without substrate bias, O_2 /-100V substrate bias, and (90% N_2 /O_2) /-100V substrate bias conditions.

5.3.5 Mechanism of O_2 Plasma Etching

P(Si) had consistently different etch behavior compared to the Si-O containing polymers. It showed consistently greater Si loss, shown in Fig. 5.5, and higher etch rates for equivalent SiO_2 layer thicknesses, shown in Fig 5.6. The difference in etch

behavior is most likely linked to the lack of Si-O bonds, and the creation of more volatile Si-containing products than P(Si-O) and P(Si-O2). From equation 5.3, the %Si wt loss of P(Si) was found to be 50% compared to 20% in P(Si-O) and P(Si-O2). This large amount of Si loss may contribute to an SiO_2 layer with greater porosity in P(Si), which may explain the increased etch rates versus SiO_2 layer thickness in Fig. 5.6. A schematic of enhanced Si loss and etch rate due to a more porous SiO_2 layer in P(Si) is shown in Fig. 5.11(a), while the comparison of a less porous SiO_2 layer in P(Si-O) and P(Si-O2) is shown in Fig. 5.11(b).

The etch behavior changed for P(Si-O) and P(Si-O2) when a -100V substrate bias was added to the O_2 discharge. Larger thicknesses removed and etch rate values for equivalent SiO_2 layer thickness, shown in Figs. 5.10(a) and 5.10(b) indicated an increase in diffusion of oxygen species from the discharge through the SiO_2 layer due to the contribution of ion bombardment. P(Si) did not show much change in etch behavior, consistent with a more porous structure. For the case of 90%N_2 /O_2 with -100V substrate bias, the etching mechanism was similar to the O_2 with no substrate bias case. The overall values of SiO_2 layer thickness were larger compared to other conditions. In general, P(Si) consistently showed greater thicknesses removed compared to other polymers in all conditions, indicating an intrinsic property of enhanced Si loss due to the polymer structure.

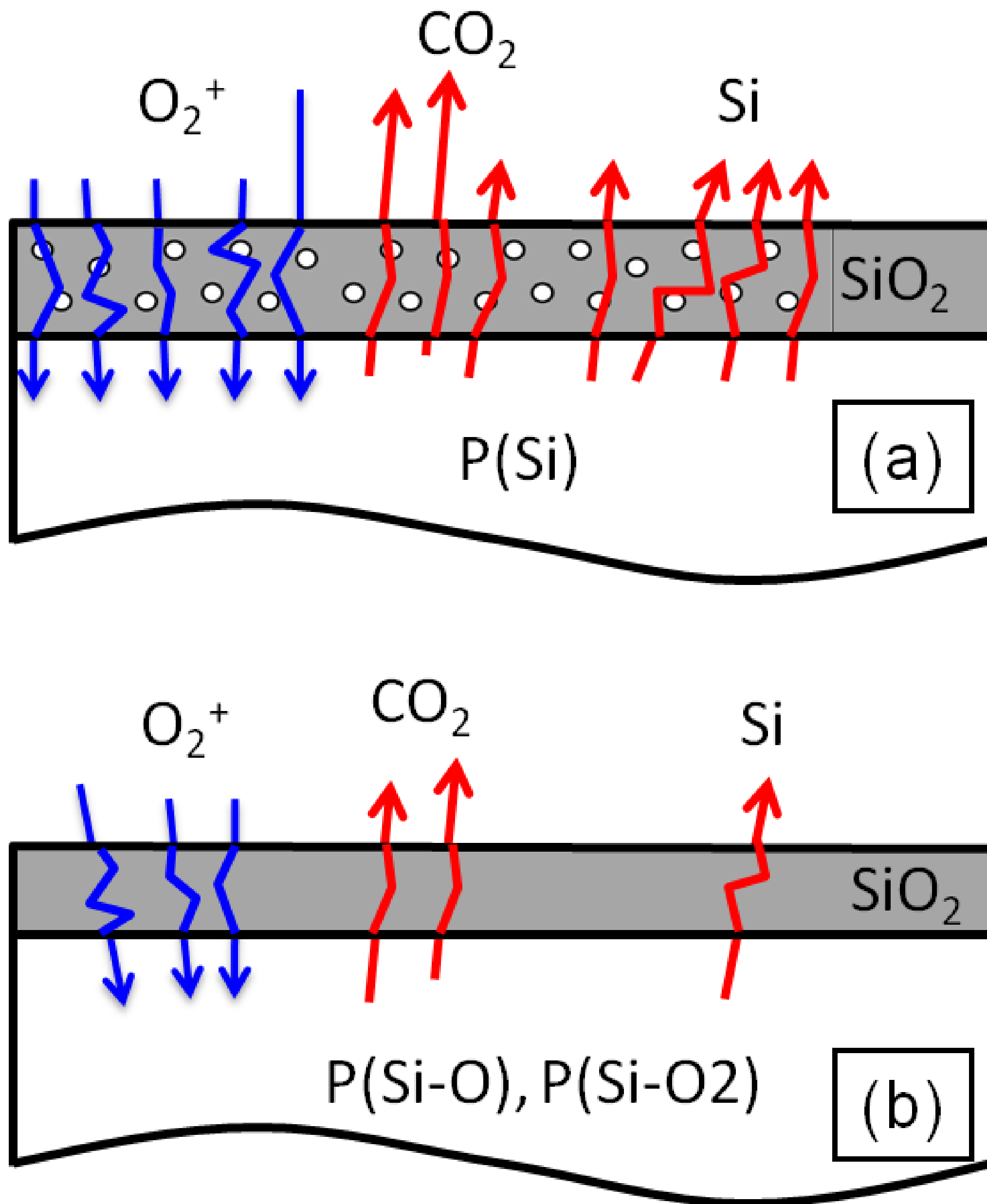

Figure 5.11: Schematic of etch behavior for (a) P(Si) and (b) P(Si-O) and P(Si-O2) under O_2 plasma without substrate bias.

5.4 Conclusion

Adding Si-O bonds to Si-containing polymers caused a significant reduction in thickness removed and Si loss during O_2 plasma exposure without substrate bias. Adding -100V substrate bias to the O_2 discharge reduced overall SiO_2 layer thicknesses due to physical sputtering of the SiO_2 layer. The case of 90% N_2 /O_2 showed instead an increase in the SiO_2 layer thickness. For all discharge conditions, polymers containing Si-O bonds consistently showed better etching properties. Increasing the number of Si-O bonds from one to two gave rise to almost identical etch behavior. However, adding Si-O bonds also reduced T_g and caused microscale wrinkling during the formation of the SiO_2 layer compared to that for no such bonds.

Acknowledgements

The authors gratefully acknowledge financial support by the National Science Foundation under awards CTS-0506988 and DMR-0705953. F. Weilnboeck and N. Fox-Lyon are thanked for their helpful comments and support.

Chapter 6: General Conclusions and Future Directions

The main goal of this PhD thesis was to establish an atomistic understanding of the interactions of polymer structures with prototypical plasmas during pattern transfer to enable the rational identification of both the molecular design parameters and internal plasma processing parameters required for controlled patterning at nanoscale dimensions.

In chapter 2, we established that a thin, dense, amorphous carbon-like layer is formed at the surface of polymers during plasma exposure due to ion bombardment. The etch rate of polymers was very high at the start of etching, but decreased significantly when the ion-modified layer was formed. Polymers with widely varying chemical structures showed the same modified surface layer formation, which indicated that ion damage was independent of polymer structure for the polymers examined in this work. VUV modification, however, was highly dependent on polymer structure and the temperature of the polymer during plasma etching.

We established a difference in the VUV surface modification mechanism of α-H and α-methyl polymer structures. While α-H polymers were fairly inert to material loss by VUV radiation, α-methyl polymers showed increased material loss as the polymer was heated closer to its ceiling temperature. However, we found little difference in ester-based α-H and α-methyl polymers due to rapid oxygen loss at the onset of etching. For ester-based polymers, material removal was inversely proportional to the oxygen content.

We also investigated the effect of ions and VUV on polymer surface roughness. Surface roughening of polymers only occurred under ion bombardment. VUV radiation did not cause surface roughness by itself, even in the case of rapid material loss as in poly(α-methylstyrene) (PαMS).

In chapter 3, we confirmed a relationship between plasma-induced surface roughness and the amorphous carbon-like layer formed by ion bombardment. We hypothesized that the formation of a stressed, ion-damaged layer at the surface of a soft polymer film would induce a buckling instability that would cause surface wrinkling to occur. Our goal was to establish that the surface morphology of plasma-processed polymer films could be calculated by elastic buckling theory using the mechanical properties and thickness of the ion-damaged layer. We showed that varying the properties of the ion-damaged layer caused changes in the wavelength and amplitude of the surface roughness that could be calculated by elastic buckling theory. We also found that the ion-damaged layer was responsible for both nanoscale surface roughness and microscale reticulations, which depended on the elastic modulus and the temperature of the polymer underlayer.

In chapter 4, we report the surprising absence of plasma-induced surface roughness in poly(4-vinylpyridine) (P4VP). Comparing the surface roughness and sidewall roughness of P4VP, polystyrene (PS), and PαMS, we show that the reduction in polymer surface roughness leads to a decrease in line edge roughness (LER). When plasma-induced surface roughness is absent, as in the case of P4VP, LER is eliminated. The mechanism that prevents plasma-induced surface roughness in P4VP was investigated by characterizing the mechanical property changes that occur in the

ion-damaged layer and the polymer underlayer. While we showed that nitrogen addition to the ion-damaged layer caused significant reduction in elastic modulus to the ion-damaged layer, P4VP showed instead similar ion-damaged layer properties to PS. However, VUV crosslinking was observed that would explain the suppression of wrinkling during ion-damaged layer formation.

In chapter 5, we studied the influence of Si-O bonding in the polymer structure of Si-containing resists on O_2 plasma etch behavior. In general, Si-containing polymers formed a ~1 nm SiO_2 layer at the surface that acted as a barrier to further oxygen etching. We observed a significant difference in etch behavior between polymers with no Si-O bonding and polymers with Si-O bonds. Si-O bonding greatly reduced the etch rate and Si loss during O_2 plasma etching, however surface roughness became more severe. Adding Si-O bonds to the polymer structure reduced the glass transition temperature below room temperature, making the polymer softer. When the SiO_2 layer is formed during O_2 plasma etch, the Si-O bonded polymers exhibited microscale wrinkling while polymers without Si-O bonding showed nanoscale wrinkling.

Overall, the present work shows that when polymers are used as resists in plasma-based pattern transfer, the effectiveness of the resist is due to the formation of a thin, dense layer at the resist surface that slows the rate of etching. However, this surface modified layer is the source of the plasma-induced roughening that leads to high LER. Plasma-induced surface roughness is dependent on the mechanical properties of the ion-damaged layer and the polymer underlayer. The properties of the ion-damaged layer are mostly dependent on plasma processing parameters. Low ion

energies produce ion-damaged layers that are thin and less dense, leading to lower surface roughness. The properties of the polymer underlayer are mostly dependent on the polymer structure. While PαMS has similar mechanical properties compared to PS, VUV radiation penetrates further into the bulk causing degradation reactions that weaken the underlayer and enhance the overall surface roughness. In the case of Si-containing polymers, increasing the amount of Si-O bonds in the polymer structure decreases the glass transition temperature making the polymer many orders of magnitude softer than Si-containing polymers without Si-O bonds. Surface roughness is enhanced because the thin, SiO_2 layer formed during O_2 plasma exposure is constrained to a much softer underlayer.

Therefore, to continue our progress in shrinking feature sizes enabling greater processing power, faster speeds, larger storage capacities, and reduced power consumption, the problem of roughness development during pattern transfer must be addressed. To reduce plasma-induced roughness, it is essential to take into account the mechanical properties of the resist and the change in mechanical properties during plasma exposure.

Characterizing the extent of plasma modification (ions, UV, radicals) in different polymer structures and determining the effect on the mechanics of buckling will help shed light on surface and LER issues in semiconductor and nanotechnology fabrication. This research is currently under investigation at the Laboratory for Plasma Processing of Materials at the University of Maryland, College Park.

References

Chapter 1:

1.1 G. E. Moore, Electronics, **38** (1965); G. E. Moore, IEEE IEDM Tech Digest, **11** (1975).

1.2 S. Wolf and R. N. Tauber, *Silicon Processing for the VLSI Era, Vol. 1*, (Lattice Press, CA, 1986).

1.3 International Technology Roadmap for Semiconductors, 2007 Edition.

1.4 A. Reiser, *Photoreactive Polymers* (Wiley, New York, 1989).

1.5 H. Schift, J. Vac. Sci. Technol. B **26**, 458 (2008).

1.6 C. T. Black, R. Ruiz, G. Breyta, J. Y. Cheng, M. E. Colburn, K. W. Guarini, H.-C. Kim and Y. Zhang, IBM J. Res. & Dev. **51**, 605 (2007).

1.7 G. S. Oehrlein, M. F. Doemling, B. E. E. Kastenmeier, P. J. Matsuo, N. R. Rueger, M. Schaepkens, and T. E. F. M. Standaert, IBM. J. Res. Dev. **43**, 181 (1999).

1.8 H. Ito, Adv. Polym. Sci. **172**, 37 (2005).

1.9 S.-J. Choi, J. Vac. Sci. Technol. B **25**, 868 (2007).

1.10 F. D. Egitto and L. J. Matienzo, IBM J. Res. Dev. **38**, 423 (1994).

1.11 D. T. Clark and A. Dilks, J. Polym. Sci. Pol. Chem. **15**, 2321 (1977).

1.12 J. J. Vegh, D. Nest, D. B. Graves, R. Bruce, S. Engelmann, T. Kwon, R. J. Phaneuf, G. S. Oehrlein, B. K. Long, and C. G. Willson, J. Appl. Phys. **104**, 034308 (2008).

1.13 K. J. Orvek and C. Huffman, Nucl. Instr. Meth. B **7/8**, 501 (1985).

1.14 Y. Koval, J. Vac. Sci. Technol. B **22**, 843 (2004).

1.15 A. Hollander, J. Behnisch, M. R. Wertheimer, *Plasma Processing of Polymers*, edited by R. d'Agostino, P. Favia, and F. Fracassi (Kluwer Academic Publishers, Norwell, MA, 1997), p. 411.

1.16 T. Hori, M. D. Bowden, K. Uchino, K. Muraoka and M. Maeda, J. Vac. Sci. Technol. A, **14**, 144 (1996).

1.17 M. A. Hartney, D. W. Hess and D. S. Soane, J. Vac. Sci. Technol. B **7**, 1 (1989).

1.18 X. Li, G. S. Oehrlein, M. Schaepkens, R. E. Ellefson and L. C. Frees, J. Vac. Sci. Technol. A, **21**, 1971 (2003).

1.19 B. Chapman, *Glow Discharge Processes*, (Wiley, New York, 1980), p. 43.

1.20 L. A. Wall, J. Polym. Sci., Part B, Polym. Phys. **17**, 141 (1955).

1.21 K. Dawes and L. C. Glover, *Physical Properties of Polymers Handbook*, edited by J. E. Mark (AIP Press, NY, 1996) p. 557.

1.22 J. Zekonyte, V, Zaporojtchenko, and F. Faupel, Nucl. Instr. Meth. B **236**, 241 (2005).

1.23 A. Chilkoti, D. G. Castner, and B. D. Ratner, Appl. Spectrosc. **45**, 209 (1991).

1.24 H. Gokan, S. Esho, and Y. Ohnishi, J. Electrochem. Soc. **130**, 143, (1983).

1.25 F. Watanabe and Y. Ohnishi, J. Vac. Sci. Technol. B **4**, 422 (1986).

1.26 C. W. Jurgensen, A. Shugard, N. Dudash, E. Reichmanis and M. J. Vasile, J. Vac. Sci. Technol. A **6**, 2938 (1988).

1.27 D. J. Abdallah, D. Mckenzie, A. Timko, A. Dioses, F. Houlihan, D. Rahman, S. Miyazaki, R. Zhang, W. Kim, H. Wu, L. Pylneva, P.-H. Lu, M. Neisser and R. R. Dammel, J. Photopolym. Sci. Technol. **20**, 697 (2007).

1.28 J. Kennedy, T. Baldwin-Hendricks, J. Stuck, A. Suedmeyer, S. Thanawala, K. Do and N. Iwamoto, Proc. SPIE, **5039**, 929 (2003).

1.29 S. Halle, A. Thomas, M. Armacost, T. Dalton, X. L. Chen, S. Bukofsky, O. Genz, Z. Lu, S. Butt, Z. Chen, R. Ferguson, E. Coker, R. Leidy, Q. Lin, A. Mahorowala, K. Babich, K. Petrillo, M. Angelopoulos, M. Ignatowicz and B. Bui, Proc. SPIE **4346**, 970 (2001).

1.30 A. P. Mahorowala, K. Babich, Q. Lin, D. R. Medeiros, K. Petrillo, J. Simons, M. Angelopoulos, R. Sooriyakumaran, D. Hofer, G. W. Reynolds and J. W. Taylor, J. Vac. Sci. Technol. A **18**, 1411 (2000).

1.31 A. Tserepi, G. Cordoyiannis, G. P. Patsis, V. Constantoudis, E. Gogolides, E. S. Valamontes, D. Eon, M. C. Peignon, G. Cartry, C. Cardinaud and G. Turban, J. Vac. Sci. Technol. B **21**, 174 (2003).

1.32 C. A. Ross, Y. S. Jung, V. P. Chuang, F. Illievski, J. K. W. Yang, I. Bita, E. L. Thomas, H. I. Smith, K. K. Berggren, G. J. Vancso and J. Y. Cheng, J. Vac. Sci. Technol. B **26**, 2489 (2008).

1.33 G. M. Schmid, M. D. Stewart, J. Wetzel, F. Palmieri, J. Hao, Y. Nishimura, K. Hen, E.-K. Kim, D. J. Resnick, J.-A. Liddle and C. Grant Willson, **24**, 1283 (2006).

1.34 M. Colburn, A. Grot, B.-J. Choi, M. Amistoso, T. Bailey, S. V. Sreenivasan, J. G. Ekerdt and C. Grant Willson, J. Vac. Sci. Technol. B **19**, 2162 (2001).

1.35 N. Sakai, J. Photopolym. Sci. Technol. **22**, 134 (2009).

1.36 J. J. Vegh, D. Nest, D. B. Graves, R. Bruce, S. Engelmann, T. Kwon, R. J. Phaneuf, G. S. Oehrlein, B. K. Long, and C. G. Willson, Appl. Phys. Lett. **91**, 233113 (2007).

1.37 D. Nest, D. B. Graves, S. Engelmann, R. L. Bruce, F. Weilnboeck, G. S. Oehrlein, C. Andes, and E. A. Hudson, Appl. Phys. Lett. **92**, 153113 (2008).

1.38 E. Pargon, K. Menguelti, M. Martin, A. Bazin, O. Chaix-Pluchery, C. Sourd, S. Derrough, T. Lill and O. Joubert, J. Appl. Phys. 105, 094902 (2009).

1.39 Y. Ban, S. Sundareswaran, R. Panda, and D. Z. Pan, Proc. SPIE **7275**, 727518 (2009).

1.40 A. Asenov, S. Kaya, and A. R. Brown, IEEE T. Electron. Dev. **50**, 1254 (2003).

1.41 M. Padmanaban, D. Rentkiewicz, C. Hong, D. Lee, D. Rahman, R. Sakamuri and R. R. Dammel, J. Photopolym. Sci. Technol. **18**, 451 (2005).

1.42 Y. Nishimura, T. B. Michaelson, J. E. Meiring, M. D. Stewart and C. G. Willson, J. Photopolym. Sci. Technol. **18**, 457 (2005).

1.43 T. Yamaguchi, H. Namatsu, M. Nagase, K. Yamazaki and K. Kurihara, Appl. Phys. Lett. **71**, 2388 (1997).

1.44 H. Namatsu, M. Nagase, T. Yamaguchi, K. Yamazaki and K. Kurihara, J. Vac. Sci. Technol. B **16**, 3315 (1998).

1.45 Q. Lin, R. Sooriyakumaran and W. Huang, Proc. SPIE **3999**, 230 (2000).

1.46 D. L. Goldfarb, A. P. Mahorowala, G. M. Gallatin, K. E. Petrillo, K. Temple, M. Angelopoulos, S. Rasgon, H. H. Sawin, S. D. Allen, M. C. Lawson, and R. W. Kwong, J. Vac. Sci. Technol. B **22**, 647 (2004).

1.47 A. P. Mahorowala, D. L. Goldfarb, K. Temple, K. E. Petrillo, D. Pfeiffer, K. Babich, M. Angelopoulos, G. Gallatin, S. Rasgon, H. H. Sawin, S. D. Allen, R. N. Lang, M. C. Lawson, R. W. Kwong, K.-J. Chen, W. Li, P. R. Varanasi, M. I. Sanchez, H. Ito, G. M. Wallraff, R. D. Allen, Proc. SPIE **5039**, 213 (2003).

1.48 S. Engelmann, R. L. Bruce, T. Kwon, R. Phaneuf, G. S. Oehrlein, Y. C. Bae, C. Andes, D. Graves, D. Nest, E. A. Hudson, P. Lazzeri, E. Iacob, and M. Anderle, J. Vac. Sci. Technol. B, **24**, 1353 (2007).

1.49 D. Bratton, D. Yang, J. Dai, and C. K. Ober, Polym. Adv. Technol. **17**, 94 (2006).

1.50 X. Li, X. Hua, L. Ling, G. S. Oehrlein, M. Barela and H. M. Anderson, J. Vac. Sci. Technol. A **20**, 2052 (2002).

1.51 X. Li, L. Ling, X. Hua, M. Fukusawa, G. S. Oehrlein, M. Barela, and H. M. Anderson, J. Vac. Sci. Technol. A **21**, 284 (2003).

1.52 X. Li, L. Ling, X. Hua, G. S. Oehrlein, Y. Wang, A. V. Vasenkov and M. J. Kushner, J. Vac. Sci. Technol. A **22**, 500 (2004).

1.53 A. V. Vasenkov, X. Li, G. S. Oehrlein, and M. J. Kushner, J. Vac. Sci. Technol. A **22**, 511 (2004).

1.54 F. L. McCrackin, E. Passaglia, R. R. Stromberg, and Harold L. Steinberg, J. Res. NBS A. Phys. Ch. **67A**, 363 (1963).

1.55 H. G. Tompkins, *A User's Guide to Ellipsometry* (Dover Publications, Inc., Mineola, NY, 1993).

Chapter 2:

2.1 F. D. Egitto and L. J. Matienzo, IBM J. Res. Dev. **38**, 423 (1994).

2.2 J. M. Grace and L. J. Gerenser, J. Disper. Sci. Technol. **24**, 305 (2003).

2.3 R. L. Kelly, *Atomic Emission Lines Below 2000 Angstrom, Hydrogen through Argon* (Naval Research Laboratory, Washington, DC, 1968), p. 246.

2.4 J. J. Vegh, D. Nest, D. B. Graves, R. Bruce, S. Engelmann, T. Kwon, R. J. Phaneuf, G. S. Oehrlein, B. K. Long, and C. G. Willson, J. Appl. Phys. **104**, 034308 (2008).

2.5 K. J. Orvek and C. Huffman, Nucl. Instr. Meth. B **7/8**, 501 (1985).

2.6 Y. Koval, J. Vac. Sci. Technol. B **22**, 843 (2004).

2.7 A. Hollander, J. Behnisch, M. R. Wertheimer, *Plasma Processing of Polymers*, edited by R. d'Agostino, P. Favia, and F. Fracassi (Kluwer Academic Publishers, Norwell, MA, 1997), p. 411.

2.8 L. A. Wall, J. Polym. Sci., Part B, Polym. Phys. **17**, 141 (1955).

2.9 K. Dawes and L. C. Glover, *Physical Properties of Polymers Handbook*, edited by J. E. Mark (AIP Press, NY, 1996) p. 557.

2.10 J. Zekonyte, V, Zaporojtchenko, and F. Faupel, Nucl. Instr. Meth. B **236**, 241 (2005).

2.11 A. Chilkoti, D. G. Castner, and B. D. Ratner, Appl. Spectrosc. **45**, 209 (1991).

2.12 H. Gokan, S. Esho, and Y. Ohnishi, J. Electrochem. Soc. **130**, 143, (1983).

2.13 X. Hua, S. Engelmann, G. S. Oehrlein, P. Jiang, P. Lazzeri, E. Iacob, and M. Anderle, J. Vac. Sci. Technol. B, **24**, 1850 (2006).

2.14 S. Engelmann, R. L. Bruce, T. Kwon, R. Phaneuf, G. S. Oehrlein, Y. C. Bae, C. Andes, D. Graves, D. Nest, E. A. Hudson, P. Lazzeri, E. Iacob, and M. Anderle, J. Vac. Sci. Technol. B, **24**, 1353 (2007).

2.15 T. E. F. M. Standaert, P. J. Matsuo, S. D. Allen, G. S. Oehrlein, and T. J. Dalton, J. Vac. Sci. Technol. A **17**, 741 (1999).

2.16 X. Li, X. Hua, M. Fukasawa, G. S. Oehrlein, M. Barela, and H. M. Anderson, J. Vac. Sci. Technol. A. **21**, 284, (2003).

2.17 T. Hori, M. D. Bowden, K. Uchino, K. Muraoka and M. Maeda, J. Vac. Sci. Technol. A, **14**, 144 (1996).

2.18 X. Li, G. S. Oehrlein, M. Schaepkens, R. E. Ellefson and L. C. Frees, J. Vac. Sci. Technol. A, **21**, 1971 (2003).

2.19 B. Chapman, *Glow Discharge Processes*, (Wiley, New York, 1980), p. 43.

2.20 F. L. McCrackin, E. Passaglia, R. R. Stromberg, and Harold L. Steinberg, J. Res. NBS A. Phys. Ch. **67A**, 363 (1963).

2.21 D. Nest, D. B. Graves, S. Engelmann, R. L. Bruce, F. Weilnboeck, G. S. Oehrlein, C. Andes, and E. A. Hudson, Appl. Phys. Lett. **92**, 153113 (2008).

2.22 F. Truica-Marasescu and M. R. Wertheimer, Macromol. Chem. Phys. **206**, 744 (2005).

2.23 T. Li, C. Zhou, and M. Jiang, Polym. Bull. **25**, 211-216 (1991).

2.24 C. Hopf, A. von Keudell, and W. Jacob, J. Appl. Phys. **93**, 3352 (2003).

2.25 A. Terrasi, G. Foti, Y. Hwu, and G. Margaritondo, J. Appl. Phys. **70**, 1885 (1991).

2.26 S. C. Sharma, M. Green, R. C. Hyer, C. A. Dark, T. D. Black, A. R. Chourasia, D. R. Chopra, K. K. Mishra, and J. Mater. Res. **5**, 2424 (1990).

2.27 H. R. Allcock, F. W. Lampe, *Contemporary Polymer Chemistry* (Prentice-Hall, NJ, 1990) p. 239.

2.28 G. Odian, *Principles of Polymerization* (Wiley,NJ, 2004) p. 279.

2.29 J. P. Chen, K. Isa, T. Kodaira, T. Senda, J. Mass. Spectrom. Soc. Jpn. **47**, 371 (1999).

2.30 J. P. Chen, T. Kodaira, K. Isa, T. Senda, J. Mass. Spectrom. Soc. Jpn. **49**, 41 (2001).

Chapter 3:

3.1 H. Ito, IBM J. Res. Dev. **45**, 683 (2001).

3.2 T. Li, Z. Y. Huang, Z. C. Xi, S. P. Lacour, S. Wagner, and Z. Suo, Mech. Mater. **37**, 261 (2005).

3.3 F. D. Egitto and L. J. Matienzo, IBM J. Res. Develop. 38, 423 (1994).

3.4 J. J. Vegh, D. Nest, D. B. Graves, R. Bruce, S. Engelmann, T. Kwon, R. J. Phaneuf, G. S. Oehrlein, B. K. Long, and C. G. Willson, Appl. Phys. Lett. **91**, 233113 (2007).

3.5 D. Nest, D. B. Graves, S. Engelmann, R. L. Bruce, F. Weilnboeck, G. S. Oehrlein, C. Andes, and E. A. Hudson, Appl. Phys. Lett. **92**, 153113 (2008).

3.6 E. Pargon, K. Menguelti, M. Martin, A. Bazin, O. Chaix-Pluchery, C. Sourd, S. Derrough, T. Lill and O. Joubert, J. Appl. Phys. 105, 094902 (2009).

3.7 D. T. Clark and A. Dilks, J. Polym. Sci. Pol. Chem. **15**, 2321 (1977).

3.8 Y. Koval, J. Vac. Sci. Technol. B 22, 843 (2004).

3.9 A. R. Pal, R. L. Bruce, F. Weilnboeck, S. Engelmann, T. Lin, M.-S. Kuo, R. Phanuef, and G. S. Oehrlein, J. Appl. Phys. **105**, 013311 (2009).

3.10 M. Sumiya, R. Bruce, S. Engelmann, F. Weilnboeck, and G. S. Oehrlein, J. Vac. Sci. Technol. B **26**, 1637 (2008).

3.11 J. J. Vegh, D. Nest, D. B. Graves, R. Bruce, S. Engelmann, T. Kwon, R. J. Phaneuf, G. S. Oehrlein, B. K. Long and C. G. Willson, J. Appl. Phys. **104**, 034308 (2008).

3.12 O. Joubert, P. Czuprynski, F. H. Bell, P. Berruyer and R. Blanc, J. Vac. Sci. Technol. B 15, 629 (1997).

3.13 B. K. Gan, M. M. M. Bilek, A. Kondyurin, K. Mizuno and D. R. McKenzie, Nucl. Instr. and Meth. in Phys. Res. B 247, 254 (2006).

3.14 J. Zekonyte, Zaporojtchenko and F. Faupel, Nucl. Instr. and Meth. in Phys. Res. B 236, 241 (2005).

3.15 M. Collaud Coen, P. Groening, G. Dietler and L. Schlapbach, J. Appl. Phys. 77, 5695 (1995).

3.16 N. Negishi, H. Takesue, M. Sumiya, T. Yoshida, Y. Momonoi and M. Izawa, J. Vac. Sci. Technol. B 23, 217 (2005).

3.17 R. L. Bruce, S. Engelmann, T. Lin, T. Kwon, R. J. Phaneuf, G. S. Oehrlein, B. K. Long, C. G. Willson, J. J. Vegh, D. Nest, D. B. Graves and A. Alizadeh, J. Vac. Sci. Technol. B **27**, 1142 (2009).

3.18 N. Bowden, W. T. S. Huck, K. E. Paul and G. M. Whitesides, Appl. Phys. Lett., 75, 2557 (1999).

3.19 N. Bowden, S. Brittain, A. G. Evans, J. W. Hutchinson and G. M. Whitesides, Nature **393**,146 (1998).

3.20 H. Jiang, D.-Y. Khang, J. Song, Y. Sun, Y. Huang and J. A. Rogers, Proc. Natl. Acad. Sci. USA 104, 15607 (2007).

3.21 R. Huang, J. Mech. Phys. Solids **35**, 63 (2005).

3.22 C.M. Stafford, C. Harrison, K. L. Beers, A. Karim, E. J. Amis, M. R. Vanlandingham, H.-C. Kim, W. Volksen, R. D. Miller, and E. E. Simonyi, Nat. Mater. **3**, 545 (2004).

3.23 P. J. Yoo and H. H. Lee, Macromolecules, 38, 2820 (2005).

3.24 E. P. Chan, K. A. Page, S. H. Im, D. Patton, R. Huang and C. M. Stafford, Soft Matter 5, 1 (2009).

3.25 J. R. Serrano, Q. Xu and D. G. Cahill, J. Vac. Sci. Technol. A 24, 324 (2006).

3.26 A. Yahata, S. Urano and T. Inoue, Jpn. J. Appl. Phys. 36, 6722 (1997).

3.27 D. L. Goldfarb, A. P. Mahorowala, G. M. Gallatin, K. E. Petrillo, K. Temple, M. Angelopoulos, S. Rasgon, H. H. Sawin, S. D. Allen, M. C. Lawson and R. W. Kwong, J. Vac. Sci. Technol. B 22, 647 (2004).

3.28 J. Kim, Y. S. Chae, W. S. Lee, J. W. Shon, C. J. Kang, W. S. Han and J. T. Moon, J. Vac. Sci. Technol. B 21, 790 (2003).

3.29 M. Collaud Coen, G. Dietler, S. Kasas and P. Groening, Appl. Surf. Sci. 103, 27 (1996).

3.30 S. Netcheva and P. Bertrand, Nucl. Instr. and Meth. in Phys. Res. B 151, 129 (1999).

3.31 R. Wilken, A. Hollander and J. Behnisch, Plasmas and Polymers 7, 185 (2002).

3.32 J. E. Mark, Polymer Data Handbook (Oxford University Press, New York, 1999).

3.33 H. G. Tompkins and W. A. McGahan, *Spectroscopic Ellipsometry and Reflectometry* (Wiley, New York, 1999).

3.34 R. M. France and R. D. Short, Langmuir 14, 4827 (1998).

3.35 P. Louette, F. Bodino and J.-J. Pireaux, Surface Science Spectra, 12, 96 (2005).

3.36 D. Briggs and M. P. Seah, Practical Surface Analysis (Wiley, Chichester, 1983), p. 165.

3.37 B. Lesiak, A. Jablonski, Z. Prussak and P. Mrozek, Surf. Sci. 223, 213 (1989).

3.38 P. Prieto, C. Quiros, E. Elizalde, J. M. Sanz, J. Vac. Sci. Technol. A **24**, 396 (2006).

3.39 T. Schwarz-Selinger, A. von Keudell and W. Jacob, J. Appl. Phys. **86**, 3988 (1999).

3.40 D. Schneider, T. Schwarz, H.-J, Scheibe, and M. Panzer, Thin Solid Films **295**, 107 (1997).

3.41 J. Robertson, Mat. Sci. Eng. R **37**, 129 (2002).

3.42 J. Schwan, S. Ulrich, H. Roth, H. Ehrhardt, S. R. P. Silva, J. Robertson, R. Samlenski, and R. Brenn, J. Appl. Phys. **79**, 1416 (1996).

3.43 C. A. Davis, Thin Solid Films **226**, 30 (1993).

3.44 A. I. Kalinichenko, S. S. Perepelkin, and V. E. Strel'nitskij, Diamond Relat. Mater. **15**, 365 (2006).

3.45 A. C. Ferrari, J. Robertson, M. G. Beghi, C. E. Bottani, R. Ferulano and R. Pastorelli, Appl. Phys. Lett. **75**, 1893 (1999).

3.46 I. W. Gilmour, A. Trainor and R. N. Haward, J. Appl. Polym. Sci. 23, 3123 (1979).

3.47 A. J. Staverman, Proc. R. Soc. London, Ser. A **282**, 115 (1964).

3.48 F. Weilnboeck, R. L. Bruce, S. Engelmann, G. S. Oehrlein, D. Nest, T.-Y. Chung, D. Graves, M. Li, D. Wang, C. Andes and E. A. Hudson, J. Vac. Sci. Technol. B (to be submitted).

Chapter 4:

4.1 Y. Ban, S. Sundareswaran, R. Panda, and D. Z. Pan, Proc. SPIE **7275**, 727518 (2009).

4.2 A. Asenov, S. Kaya, and A. R. Brown, IEEE T. Electron. Dev. **50**, 1254 (2003).

4.3 D. L. Goldfarb, A. P. Mahorowala, G. M. Gallatin, K. E. Petrillo, K. Temple, M. Angelopoulos, S. Rasgon, H. H. Sawin, S. D. Allen, M. C. Lawson, and R. W. Kwong, J. Vac. Sci. Technol. B **22**, 647 (2004).

4.4 A. P. Mahorowala, D. L. Goldfarb, K. Temple, K. E. Petrillo, D. Pfeiffer, K. Babich, M. Angelopoulos, G. Gallatin, S. Rasgon, H. H. Sawin, S. D. Allen, R. N. Lang, M. C. Lawson, R. W. Kwong, K.-J. Chen, W. Li, P. R. Varanasi, M. I. Sanchez, H. Ito, G. M. Wallraff, R. D. Allen, Proc. SPIE **5039**, 213 (2003).

4.5 L. Ling, X. Hua, X. Li, G. S. Oehrlein, E. A. Hudson, P. Lazzeri, and M. Anderle, J. Vac. Sci. Technol. A **22**, 2594 (2004).

4.6 J. J. Vegh, D. Nest, D. B. Graves, R. Bruce, S. Engelmann, T. Kwon, R. J. Phaneuf, G. S. Oehrlein, B. K. Long, and C. G. Willson, J. Appl. Phys. **104**, 034308 (2008).

4.7 R. L. Bruce, S. Engelmann, T. Lin, T. Kwon, R. J. Phaneuf, G. S. Oehrlein, B. K. Long, C. G. Willson, J. J. Vegh, D. Nest, D. B. Graves, and A. Alizadeh, J. Vac. Sci. Technol. B **27**, 1142 (2009).

4.8 R. L. Bruce, F. Weilnboeck, T. Lin, R. J. Phaneuf, G. S. Oehrlein, B. K. Long, C. G. Willson, J. J. Vegh, D. Nest, and D. B. Graves, Journal of Applied Physics (to be published).

4.9 S. Engelmann, R. L. Bruce, T. Kwon, R. Phaneuf, G. S. Oehrlein, Y. C. Bae, C. Andes, D. Graves, D. Nest, E. A. Hudson, P. Lazzeri, E. Iacob, and M. Anderle, J. Vac. Sci. Technol. B **25**, 1353 (2007).

4.10 H. Ito, Adv. Polym. Sci. **172**, 37 (2005).

4.11 D. Bratton, D. Yang, J. Dai, and C. K. Ober, Polym. Adv. Technol. **17**, 94 (2006).

4.12 A. Majumdar, J. Schafer, P. Mishra, D. Ghose, J. Meichsner, and R. Hippler, Surf. Coat. Tech. **201**, 6437 (2007).

4.13 E. Broitman, N. Hellgren, K. Jarrendahl, M. P. Johansson, S. Olafsson, G. Rodnoczi, J.-E. Sundgren, and L. Hultman, J. Appl. Phys. **89**, 1184 (2001).

4.14 H. Schift, J. Vac. Sci. Technol. B **26**, 458 (2008).

4.15 H. G. Tompkins and W. A. McGahan, *Spectroscopic Ellipsometry and Reflectometry* (Wiley, New York, 1999).

4.16 J. E. Mark, Polymer Data Handbook (Oxford University Press, New York, 1999).

4.17 M. Biesalski and J. Rhe, Langmuir **16**, 1943 (2000).

4.18 X. Hua, S. Engelmann, G. S. Oehrlein, P. Jiang, P. Lazzeri, E. Iacob, and M. Anderle, J. Vac. Sci. Technol. B **24**, 1850 (2006).

4.19 S. M. Smith, S. A. Voight, H. Tompkins, A. Hooper, A. A. Talin, and J. Vella, Thin Solid Films **398-399**, 163 (2001).

4.20 C. Popov, L. M. Zambov, M. F. Plass, and W. Kulisch, Thin Solid Films **377-378**, 156 (2000).

4.21 Y. M. Ng, C. W. Ong, X.-A. Zhao, and C. L. Choy, J. Vac. Sci. Technol. A **17**, 584 (1999).

4.22 R. Huang, J. Mech. Phys. Solids **35**, 63 (2005).

4.23 R. M. France and R. D. Short, Langmuir 14, 4827 (1998).

4.24 P. Louette, F. Bodino and J.-J. Pireaux, Surface Science Spectra, 12, 96 (2005).

4.25 G. Beamson and D. Briggs, *High Resolution XPS of Organic Polymers – The Scienta ESCA300 Database* (Wiley, Chichester, 1992).

4.26 D. Briggs and M. P. Seah, *Practical Surface Analysis* (Wiley, Chichester, 1983), p. 165.

4.27 P. Prieto, C. Quiros, E. Elizalde, J. M. Sanz, J. Vac. Sci. Technol. A **24**, 396 (2006).

4.28 X. W. Zhang, W. Y. Cheung, N. Ke and S. P. Wong, J. Appl. Phys. **92**, 1242 (2002).

4.29 S. Gauthier, D. Duchesne and A. Eisenberg, Macromolecules **20**, 753 (1987).

4.30 A. Hollander, J. Behnisch, M. R. Wertheimer, in *Plasma Processing of Polymers*, edited by R. d'Agostino, P. Favia, and F. Fracassi (Kluwer Academic, Norwell, MA, 1997), p. 411.

Chapter 5:

5.1 S.-J. Choi, J. Vac. Sci. Technol. B **25**, 868 (2007).

5.2 D. J. Abdallah, D. Mckenzie, A. Timko, A. Dioses, F. Houlihan, D. Rahman, S. Miyazaki, R. Zhang, W. Kim, H. Wu, L. Pylneva, P.-H. Lu, M. Neisser and R. R. Dammel, J. Photopolym. Sci. Technol. **20**, 697 (2007).

5.3 J. Kennedy, T. Baldwin-Hendricks, J. Stuck, A. Suedmeyer, S. Thanawala, K. Do and N. Iwamoto, Proc. SPIE, **5039**, 929 (2003).

5.4 S. Halle, A. Thomas, M. Armacost, T. Dalton, X. L. Chen, S. Bukofsky, O. Genz, Z. Lu, S. Butt, Z. Chen, R. Ferguson, E. Coker, R. Leidy, Q. Lin, A. Mahorowala, K. Babich, K. Petrillo, M. Angelopoulos, M. Ignatowicz and B. Bui, Proc. SPIE **4346**, 970 (2001).

5.5 A. P. Mahorowala, K. Babich, Q. Lin, D. R. Medeiros, K. Petrillo, J. Simons, M. Angelopoulos, R. Sooriyakumaran, D. Hofer, G. W. Reynolds and J. W. Taylor, J. Vac. Sci. Technol. A **18**, 1411 (2000).

5.6 A. Tserepi, G. Cordoyiannis, G. P. Patsis, V. Constantoudis, E. Gogolides, E. S. Valamontes, D. Eon, M. C. Peignon, G. Cartry, C. Cardinaud and G. Turban, J. Vac. Sci. Technol. B **21**, 174 (2003).

5.7 C. A. Ross, Y. S. Jung, V. P. Chuang, F. Illievski, J. K. W. Yang, I. Bita, E. L. Thomas, H. I. Smith, K. K. Berggren, G. J. Vancso and J. Y. Cheng, J. Vac. Sci. Technol. B **26**, 2489 (2008).

5.8 G. M. Schmid, M. D. Stewart, J. Wetzel, F. Palmieri, J. Hao, Y. Nishimura, K. Hen, E.-K. Kim, D. J. Resnick, J.-A. Liddle and C. Grant Willson, **24**, 1283 (2006).

5.9 M. Colburn, A. Grot, B.-J. Choi, M. Amistoso, T. Bailey, S. V. Sreenivasan, J. G. Ekerdt and C. Grant Willson, J. Vac. Sci. Technol. B **19**, 2162 (2001).

5.10 N. Sakai, J. Photopolym. Sci. Technol. **22**, 134 (2009).

5.11 F. Watanabe and Y. Ohnishi, J. Vac. Sci. Technol. B **4**, 422 (1986).

5.12 M. A. Hartney, D. W. Hess and D. S. Soane, J. Vac. Sci. Technol. B **7**, 1 (1989).

5.13 C. W. Jurgensen, A. Shugard, N. Dudash, E. Reichmanis and M. J. Vasile, J. Vac. Sci. Technol. A **6**, 2938 (1988).

5.14 S. Hayase, Prog. Polym. Sci. **28**, 359 (2003).

5.15 E. Reichmanis, G. Smolinsky and C. W. Wilkins, Jr., Solid State Tech., **28**, 130 (1985).

5.16 B. K. Long, Ph. D. Thesis, University of Texas, Austin, 2009.

5.17 T. E. F. M. Standaert, P. J. Matsuo, S. D. Allen, G. S. Oehrlein and T. J. Dalton, J. Vac. Sci. Technol. A **17**, 741 (1999).

5.18 X. Li, X. Hua, M. Fukusawa, G. S. Oehrlein, M. Barela and H. M. Anderson, J. Vac. Sci. Technol. A **21**, 284 (2003).

5.19 H. G. Tompkins and W. A. McGahan, *Spectroscopic Ellipsometry and Reflectometry* (Wiley, New York, 1999), p. 31.

5.20 D. Briggs and M. P. Seah, *Practical Surface Analysis* (Wiley, Chichester, 1983), p. 165.

5.21 S. Tanuma, C. J. Powell and D. R. Penn, Surf. Interface Anal., **17**, 927 (1991).

5.22 T. E. F. M. Standaert, M. Schaepkens, N. R. Rueger, P. G. M. Sebel, G. S. Oehrlein, and G. M. Cook, J. Vac. Sci. Technol. A **16**, 239 (1998).

5.23 A. R. Pal, R. L. Bruce, F. Weilnboeck, S. Engelmann, T. Lin, M.-S. Kuo, R. Phanuef, and G. S. Oehrlein, J. Appl. Phys. **105**, 013311 (2009).

5.24 N. Bowden, S. Brittain, A. G. Evans, J. W. Hutchinson and G. M. Whitesides, Nature **393**, 146 (1998).

5.25 R. Huang, J. Mech. Phys. Solids **35**, 63 (2005).

5.26 D. G. Gilbert, M. F. Ashby and P. W. R. Beaumont, J. Mater. Sci. **21**, 3194 (1986).

5.27 N. J. Chou, C. H. Tang, J. Paraszczak and E. Babich, Appl. Phys. Lett. **46**, 31 (1985).

5.28 M. Pons, O. Joubert, C. Martinet, J. Pelletier, J.-P. Panabiére and A. Weill, Jpn. J. Appl. Phys. **33**, 991 (1994).

5.29 R. S. Hutton, C. H. Boyce and G. N. Taylor, J. Vac. Sci. Technol. B **13**, 2366 (1995).